Combined evaluation of strong motion and GPS data for analyzing coseismic deformation caused by strong earthquakes

Inauguraldissertation
zur Erlangung des akademischen Doktorgrades

eingereicht am Fachbereich Geowissenschaften,
der Freien Universität Berlin

vorgelegt von

Muzli Muzli

April 15, 2013

Als Dissertation angenommen vom Fachbereich Geowissenschaften
der Freien Universität Berlin.

auf Grund der Gutachten
von Priv. Doz. Dr. Günter Asch
und Prof. Dr. Serge Shapiro

Berlin, den 15. April 2013

Eidesstattliche Erklärung

Bei der eingereichten Dissertation zu dem Thema *"Combined evaluation of strong motion and GPS data for analyzing coseismic deformation caused by strong earthquakes"* handelt es sich um meine eigenständig erbrachte Leistung.

- Ich habe nur die angegebenen Quellen und Hilfsmittel benutzt und mich keiner unzulässigen Hilfe Dritter bedient. Insbesondere habe ich wörtlich oder sinngemäß aus anderen Werken übernommene Inhalte als solche kenntlich gemacht.

- Die Arbeit oder Teile davon habe ich nicht an einer Hochschule des In- oder Auslands als Bestandteil einer Prüfungs- oder Qualifikationsleistung vorgelegt.

- Ich versichere an Eides statt, dass ich nach bestem Wissen die reine Wahrheit erklärt und nichts verschwiegen habe.

Statement of Authorship

The thesis I have submitted entitled *"Combined evaluation of strong motion and GPS data for analyzing coseismic deformation caused by strong earthquakes"* is my own accomplishment.

- I have only used the sources indicated and have not made unauthorised use of services of a third party. Where the work of others has been quoted or reproduced, the source is always given.

- I have not presented this thesis or parts thereof to a university as part of an examination or degree.

- I affirm that the above is the absolute truth to the best of my knowledge and that I have not concealed anything.

Muzli Muzli
April 15, 2013

Zusammenfassung

In dieser Studie wird die koseismische statische Oberflächendeformation durch zweifache Integration von Strong Motion Beschleunigungsdaten berechnet. Strong Motion Daten haben im Vergleich zu GPS-Messungen den Vorteil, Angaben über koseismische statische Verschiebung in Echtzeit bereitstellen zu können. Allerdings zeigen Strong Motion Daten das klassische Problem eines Basislinienversatzes. Dieser kann nach der zweifachen Integration der Beschleunigungsdaten zu unrealistischen Werten für die Bodenverschiebung führen. Dieses Problem wird durch eine bilineare Kurvenangleichung der empirischen Basislinienkorrektur behoben.

Wir untersuchen eine verbesserte Methode zur Basislinienkorrektur, welche die maximale Flachheit der Deformationskurve als Bedingung hat, sowie kumulative Energieverhältnisse als Grenzwerte verwendet. Diese Methode wird auf seismische Datensätze des 2003, Mw 8.3 Tokachi-Oki Bebens, des 2007, Mw 7.7 Tocopilla Bebens, des 2010, Mw 7,8 Mentawai Bebens und des 2011, Mw 9.0 Tohoku Bebens angewandt. Für die meisten Datensätze sind im allgemeinen die aus Strong Motion Daten berechneten Verschiebungen mit den durch GPS gemessenen Verschiebungen vergleichbar. Allerdings kann die Anwendung der Methode auf Fernfeld-Daten zu schlechten Ergebnissen führen. Es wird bestätigt, dass das kumulative Energieverhältnis als Grenzwert für die Basislinienkorrektur verwendet werden kann.

Die große Datenmenge und sehr gute Datenqualität der Strong Motion Bohrlochdaten des Tohoku Bebens erlaubt eine genauere Untersuchung der genannten Methode. Die Abhängigkeit der Methode von Hypozentraldistanz, Magnitude und des verwendeten Bruchmodells wird analysiert. Wir zeigen eine starke Abhängigkeit der Methode von den gegebenen Parametern, im speziellen vom Parameter Hypozentraldistanz. Desweiteren zeigen wir, dass bei der Benutzung dieser Methode zwischen horizontalen und vertikalen Komponenten

unterschieden werden sollte. Die Verwendung unserer verbesserten Methode minimiert signifikant die Abweichung zwischen aus Strong Motion Daten berechneter Verschiebung und durch GPS Messungen gemessene Verschiebung für Horizontal- und Vertikalkomponente.

In einer weiteren Untersuchung optimieren wir den Einsatz von wichtigen, schnell verfügbaren statischen Verschiebungsdaten, gewonnen aus Strong Motion Daten oder aus GPS-Stationen nahe der Quelle. Wir schlagen eine Rastersuche zur Berechnung der Momentenmagnitude anhand des Modells von Okada (1985) vor. Die Methode liefert auch unter Verwendung von Daten nur einer einzelnen Station akzeptable Momentenmagnitudenberechnungen. Diese Berechnung kann sehr schnell ($\sim$5 Minuten) durchgeführt werden und kann somit wertvolle Informationen, für z.B. die Tsumanifrühwarnung, liefern.

Abstract

We recover coseismic static surface deformation by double integration of strong motion accelerometric data. Compared to GPS measurement, the advantage of strong motion data is that they have the potential to provide real-time coseismic static displacements. Strong motion data, however, has the classic problem of baseline offsets which produce unrealistic displacements after double integration is applied. We adopted a bilinear line fitting of empirical baseline correction method to overcome such problem.

We investigate the improvement methods of baseline correction that constrain the maximum flatness of the displacement trace and use the cumulative energy ratio as a threshold. We apply the methods to data sets of the 2003, Mw 8.3 Tokachi-Oki earthquake, the 2007, Mw 7.7 Tocopilla earthquake, the 2010, Mw 7.8 Mentawai earthquake and the 2011, Mw 9.0 Tohoku earthquake. We show that, in general, the results of strong motion derived displacements are comparable to nearby GPS data for most data sets, although for far-field data the method may lead to poor results. It confirms that cumulative energy ratio is appropriate to be used as a threshold of baseline correction method.

The very large and very good quality of boreholes strong motion data of the Tohoku earthquake gives opportunity to investigate the method deeply. We analyze the dependency of the method on hypocenter distance, magnitude and rupture model of the earthquake. We found that the method has a strong dependency on the given parameters, particularly on hypocenter distance. We also show that the method should be distinguished for horizontal and vertical components. Using our improvement method in this study, the deviations of vector length between strong motion derived displacements and nearby GPS data either for horizontal or vertical components, are significantly minimized.

Further study, we optimize the use of valuable rapid static displacement data obtained from strong motion or GPS near-source station. We introduce a centroid grid

search method to calculate the moment magnitude by using Okada (1985) model. Our method calculates reasonable moment magnitude using data even only from single station. This method can be done very rapidly within $\sim$5 minutes. It provides crucial information e.g. for making tsunami warning decision.

Abstrak

Perhitungan coseismic deformasi atau pergeseran permanen permukaan bumi akibat gempabumi kuat dapat dilakukan dengan menerapkan dua kali integrasi terhadap data strong motion. Pengukuran deformasi permukaan dapat juga dilakukan dengan menggunakan metode GPS. Dibandingkan dengan metode GPS, penggunaan data strong motion memiliki kelebihan yaitu dapat menentukan deformasi permukaan secara real-time. Meskipun demikian, data strong motion memiliki masalah klasik yaitu pergeseran garis dasar dari posisi nol. Pergeseran garis dasar tersebut terjadi pada saat seismometer mengalami goncangan kuat akibat gempabumi. Pergeseran ini, walaupun relatif sangat kecil, memiliki pengaruh yang sangat besar terhadap hasil perhitungan deformasi permukaan akibat dari proses integrasi dua kali. Hal tersebut menyebabkan hasil perhitungan deformasi permukaan menjadi tidak realistis. Untuk mengatasi permasalahan tersebut, kami mengadopsi metode empiris bilinier line fitting untuk koreksi pergeseran garis dasar.

Kami pelajari metode empiris terbaru berdasarkan bilinier line fitting untuk koreksi garis dasar. Metode ini dilakukan melalui pengamatan terhadap tingkat kedataran gelombang displacement dan menggunakan rasio energi kumulatif dari gelombang untuk menentukan titik-titik pembatas, yang akan digunakan untuk proses koreksi garis dasar. Kami menerapkan metode tersebut terhadap beberapa gempabumi kuat yaitu Tokachi-Oki, tahun 2003 dengan Mw 8.3, Tocopilla, 2007 dengan Mw 7.7, Mentawai, 2010 dengan Mw 7.8 dan Tohoku, 2011 dengan Mw 9.0. Hasil studi kami menunjukkan bahwa secara umum penerapan metode tersebut menghasilkan deformasi permukaan yang sebanding dengan hasil pengukuran GPS untuk hampir semua data, meskipun pada beberapa data yang relatif jauh dari epicenter gempabumi, hasilnya kurang memuaskan. Hasil ini menegaskan bahwa rasio energi kumulatif tepat digunakan sebagai acuan untuk menentukan titik-titik pembatas pada proses koreksi garis dasar.

Data gempabumi Tohoku yang sangat besar jumlahnya dan memiliki kualitas yang sangat baik memberikan kesempatan untuk mempelajari lebih dalam tentang metode koreksi garis dasar tersebut di atas. Kami menganalisis ketergantungan dari metode tersebut terhadap pengaruh jarak hypocenter, magnitudo dan model rupture gempabumi. Kami menemukan bahwa metode tersebut sangat tergantung pada beberapa parameter yang disebutkan di atas, terutama jarak hypocenter. Kami juga menunjukkan bahwa metode koreksi garis dasar tersebut harus dibedakan untuk komponen horizontal dan vertikal. Kami mengajukan metode perbaikan, dengan menggunakan metode perbaikan ini, selisih hasil deformasi permukaan dari data strong motion dengan hasil yang diperoleh dari pengukuran GPS dapat diperkecil.

Pada studi lebih lanjut, kami mengoptimalkan penggunaan data real-time deformasi permukaan untuk melakukan perhitungan magnitudo momen (Mw). Kami mengajukan metode grid search terhadap posisi centroid dari sumber gempabumi dengan menggunakan model Okada (1985). Metode kami dapat menghitung magnitudo momen dengan hanya menggunakan data dari satu stasiun. Penambahan jumlah data dapat memperbaiki kualitas magnitudo secara bertahap. Metode ini dapat dilakukan dalam waktu yang sangat cepat yaitu $\sim$5 menit. Hasil magnitudo momen ini memberikan informasi yang sangat penting sebagai salah satu parameter yang dibutuhkan dalam pengambilan keputusan terhadap peringatan dini tsunami.

Contents

Chapter 1

Introduction

1.1 Background and motivation

Coseismic static surface deformations occur due to strong earthquakes. Their amplitude and direction depend on source parameters, location and magnitude of the earthquakes. Studies using GPS (Global Positioning System) measurements, InSAR (Interferometric Synthetic Aperture Radar) and strong motion records that present the coseismic displacement have been published widely (e.g. Larson, 2009; Motagh et al., 2010; Béjar-Pizarro et al., 2010; Trifunac, 1971; Graizer, 1979; Wang et al., 2011).

Compared to strong motion derived displacement, satellite-based methods (i.e. GPS and InSAR) can measure the amplitude of static ground displacement with relatively higher accuracy. GPS instruments, however, provide precise measurements with longer time periods of observation. This may lead to a time delay of hours, days or even longer for obtaining GPS data. In opposite to GPS instrument, the strong motion accelerometer records the ground acceleration during an earthquake with higher sampling rates and higher sensitivity to dynamic ground motion. The instrument shows best performance for the time history

of displacements. This advantage of an accelerometer makes it possible to be used for analyzing the time dependent of the earthquake mechanism e.g. source time function or rupture process. Not only dynamic displacement, double integration of accelerometric data can also provide static displacements due to strong earthquakes. Analysis of displacements data from both instruments is complementary each other. In this thesis, however, we focus on the analysis of static displacements derived from strong motion data.

Other advantages of strong motion recording are their potential to provide the static displacement in real-time, low cost and a worldwide higher stations density, particularly in seismically active regions. It is our motivation to show that reasonable static displacements can be accurately derived from strong motion data and much faster compared to satellite-based methods. It is even possible to be done in real-time. We then test the usefulness of this data e.g. for tsunami early warning. For instance, the rapid static displacement data can potentially be used to quickly calculate moment magnitude (Mw), which is extremely important as it is one of the main parameters to make a decision for early warning of tsunami. Moreover, we realize that in some earthquake prone regions like Indonesia, lack of strong motion or GPS stations. We want to show that with a relatively few good measurements of static displacements, moment magnitude can be estimated rapidly with an accuracy that justifies its use in the context of tsunami early warning. *Chapter* 6 of this thesis describes much more about the advantages of rapid static displacements data and method of moment magnitude estimation using data even from single strong motion or GPS near-source station.

1.2 Problem statement

The challenge for strong motion data processing, however, the accelerometric data has the classic problem of unpredictable baseline shifts that occur during strong shaking. This

problem can be removed after a baseline correction is applied. Using strong motion records or acceleration data the displacement can in principle be obtained by double integration. However, in practice very often the naive double integration applied to uncorrected acceleration data will produce unrealistic displacements. This problem arises because of baseline shifts in the acceleration data. Iwan et al. (1985) attributed the problem to mechanical hysteresis in the sensors. Boore (2003) showed that analog-to-digital converter can be the source of baseline shift and Rodgers (1968); Boore (2001); Graizer (2005, 2006, 2010) indicated that the ground tilt and rotation during the strong shaking is the source of baseline shifts.

Iwan et al. (1985) proposed the initial robust empirical method of bilinear baseline correction for the first time. From the experiments, they observed the baseline shifts occurred when the acceleration exceeds 50 $cm\ s^{-2}$. Consequently, they proposed the velocity obtained from integration of acceleration data should be corrected with a bilinear baseline correction.

Based on the method described by Iwan et al. (1985), Wu & Wu (2007) proposed a new approach by using flatness constraints of the displacement trace. They calculated and observed the flatness of displacement trace. The displacement trace should be very flat after it reaches the permanent displacement position. The average velocity of the ground should become zero when the ground has reached the new permanent position. The correction methods by Iwan et al. (1985) and Wu & Wu (2007), essentially attempt to constrain the average velocity time series at the beginning and at the end of the earthquake records to become zero or very close to zero.

The procedure proposed by Wu & Wu (2007) is already a standardized approach and behaves as the best model for several data sets. Nevertheless, Chao et al. (2009) and Rupakhety et al. (2009) noted that the time points in their procedure are determined

arbitrarily in a recursive process and there is no clear prescription when the iterative scheme of the method should be stopped. Chao et al. (2009) improved the method of Wu & Wu (2007). They proposed an automatic scheme to determine the time points described by Wu & Wu (2007) method based on the threshold of cumulative energy ratio.

1.3 Objectives

We compare the methods proposed by Chao et al. (2009) and Iwan et al. (1985) using several data sets of strong earthquakes. The largest data set we use, is the 2011, Mw 9.0 Tohoku earthquake which was recorded by the KiK-Net strong motion network operated by NIED (National Research Institute for Earth Science and Disaster Prevention), Japan (Aoi et al., 2004; Suzuki et al., 2011). We also use other data sets of megathrust earthquakes, which occurred at slab interfaces and shallow depth in the seismic coupling area at subduction zones. The depth of seismic coupling at subduction zones is not lower than ∼40 km (Ruff & Kanamori, 1983). Only the earthquakes in this location can release the greatest energy and cause significant damage and tsunami disasters. Normally, the shallow strong megathrust earthquakes affect the significant static surface deformation. In this study, we use the strong motion data of the 2007, Mw 7.7 Tocopilla earthquake, recorded by the strong motion network of IPOC (Integrated Plate Boundary Observatory Chile) (Schurr et al., 2009), same data that was used by Wang et al. (2011) but with some additional data from seismic network of University of Chile (Boroschek et al., 2008); the 2010, Mw 7.8 Mentawai earthquake, Sumatra, obtained from strong motion network of BMKG (Meteorological, Climatological and Geophysical Agency of Indonesia) (Wjayanto, 2007; Muzli et al., 2011); the 2003, Mw 8.3 Tokachi-Oki earthquake, Japan and the 2011, Mw 9.0 Tohoku earthquake, recorded by KiK-net strong motion network, Japan.

Previous studies show that the method proposed by Chao et al. (2009) works well for many data sets, i.e., the 2003, Mw 6.8 Chengkung earthquake, the 2006, Mw 6.1 Taitung earthquake, the 1999, Mw 7.6 Chi-chi earthquake (Chao et al., 2009) and the 2007, Mw 7.7 Tocopilla earthquake (Wang et al., 2011). However, as already mentioned in Chao et al. (2009) for the relatively small coseismic deformation or far-field data, the method may lead to poor results. The limitation was also shown by Wang et al. (2011) in their results using data set of the 2007, Mw 7.7 Tocopilla earthquake. Based on this limitation, we suspect there is a hypocenter distance dependency of the time points estimation in the baseline correction method.

The very large and very good quality of boreholes strong motion data of the Tohoku earthquake gives us the opportunity to investigate the method deeply. First study, we apply a similar technique as described by Chao et al. (2009) to find the best position of thresholds based on the cumulative energy ratio for the whole data set of Mw 9.0 Tohoku earthquake. Compared to the existing method, the difference we make in this study, is that we distinguish data processing for horizontal and vertical components. In the second part of this study, we search for the best position of the thresholds gradually for each group of data sets at different hypocentral distances. We analyze the dependency of the method on the given parameters. We also analyze the influence of rupture model to the cumulative energy method. Finally, we compare the results of our study with the results calculated using existing method.

Further study, we observed that the static displacement obtained from strong motion records can already reach a stable position soon after the strong shaking transient. For instance, as shown in Figure 1.1b the stable static displacement at station MYGH12 (38.642N, 141.44E) can be obtained about 150 sec after P-wave arrival time. In fact, the whole 100% of energy is recorded at around 300 sec after P-wave arrival time. The station

is located ∼114 km from hypocenter location.

For the tsunami early warning purposes, it is important to release reliable information as soon as possible using rapid displacement data. Additional data can be included and processed incrementally. The method proposed by Chao et al. (2009), however, can not be applied before the seismogram reach 100% of cumulative energy, because they determine the time points for the baseline correction at 25% and 65% of total cumulative energy. Therefore, in this study, we analyze the arrival time of the empirical time points T1 and T3 related to the cumulative energy distribution of each accelerogram recorded. We then establish the relation of arrival time of empirical time points T1 and T3 as a function of station to hypocenter distance. Using such relation we can speed up the calculation of static displacement from strong motion records.

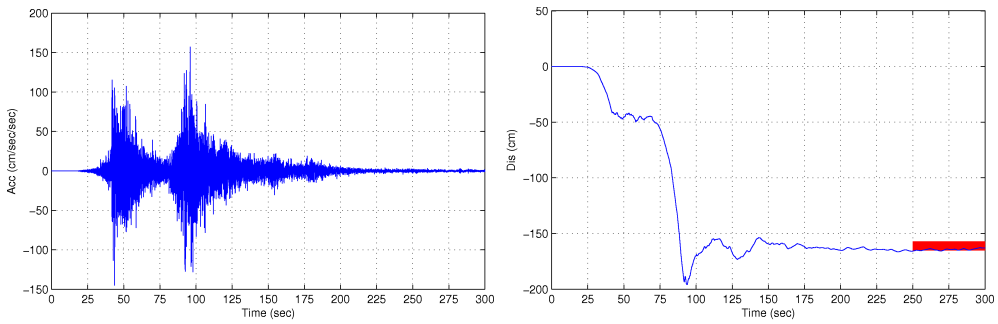

(a) **(b)**

Figure 1.1: (a) Accelerogram of the 2011, Mw 9.0 Tohoku earthquake recorded at station MYGH12 (north-south component). The distance of station to hypocenter location is ∼114 km. (b) Displacement trace after double integration and baseline correction was applied. Short red line near the end of the record shows the static displacement from nearby GPS measurement at station 0175 with the distance of ∼4.62 km.

In order to investigate the causality of the baseline shifts in the accelerometric data, we also conducted an experiment of strong motion recordings by using a shaking table. In the experiments, we give the input of static displacements to the shaking table and recover the output by double integration of acceleration records. We compare the input and recovered static displacements. The shaking table is designed with a high accuracy linear

displacement driver. Therefore, it is our hypothesis that the results of static displacements from the experiment are not influenced by the tilt. We assume that, in contrast to the experimental data, the real strong motion data of the earthquakes are contaminated by several possible sources of baseline shifts, particularly the tilt. It happens due to rotational motion of the ground during the strong shaking (Rodgers, 1968; Boore, 2001; Graizer, 2005, 2006, 2010). This should not occur during the experiment using the shaking table.

Chapter 2

Theory and Method

2.1 Coseismic deformation

Seismic waves are generated by natural sources such as an earthquake, or artificial such as an explosion. The waves propagate through the medium of earth's layers and are recorded by the seismic sensors or other instruments. When the earthquake fault ruptures, it produces two types of deformations. They are static and dynamic deformations. Static deformation is defined as the permanent displacement of the earth's surface due to strong earthquakes and dynamic deformation is essentially the waves that radiated by the earthquake ruptures. An important feature of these two kinds of deformations is that the static deformation decays by the factor of $1/r^2$. It is faster compared to propagating waves which decay by the factor of 1/r.

Based on the time period of seismic deformation, they are devided to several phases. The very long time deformation during return period of the earthquake is known as interseismic deformation. In this period, energy is accumulated at the fault interface. The deformation or displacement that occurs at the time of earthquake occurrence or during

the mainshock is identified as coseismic deformation. During this period, the earthquake releases its greatest energy. Another phase is post-seismic deformation. In this phase, the earthquake releases its rest of energy and the fault moves aseismically. This period is then followed by the new interseismic period. In this study, we only focus on analysis of coseismic deformation.

The earthquake releases its greatest energy during the mainshock. The relatively strong earthquakes often cause static deformation at near-source regions. This coseismic deformation can be recorded by satellite-based instruments (e.g. GPS or InSAR) and seismic sensors. Coseismic deformation occurs in horizontal and vertical displacements.

Figure 2.1 showing illustration of seismic deformation that occurs in subduction zones. It shows the plate convergence boundary between oceanic and continental plates. First stage on top figure showing the oceanic plate subducts or dives beneath the continental plate. In the period of interseismic, the large energy accumulates at the slab interface. Fault is locked. An earthquake occurs when the continental crust, which is lighter than the oceanic crust, is forced up suddently. It happens when the breaking strength of the fault has been reached. As shown in second stage, the fault then ruptures suddently. The earthquake releases large energy. At the vicinity of epicenter location, a strong shallow earthquake can produce static deformation, which is known as the coseismic deformation.

Coseismic surface deformation is a function of earthquake size, location, source mechanism and fault geometry. Understanding surface deformation at smaller scale of area can be simulated using a simple pure strike-slip faulting model on an infinitely long vertically dipping fault.

Figure 2.2 (Top) shows the strike-slip vertically dipping fault with the strike in x direction and dip of 90 degrees. (Bottom) Static dislacements due to the fault dislocation are observed at distances along y direction.

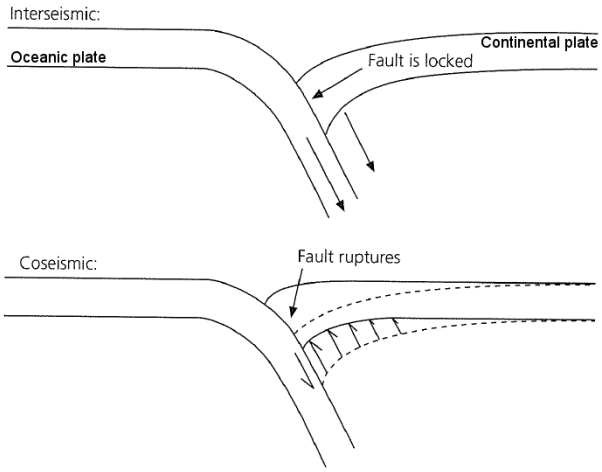

Figure 2.1: Two stages of seismic deformation that occur in subduction zones. First stage on top figure showing the interseicmic period. Second stage showing the fault ruptures during the period of coseismic (modified from Stein & Wysession, 2003).

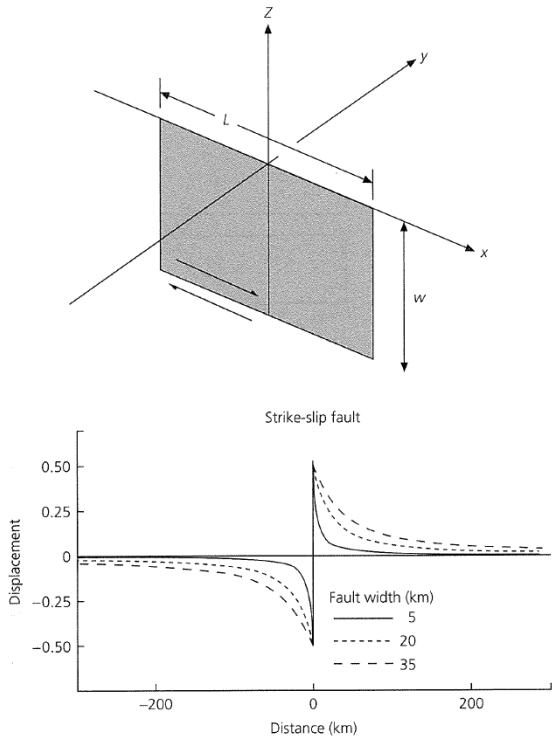

Figure 2.2: Static deformation observed near vertically dipping fault. Top figure showing geometry of strike-slip vertically dipping fault. Bottom figure showing the displacements observed near the fault. Different lines showing displacement models using different fault width (W). (Stein & Wysession, 2003).

The displacements are calculated using the following equation (Stein & Wysession, 2003).

$$u(y) = \pm D/2 - (D/\pi)tan^{-1}(y/W) \tag{2.1}$$

where, displacement $u(y)$ is a function of slip (D), distance from the fault in y direction and fault width (W). Slip (D) is assumed to be uniform all over the fault interface.

Figure 2.2 (Bottom) shows the displacements are higher near the fault and decrease with increasing distance from the fault. At the closest point near the fault, distance along y is close to zero. This yields maximum displacement with $u(y) \approx D/2$. On the other hand, when the distance along y is very far away from the fault, y/W is unlimited, this results $tan^{-1}(y/W) = 90$. Hence, at the observation point relatively far away from the fault, the displacement is zero.

Coseismic static surface deformation of finite rectangular faults, however, is more complicated. The decay of displacements at distances along y direction depends on the fault length (L) and width (W). One of the most popular models using finite rectangular fault was introduced by Okada (1985). He proposed a set of formula to calculate the surface deformation due to shear and tensile faults in a half space. In this thesis, we briefly introduce the set of formula to calculate the surface static displacement due to the simple case of a finite rectangular fault.

Surface static displacement can be derived using basic source parameters of the earthquake, namely centroid depth (d), strike, dip (δ), length of fault (L), width of fault (W), rake, slip (U) and an assumption of Poisson's ratio (see Figure 2.3). The predicted static displacement calculated at the coordinate of observation points on the surface.

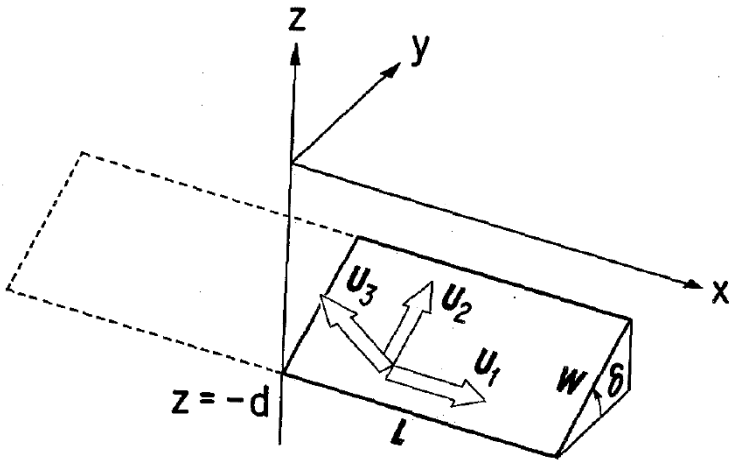

Figure 2.3: Geometry of the source model described by Okada (1985).

Vectors U_1, U_2 and U_3 in Figure 2.3 showing the dislocation on the fault surface due to the earthquake. The U_1, U_2 and U_3 correspond to strike-slip, dip-slip and tensile components, respectively. Vector U_2 shown in Figure 2.3 represents the typical of reverse fault dislocation. However, it can be changed to the normal fault if the dip angle (δ) becomes $sin\ 2\delta < 0$.

Surface deformation at observation point of coordinates x and y is represented by u_x, u_y and u_z. It can be calculated using the Eqs. 2.2, 2.3 and 2.4 below. The vectors u_x and u_y correspond to the surface displacement in horizontal x and y directions. Vector u_z corresponds to the surface displacement in vertical direction.

$$\begin{aligned} u_x = &-\frac{U_1}{2\pi}\left[\frac{\xi q}{R(R+\eta)} + tan^{-1}\frac{\xi\eta}{qR} + I_1 sin\ \delta\right] \\ &-\frac{U_2}{2\pi}\left[\frac{q}{R} + I_3 sin\ \delta\ cos\ \delta\right] \\ &+\frac{U_3}{2\pi}\left[\frac{q^2}{R(R+\eta)} - I_3 sin^2\delta\right] \end{aligned} \tag{2.2}$$

$$
\begin{aligned}
u_y = &-\frac{U_1}{2\pi}\left[\frac{\tilde{y}q}{R(R+\eta)} + \frac{q\,cos\,\delta}{R+\eta} + I_2 sin\,\delta\right] \\
&-\frac{U_2}{2\pi}\left[\frac{\tilde{y}q}{R(R+\xi)} + cos\,\delta\,tan^{-1}\frac{\xi\eta}{qR} - I_1 sin\,\delta\,cos\,\delta\right] \\
&+\frac{U_3}{2\pi}\left[-\frac{\tilde{d}q}{R(R+\xi)} - sin\,\delta\left\{\frac{\xi q}{R(R+\eta)} - tan^{-1}\frac{\xi\eta}{qR}\right\} - I_1 sin^2\delta\right]
\end{aligned}
\tag{2.3}
$$

$$
\begin{aligned}
u_z = &-\frac{U_1}{2\pi}\left[\frac{\tilde{d}q}{R(R+\eta)} + \frac{q\,sin\,\delta}{R+\eta} + I_4 sin\,\delta\right] \\
&-\frac{U_2}{2\pi}\left[\frac{\tilde{d}q}{R(R+\xi)} + sin\,\delta\,tan^{-1}\frac{\xi\eta}{qR} - I_5 sin\,\delta\,cos\,\delta\right] \\
&+\frac{U_3}{2\pi}\left[-\frac{\tilde{y}q}{R(R+\xi)} - cos\,\delta\left\{\frac{\xi q}{R(R+\eta)} - tan^{-1}\frac{\xi\eta}{qR}\right\} - I_5 sin^2\delta\right]
\end{aligned}
\tag{2.4}
$$

where,

$$
\begin{aligned}
I_1 &= \frac{\mu}{\lambda+\mu}\left[\frac{-1}{cos\,\delta}\cdot\frac{\xi}{R+\tilde{d}}\right] - \frac{sin\,\delta}{cos\,\delta}I_5 \\
I_2 &= \frac{\mu}{\lambda+\mu}\left[-ln(R+\eta)\right] - I_3 \\
I_3 &= \frac{\mu}{\lambda+\mu}\left[\frac{1}{cos\,\delta}\cdot\frac{\tilde{y}}{R+\tilde{d}} - ln(R+\eta)\right] + \frac{sin\,\delta}{cos\,\delta}I_4 \\
I_4 &= \frac{\mu}{\lambda+\mu}\cdot\frac{1}{cos\,\delta}\left[ln(R+\tilde{d}) - sin\,\delta\,ln(R+\eta)\right] \\
I_5 &= \frac{\mu}{\lambda+\mu}\cdot\frac{2}{cos\,\delta}\,tan^{-1}\frac{\eta(X+q\,cos\delta) + X(R+X)sin\,\delta}{\xi(R+X)cos\,\delta}
\end{aligned}
\tag{2.5}
$$

and if $\cos\,\delta \approx 0$,

$$
\begin{aligned}
I_1 &= -\frac{\mu}{2(\lambda+\mu)}\cdot\frac{\xi q}{(R+\tilde{d})^2} \\
I_3 &= \frac{\mu}{2(\lambda+\mu)}\left[\frac{\eta}{R+\tilde{d}} + \frac{\tilde{y}q}{(R+\tilde{d})^2} - ln(R+\eta)\right] \\
I_4 &= -\frac{\mu}{\lambda+\mu}\cdot\frac{q}{R+\tilde{d}} \\
I_5 &= -\frac{\mu}{\lambda+\mu}\cdot\frac{\xi\,sin\,\delta}{R+\tilde{d}}
\end{aligned}
\tag{2.6}
$$

where, λ and μ are Lame's constants.

$$\begin{aligned} p &= y\,cos\,\delta + d\,sin\,\delta \\ q &= y\,sin\,\delta - d\,cos\,\delta \\ \tilde{y} &= \eta\,cos\,\delta + q\,sin\,\delta \\ \tilde{d} &= \eta\,sin\,\delta - q\,cos\,\delta \\ R^2 &= \xi^2 + \eta^2 + q^2 = \xi^2 + \tilde{y}^2 + \tilde{d}^2 \\ X^2 &= \xi^2 + q^2 \end{aligned} \tag{2.7}$$

When $cos\,\delta = 0$, we must be careful that there are two cases on $sin\,\delta = +1$ and -1.

As noted by Okada (1985), ξ and η are obtained from the equation that involves Chinnery (1963) notation.

$$f(\xi,\eta)\,|| = f(x,p) - f(x,p-W) - f(x-L,p) + f(x-L,p-W) \tag{2.8}$$

We use a Matlab function based on Okada (1985) model written by Francois Beauducel from Institut de Physique du Globe de Paris (IPGP) to show the illustration how the method works. The code is available at url: $http://www.mathworks.com/matlabcentral/fileexchange/25982$ (last accessed August 2012). Using this Matlab function, we can calculate predicted surface deformations at the fixed observation coordinates on the earth's surface.

For an example, we calculate the predicted static displacement at a near-source observation point in Japan caused by the 2011, Mw 9.0 Tohoku earthquake. We selected an observation point at the same location with the GPS station 0175 (38.68N, 141.45E) of the GEONET network. In order to compare the predicted and observation data, we also

show the GPS data at the station for the reference (see Figure 2.4).

The fault size (A) from the product of rupture length (L) and width (W) is calculated using empirical scaling relations of moment magnitude and rupture area following Eqs. 2.9 and 2.10 (Wells & Coppersmith, 1994). We use moment magnitude of 9.0. The slip average is calculated using Eqs. 2.11 and 2.12 from (Kanamori, 1977) and (Hanks & Kanamori, 1979), respectively.

$$\log(L) = 0.63M_w - 2.86 \tag{2.9}$$

$$\log(W) = 0.41M_w - 1.61 \tag{2.10}$$

$$M_o = \mu\, D\, A \tag{2.11}$$

$$\log(M_o) = 1.5M_w + 9.1 \tag{2.12}$$

We adopted the commonly used constant elastic shear modulus $\mu = 30\,GPa$. We obtained $M_o = 3.98 \times 10^{22}\,N\,m$ and $D = 18.32\,m$. Where, M_o is seismic moment energy and D is the slip average of the whole rupture area on the entire fault surface. Lee et al. (2011) also shows that the slip average of the Tohoku earthquake is about 18 m.

In Figure 2.4 we show that by giving the simple input model of the source parameter, we can calculate the surface displacement by forward modeling. We give the input for Eqs. 2.2, 2.3 and 2.4 in the Matlab program with the fault length and width, hypocenter location, strike, dip, rake and slip of the Tohoku earthquake from the reference. The results of displacement model are 4.08 m, -1.88 m and -0.33 m, respectively for east-west, north-south and vertical components. These results are comparable with GPS measurements of the Tohoku earthquake at station 0175, which are 4.04 m, -1.61 m and -0.65 m for east-west, north-south and vertical components, respectively. The coseismic deformation theory described in a set of formulas above proposed by Okada (1985) works well for the Tohoku earthquake. A certain discrepancy of displacements data of observation and prediction is

of course expected, since Okada (1985) method makes simplification in his model e.g. fault dimension by assuming a rectangular rupture area and homogeneous slip.

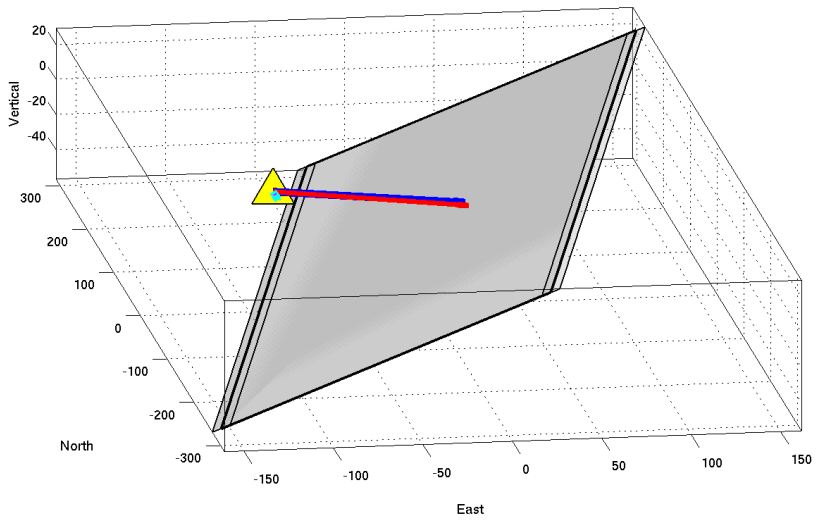

Figure 2.4: Example of surface deformation calculated using Okada (1985) model of the 2011, Mw 9.0 Tohoku earthquake. Blue and cyan arrows showing the observation displacement data at station 0175 (38.68N, 141.45E), respectively for horizontal and vertical components. Whereas red and magenta showing the predicted displacement calculated using Okada (1985) model. Yellow triangle indicates the location of GPS station 0175 and large gray square area represents the rupture area of the earthquake.

2.2 Observations of static deformation

Static deformations of the earth's surface due to strong shallow earthquakes or other phenomena can be recorded using GPS (Global Positioning System), InSAR (Interferometric Synthetic Aperture Radar) and seismic sensors. The three methods have advantages and limitations. All the methods are complementary to each other.

2.2.1 GPS

GPS station records the earth's surface deformation continuously with the observation time of 24 hours/day. GPS method determines the position of the antenna receiver or GPS station in 3 dimension. The GPS station receives the signal from the satellites. As on September 2012, there are 31 actively satellites in operational ($http://www.navcen.uscg.gov/Do = constellationStatus$). The satellites transmit the signals to GPS station from different directions at the same time.

The position of GPS receiver or station can be determined in the ways analogous to the earthquake hypocenter determination using several seismic stations by the simple mathematical method of trilateration. GPS station collects the information relies on the travel time of radio signals between satellites and ground stations. It collects the data from several GPS satellites. Such informations can be used to calculate the distance of GPS station to each satellite. The approximate position of GPS station can be estimated at the interception of at least 3 spherical distances of GPS satellites. Another or more data from GPS satellites need to improve the accuracy and to get the precise altitude information. GPS method determines the position of observation point two or three times more precise in the horizontal components compared to the vertical one. This is because the radio signals that are transmitted from the satellites, arrive at GPS station only from above. It is similar to the earthquake locations, particularly teleseismic events, which are less precise in depth because the seismic waves arrive at seismic stations only from below.

GPS data are collected in two modes. In survey mode or usually known as campaign GPS data, GPS antennas are installed temporary at interested locations. GPS campaign stations are usually used to observe coseismic and post-seismic deformation. Alternatively, GPS receivers are installed permanently. The stations record surface deformation con-

tinuously. Permanent GPS stations are used for most purposes, including observation of interseicmic deformation or global plate motion. They are also useful to be the survey monuments or base points of temporary GPS survey.

The limitation of GPS method, however, for the early warning tsunami or rapid hazard assessment, such geodetic measurement are less useful because they are usually available only with a time delay of days to weeks or even longer (Wang et al., 2011). It happens because, for a precise position, in general, GPS method estimates positions of receiver over long periods, ∼24 hours. The entire day or multiple days of GPS data are required to process retrieving a single average position of GPS station before and after the earthquake occurrence (Emore & Haase, 2007). Only continuous high-rate GPS may have the potential to provide real-time surface deformation data. Accurate GPS real-time processing, however, is not yet well established, and high-rate continuous GPS networks are rare (Wang et al., 2011).

2.2.2 InSAR

InSAR (Interferometric Synthetic Aperture Radar) on the other hand can produce the surface deformation without any receivers on the earth's surface. However, it can not produce the absolute position or deformation of the area but relative to the position of previous data. The absolute deformations can be obtained through further data analysis. An advantage of using InSAR method is that it can produce the deformation of a wide area at one time which can not be done by the GPS measurement. Another advantage is that InSAR method has a better estimation of the vertical deformation compared to GPS method.

InSAR data shows how the elevation of the earth's surface changes over the time. Synthetic Aperture Radar (SAR) observe the elevation by transmitting its signal to an area

and getting back the reflected signal from the area to its antenna. The deformation of an area can be analyzed by doing the same observation at the same area but at different times. The signal should be transmitted from the same position of SAR antenna. The frequency of the phases of each observation are collected and compared. Frequency differences of the phases imply the deformation of the area or changing of elevation.

InSAR method, however, has several limitations. It recovers ground motion only in the look direction of its antenna. Another limitation, it reads the images data from the ground surface without distinguishing that in some regions the images come from vegetation growth. In the area where no dominated vegetation, the method is powerful.

2.2.3 Seismic method

Compared to geodetic method (i.e. GPS), transient displacements due to propagating seismic waves which are generated by the earthquakes can be studied much better using data from seismic instruments like broadband or strong motion seismometer. For near-source stations, strong motion seismometer provides the best recording even for the earthquakes with the very large magnitude. Static deformation can also be derived from the records of strong motion seismometer after double integration is applied. The higher sampling rate of strong motion seismometers, allows the displacement time series to be analyzed in real-time. Compared to GPS and InSAR methods, this is an important advantage of seismic method. Another advantage is that strong motion seismometers record ground motion with higher dynamic range. Their relatively low cost also allow higher station density, especially in the seismically active area.

Geodetic station records the displacement directly, whereas the strong motion seismometer can produce the displacement by a double integration of the acceleration records. Strong motion records, however, have the problem with the baseline offsets. Most of the

strong motion records contain such offsets after the sensors experience the strong shaking. The problem gives the profound effects to the displacements when the waveforms are integrated twice. Therefore, the strong motion derived displacements require the baseline correction in the data processing. A more detail explanation of this issue is described in Section 2.4 “Strong motion derived displacement”.

2.3 Broadband and Strong motion seismometer

A typical broadband seismometer records ground velocity. The response of sensor is set up to be sensitive to low frequency ground motion. The response to ground velocity is flat at periods typically between 0.1 to 120 sec. The frequency of earthquake waves is less than 10 Hz, except the very small earthquakes (M $<$ 2), frequency of the waves is 10-1000 Hz (Havskov & Ottemöller., 2010). So that, the sensor can be expected to record the earthquake at its best performance. Broadband seismomenters record best teleseismic events at all magnitudes or local events at relatively small to moderate magnitudes. Strong near field earthquakes, however, normally recorded by the sensors offscale or clipped in the period of highest velocity.

A strong motion seismometer, on the other hand, designed to be relatively less sensitive to low frequency ground motion but more sensitive to the high frequency. The advantage of this type of sensors is that the near-source station can record relatively strong earthquakes without any saturation. Strong motion seismometers produce acceleration records. Velocity and displacement can be obtained by first and second integration of the accelerogram, respectively.

Strong motion seismometer basically uses the same pendulum mechanical system as it is used in the classical seismometer. The sensor consists of a mass, a spring and a

dashpot or damping device. To measure the ground motion, the sensor is desinged so that the motion of the pendulum is out of phase with the ground motion.

The sensor records the ground motion and converts it into a voltage. Ground motion can be described as displacement, velocity and acceleration. During the earthquake, the sensor is moving, following the ground shaking. As shown in Figure 2.5, the pendulum or mass in the sensor moves relative to the ground movements. Since the measurement is done in a moving reference frame, the principle of inertia dictates that only motions that cause acceleration (change of velocity in time) can be measured (Havskov & Ottemöller., 2010). Besides it, the dynamic range of seismometer is relatively very narrow to record the ground displacement directly, and even the ground velocity as it is recorded by the broadband seismometer, which is clipped at near-source station during the relatively strong earthquake recording.

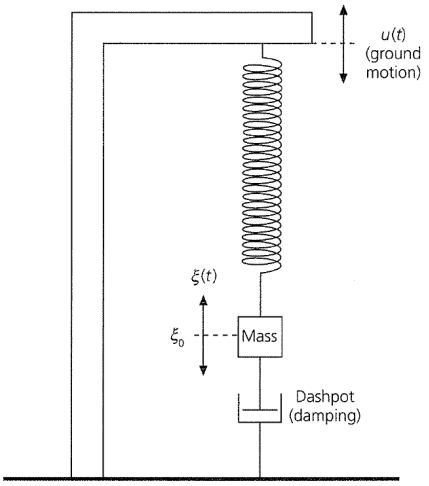

Figure 2.5: The principle of seismic sensor, a mass moves with the displacement $\xi(t)$ relative to the reference position (ξ_0) in response to ground movements ($u(t)$) (Stein & Wysession, 2003).

Basic equation of pendulum motion of the seismometer can be discovered in many literatures (Aki & Richards, 2002). The typical pendulum mechanical seismometer is a damped harmonic oscillator. A simple seismograph system as shown in Figure 2.5 detects vertical ground motion. Assuming the ground and pendulum move restricted to one di-

rection, $\xi(t)$ is denoted as the displacement of the pendulum with the mass (m) and $u(t)$ is the displacement of the ground. If the equilibrium length of the spring without ground motion is $\xi(0)$, the spring exerts the force proportional to its extension from the equilibrium position as a function of time, $\xi(t) - \xi(0)$, times a spring constant k. The damping system with damping constant d, exerts a force proportional to the relatives velocity $\dot{\xi}(t)$ between the mass (m) and the earth. So, the equation of the ground motion displacement $u(t)$ is given by

$$m\frac{d^2}{dt^2}\left[\xi(t) + u(t)\right] + d\frac{d\xi(t)}{dt} + k\left[\xi(t) - \xi_0\right] = 0 \tag{2.13}$$

if we define $\xi(t) - \xi(0)$ relative to the equilibrium position $\xi(0)$ as $\xi(t)$, the Eq. 2.13, becomes

$$m\ddot{\xi} + d\dot{\xi} + k\xi = -m\ddot{u} \tag{2.14}$$

or,

$$\ddot{\xi} + 2\varepsilon\dot{\xi} + \omega_0^2\xi = -\ddot{u} \tag{2.15}$$

where, $\varepsilon = d/(2m)$ and $\omega_0 = \sqrt{\frac{k}{m}}$. The single and double dots denote the first and second time derivatives, respectively. ω_0 is known as the natural frequency of the undamped pendulum mechanical system.

The Eq. 2.15 shows that if the ground moves very rapidly, the pendulum acceleration $\ddot{\xi}$ is very large and the term $2\varepsilon\dot{\xi} + \omega_0^2\xi$ can be neglected. Hence, the acceleration of the pendulum $\ddot{\xi}$ becomes nearly equal to the acceleration of the ground $-\ddot{u}$, in opposite direction. Whereas, if the ground moves very slowly, the term $\omega_0^2\xi$ becomes nearly equal

to $-\ddot{u}$. It follows the acceleration of the ground motion $-\ddot{u}$ reproduces the displacement of the pendulum ξ.

Eq. 2.15 can be solved by assuming that the response of such sensors to sinusoidal ground displacement $u(t) = e^{-i\omega t}$ can be written as $\xi(t) = X(\omega)e^{-i\omega t}$. These equations are substituded to Eq. 2.15 to yield

$$X(\omega)(-\omega^2 - 2\varepsilon i\omega + \omega_0^2)e^{-i\omega t} = \omega^2 e^{-i\omega t} \tag{2.16}$$

or,

$$X(\omega) = -\omega^2/(\omega^2 - \omega_0^2 + 2\varepsilon i\omega) \tag{2.17}$$

where, $X(\omega)$ is the transfer function or instrument response of the seismometer produced by the ground motion $e^{i\omega t}$ as shown in Figure 2.6.

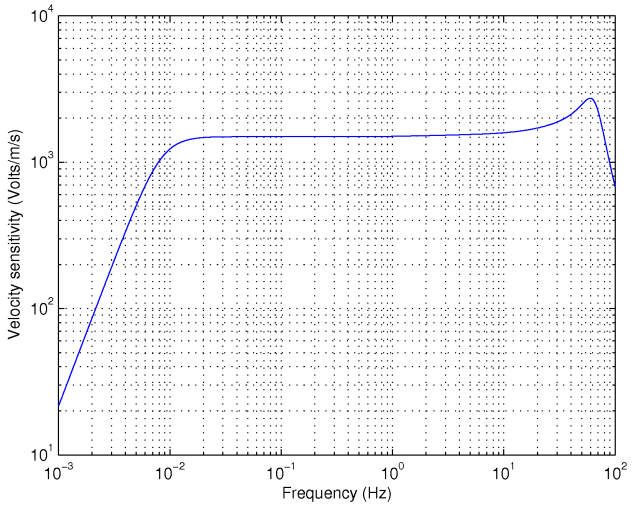

Figure 2.6: Instrument response of STS-2 broadband seismometer.

Transfer function of the seismometer shows the frequency response of seismometer to the ground velocity. The transfer function flat indicates the instrument experience

resonnance to the ground motion. In this frequency band, the pendulum of the sensor is shaked with nearly the same frequency of the ground motion. In this situation, the seismometer responds best the ground motion.

In principle, all seismic sensors have the same mechanical system as described above. Inside the sensors, the ground motion generates the voltage. The changes in the voltage generate current in coil. The feedback system leads the current to create a magnetic restoring and force the moving mass to original zero position. Thus, the current traveling through the coil is proportional to the ground acceleration. By passing this current through a complex impedance consisting of a resistor and tranducer it can be converted to a voltage output proportional to acceleration (Kinemetrics, 2005). So the voltage over the resistor gives a direct measure of acceleration. If we want to have the voltage proportional to velocity, the feedback system should be designed to integrate it. Therefore, the only difference between the two sensors of Force Balance Accelerometer and broadband STS-2 is the integration of the signal in the case of broadband STS-2.

The transfer function of an accelerometer follows the Eq. 2.18.

$$\frac{V(s)}{A(s)} = \frac{k1 * k2}{(s - p_1)(s - p_2)(s - p_3)(s - p_4)} \tag{2.18}$$

where,

$k1$ = 2.46 x 10^{13}

$k2$ = Sensitivity of sensor in V/g

s is the Laplace transform variable

p_1 = -981 + 1009i (Pole 1)

p_2 = -981 - 1009i (Pole 2)

p_3 = -3290 + 1263i (Pole 3)

p_4 = -3290 - 1263i (Pole 4)

$V(s)$ is the Laplace transform of the output voltage

$A(s)$ is the Laplace transform of the input acceleration

For Episensor Force Balance Accelerometer model FBA-EST (Kinemetrics, 2005) with the output of 10 V/g (where g is gravity constant 9.8 m/s^{-2}), the transfer function is shown in Figure 2.7.

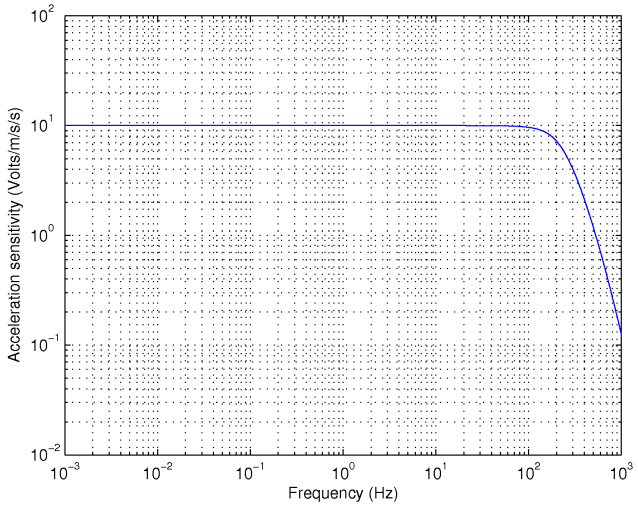

Figure 2.7: Instrument response of Episensor Accelerometer model FBA-EST.

The acceleration records obtained from the strong motion accelerometer have the frequency response flat for the earthquake recording. Thus, it is not necessary to remove the instrument response of the strong motion accelerogram to calculate the velocity and displacement (Emore & Haase, 2007).

2.4 Strong motion derived displacement

The Eq. 2.15 introduced earlier can be used as a basis for strong motion data processing. Since the accelerometer usually has relatively high natural frequency (ω_0), the term $\ddot{\xi} + 2\varepsilon\dot{\xi}$

in the Eq. 2.15 can be neglected. Thus, the equation can be simplified to

$$\omega_0^2 \xi = -\ddot{u} \tag{2.19}$$

Theoretically, velocity and displacement of the ground motion can be simple recovered by first and double integration of Eq. 2.19.

However, the seismometer, in fact, does not record only the translational motion as assumed in Eq. 2.15 but also tilt and rotational motion (Rodgers, 1968; Boore, 2001; Graizer, 2005, 2006, 2010). The equation of a horizontal pendulum oscillation given by Graizer (1989); Trifunac & Todorovska (2001); Graizer (2005). It can be written as:

$$\begin{aligned}
\ddot{\xi}_x + 2\omega_x d_x \dot{\xi}_x + \omega_x^2 \xi_x &= -\ddot{u}_x + g\psi_y - \ddot{\psi}_z l_x + \ddot{u}_y \theta_x \\
\ddot{\xi}_y + 2\omega_y d_y \dot{\xi}_y + \omega_y^2 \xi_y &= -\ddot{u}_y + g\psi_x - \ddot{\psi}_z l_y + \ddot{u}_x \theta_y \\
\ddot{\xi}_z + 2\omega_z d_z \dot{\xi}_z + \omega_z^2 \xi_z &= -\ddot{u}_z + g\psi_x^2/2 - \ddot{\psi}_x l_z + \ddot{u}_y \theta_z
\end{aligned} \tag{2.20}$$

where, index x and y for horizontal components and index z for vertical component; g is gravitational force vertically; ψ is a rotation of the ground surface; l is length of pendulum arm; and θ is angle of pendulum rotation. Other symbols have the same definition as in Eq. 2.15.

The Eq. 2.20 of pendulum oscillation for vertical component with index z has the term $g\psi_x^2/2$ on the right hand side. The term indicates the sensitivity of the sensor to the tilt effect. Boore (1999); Clinton (2004) and Graizer (2006) noted that this term becomes relatively very small for small angles (less than 10 degrees). The term $g\psi_x^2/2$ is proportional

to $g(1 - cos(\psi))$ for vertical component. Thus, for small tilts,

$$g\psi_x^2/2 = g(1 - cos(\psi)) \tag{2.21}$$

where, for small value of ψ, $cos(\psi)$ is $\sim$1, Hence, the term can be neglected. The equation for the vertical component becomes:

$$\ddot{\xi}_z + 2\omega_z d_z \dot{\xi}_z + \omega_z^2 \xi_z = -\ddot{u}_z - \ddot{\psi}_x l_z + \ddot{u}_y \theta_z \tag{2.22}$$

Thus, the vertical component sensitive only to acceleration of linear motion, angular acceleration and cross axis excitation, but not tilt. Whereas, the horizontal components are sensitive to all motions including tilt. The sensitivity response of horizontal components to the ground motion is more complicated than the vertical component.

The Eq. 2.20 that involves all effect regarding the ground motion are necessary to analyze the strong motion records perfectly. However, Rodgers (1968); Aki & Richards (2002) suggested the second, third and forth terms on the right hand side of the equation can be neglected for the teleseismic studies. The terms give the effect small enough to be neglected.

More detail about the effect of the terms on the right hand side of the Eq. 2.20 were studied (e.g. Graizer, 1989, 2006). Based on experiments, they confirm that the terms of angular acceleration and cross axis excitation can be neglected because the accelerometer has a short pendulum arm. Whereas the tilt effect can not be neglected because it gives the significant influence to the strong motion records, particularly for the horizontal components. Thus, the equation of pendulum oscillation with a short arm for the three components accelerometer follows:

$$\begin{aligned}
\ddot{\xi}_x + 2\omega_x d_x \dot{\xi}_x + \omega_x^2 \xi_x &= -\ddot{u}_x + g\psi_y \\
\ddot{\xi}_y + 2\omega_y d_y \dot{\xi}_y + \omega_y^2 \xi_y &= -\ddot{u}_y + g\psi_x \\
\ddot{\xi}_z + 2\omega_z d_z \dot{\xi}_z + \omega_z^2 \xi_z &= -\ddot{u}_z
\end{aligned} \tag{2.23}$$

The explanation given above describes the causality of baseline shift in the strong motion records. The tilt effect which proposed by many studies (Rodgers, 1968; Boore, 2001; Graizer, 2005, 2006, 2010), in fact, is discussed as one possible reason of the baseline shift. Iwan et al. (1985), based on their experiments, proposed another reason for the baseline shift in strong motion records. They found that during the strong shaking, the mechanical hysteresis in the sensors triggered the baseline shift. Boore (2003) also showed that analog-to-digital converter as a source of the the baseline shift.

In principle, we can remove the baseline shift of strong motion records using high-pass filter such as that by Chiu (1997). This method, however, is useful only for engineering purposes. It recovers the dynamic displacements of the records, but it will remove the content of low-frquency or static displacement of the records.

The problem of baseline shift in strong motion records influence significantly to the analysis of static displacement. The displacement can be calculated in principle by double integration of the acceleration data. If the baseline of the records shifted in a step function, even in a very small amplitude, the double integration will produce a profound effect. For instance, the two baseline offsets of 0.01 and 0.02 $cm\ s^{-2}$ of the acceleration data at station MYGH06 (see Figure 2.11) produce the unrealistic displacements. It produces about 500 cm displacement after approximately 250 sec. The first integration yields the velocity with the large drift and the second integration produces unrealistic displacement, usually in the quadratic pattern. Therefore, it is impossible to get a reasonable displacement without

any correction applied to double integration process.

Theoretically, at the beginning of the strong motion records, the baseline is exactly at zero position. The sensor records only noise of the ground motion. So that, if DC (Direct or continuous Current) offset observed, it should be first removed in the data processing. Whereas, during the eartquake, the sensor records the strong ground motion. If the earthquake is relatively large, normally, we observe the ground motion can move the sensor to another new position. Just after the earthquake occurrence, the sensor stays at zero velocity at its new position. Therefore, basically, the baseline correction method attempts to adjust the baseline of velocity trace to be at zero position before and after the earthquake occurrence.

As it was described above, the ground motion shakes the sensor not only in linear motion but also results in tilt and rotational motion. Therefore, the strong motion records are contaminated by tilt or rotational effect. If we are interested only in the translational motion, the tilt or rotational effect needs to be removed. Such tilt or rotational motion of the ground, can in principle be measured independently by rotational sensors (Schreiber et al., 2009). The sensor would have to be installed at the same location with the strong motion seismometer. Using rotational data of the sensor, theoretically, the tilt effect can be romoved from strong motion records, properly.

In practice, however, it is not feasible. Rotational sensors can only be found in a very small numbers of stations in certain locations. They can not be expected to be part of routine strong motion data processing (Wu & Wu, 2007; Wang et al., 2011). The only solution at this moment is by removing baseline shifts with the empirical method of baseline correction.

2.5 Laboratory Experiments

Many studies (e.g. Trifunac (1971); Iwan et al. (1985); Boore (2001, 2003); Wu & Wu (2007); Chao et al. (2009) and Wang et al. (2011)) discussed the sources of baseline shifts and provide methods of baseline correction to recover the correct displacements. To make a summary, in several cases they found that the sources of baseline shifts are hysteresis in the sensors during the strong shaking, problems of analog-to-digital converter and ground tilting or rotation during the strong shaking due to earthquake. However, as noted by Boore (2001), in most cases, the source of baseline offsets is still unknown. Therefore, it is very difficult to provide the proper method of baseline correction on the physical basis. Alternatively, many studies provide the methods based on empirical formulas.

In this section, in order to investigate the causality of baseline shifts in the strong motion accelerometric data, we conducted an experiment of strong motion recording using a shaking table. We assume that the real strong motion data are contaminated by tilting or rotation of the ground during strong shaking due to the earthquake. If it is true, the baseline shift should not be observed in the strong motion recording using shaking table. In the experiment, an accelerometer is moved on the controlled shaking table. The shaking table is designed with the high accuracy linear displacement driver. So that, it is virtually impossible for tilt to occur during the experiments. This study is expected to strengthen the hypothesis, that the baseline shifts in "real" strong motion records are caused by ground tilting or rotation.

2.5.1 Experiments

The experiments were conducted at GFZ-Potsdam (German Research Center for Geoscience). We used an Episensor force balanced accelerometer, model FBA ES-T (Kinemet-

rics, 2005) for trace recording. As shown in Figure 2.8, the sensor was installed on the GSK-166 Uniaxial linear shaking table from GeoSIG (Geosig, 2009). The shaking table is computerized and controlled by GeoDAS software (Razinkov, 2012). The data is recorded by an EDL data logger, with the sampling rate of 100 Hz.

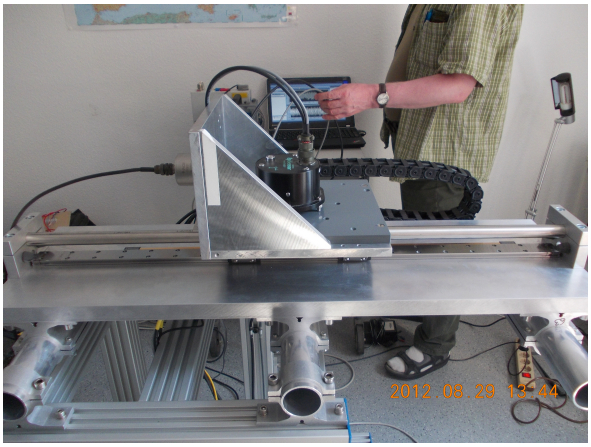

Figure 2.8: Experiments of strong motion data recording by using shaking table.

The shaking table was configured to work in horizontal direction. In principle, vertical direction is also possible but due to technical problems, we only conducted the experiment in horizontal movements. The table can move with a maximum displacement of about ±30 cm, if the zero position is at the center of shaking table. However, if the start position is moved to the edge of the shaking table, it can move maximum about ±60 cm. In our experiments, we give the input of static displacements to the shaking table in the range of 10 to 60 cm (see Table 2.1).

2.5.2 Results of experiments

Table 2.1 and Figure 2.9 show the results of experiments of strong motion data recording using the shaking table. We conducted several experiments with the given static displacements of 10, 20, 30, -40, -50, -60 cm. We also made an experiment of vibration recording. The sensor was shaked with zero static displacement.

The acceleration data was recorded during the experiments. We recover the static displacements from acceleration time series by double integration. We first removed the pre-event mean of the traces, which produces the recordings are started at zero baselines. Then, we apply double integration in time. As shown in Figure 2.9, first integration yields velocity time series and second integration yields displacement time series.

On the velocity traces, it is clear to see the peak velocity of sensor movement at the middle of velocity time series. The velocity starts from zero and increases until it reaches the maximum value in the middle point. After this point, the velocity starts decreasing to zero. At this time point, the sensor already reachs new permanent position.

The recorded amplitude of static displacements are measured from displacement traces, as seen in Figure 2.9 on the third column. The traces were obtained after double integration was applied. Complete results for all static displacements recovered by double integration of acceleration traces are shown in Table 2.1.

Table 2.1: Static movements of accelerometer applied to the shaking table

Nr.	**Static Displacements (cm)**	
	Input	**Recovered**
1	10	10.24
2	20	20.17
3	30	30.68
4	-40	-40.52
5	-50	-52.80
6	-60	-63.36
7	0	-0.27

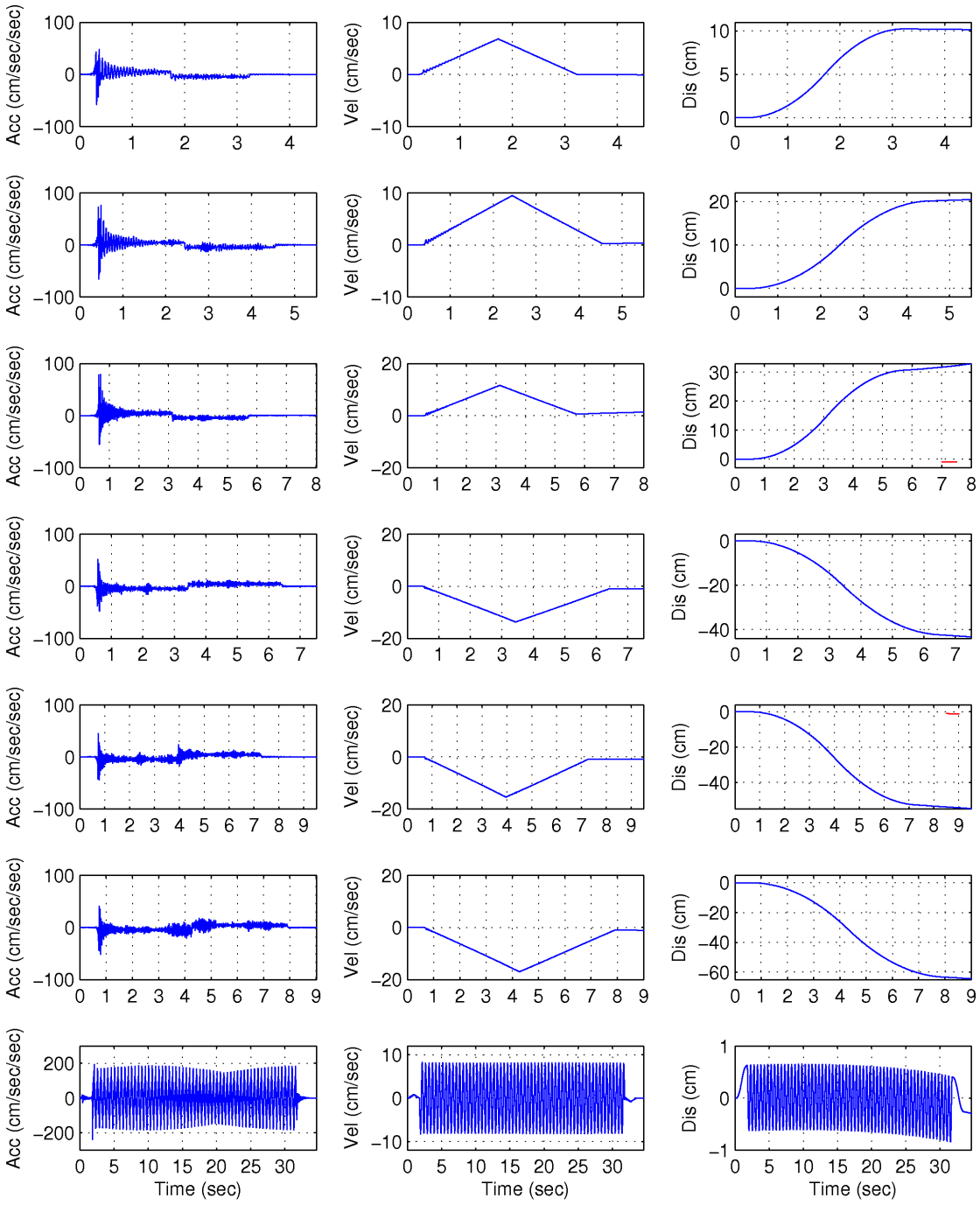

Figure 2.9: Results of experiment for strong motion recording using shaking table. The input of static displacements to shaking table following Table 2.1, respectively from top to buttom figures.

In general, the results show that the given input of static displacements were very well recovered by simple double integration data processing. The misfits were very small, with the average value for seven experiments being 1.15 cm. A relatively very small tilt was observed in the experiments data, for examples, in experiments of 40, 50 and 60 cm of static displacements (pers. comm. Karl-Heinz Jäckel). For such scale of static displacements, however, the shifts due to such very small tilt were still in a tolarable range. These results imply that likely the relatively larger baseline shift observed in the real strong motion data are contaminated by ground tilting.

2.6 Empirical baseline correction for strong motion records.

Several methods can be applied for baseline correction of acceleration data. The method proposed by Iwan et al. (1985) has become the basis for many improvements. From their experiment, Iwan et al. (1985) found that the drift in strong motion derived displacement is caused by baseline shifts in the acceleration data. They observed two baseline shifts during and after the strong shaking. These boxcar or parallel to zero-line shifts in the acceleration data, can usually only be observed as the trend in the velocity trace after the first integration is applied. However, recently, for the very large magnitude Mw 9.0 of the Tohoku earthquake in 2011, we found that the baseline shifts can clearly be observed even in the acceleration data for several records (e.g. see Figure 2.10a). The baseline shift can exceed $\sim 5\ cm\ s^{-2}$.

Using the method of bilinear line fitting, Iwan et al. (1985) proposed the time points T1 and T2 as the times of the baseline shifts in the acceleration data. Their algorithm is illustrated in Figure 2.11. Based on laboratory observation, they proposed the thresholds

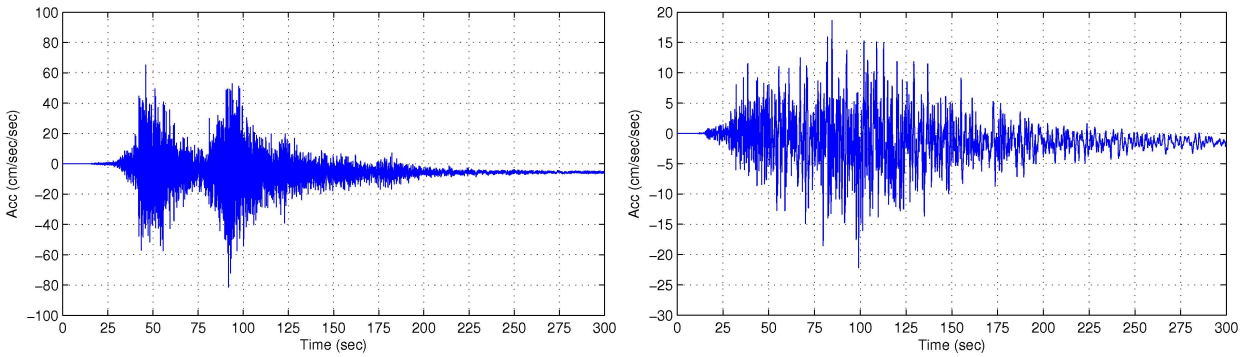

(a) **(b)**

Figure 2.10: (a) Accelerogram of the 2011, Mw 9.0 Tohoku earthquake recorded at KIK-net station IWTH05 ($\sim$ 133 km from hypocenter). The baseline shift of $\sim$5 $cm\ s^{-2}$ after the strong shaking can be seen clearly. (b) the same earthquake recorded at station YMTH08 ($\sim$ 272 km from hypocenter). Both traces in (a) and (b) show the vertical components.

for T1 and T2 when the acceleration exceeds 50 $cm\ s^{-2}$. The velocity trace is divided into three segments. The first segment begins at T1 when the acceleration first exceeds 50 $cm\ s^{-2}$, it ends at T2 when the acceleration never again exceeds 50 $cm\ s^{-2}$. The second segment starts at T2 and spans until the end of acceleration record. The remaining segment is the trace before T1. They also proposed another option for T2, namely the time point at which the final net displacement is minimized. The uncorrected velocity trace of the first and second segments are fit linearly using Eqs. 2.24 and 2.25, where $V_c(t)$ is the fitted line in the second segment with slope a_f. The slope of the first segment is given by a_m. Linear fits of the velocity traces in the first and second segments are subtracted from the uncorrected velocity trace. The corrected displacement can then be obtained by integrating the corrected velocity trace.

$$V_c(t) = V_0 + a_f t \tag{2.24}$$

$$a_m = \frac{V_c(T_2)}{T_2 - T_1} \tag{2.25}$$

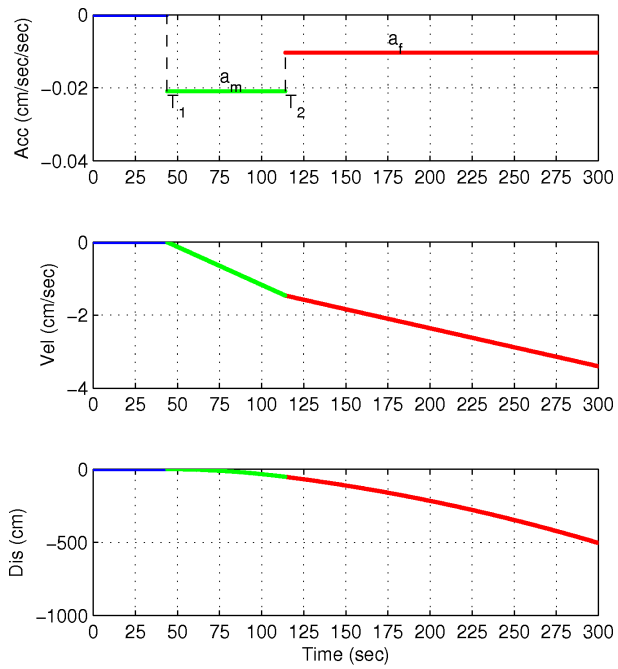

Figure 2.11: Baseline correction method by Iwan et al. (1985), based on the baseline shifts of real strong motion data of the 2011, Mw 9.0 Tohoku earthquake at station MYGH06 (38.591N,141.07E) east-west component.

Based on the method described by Iwan et al. (1985), Wu & Wu (2007) proposed a new approach by introducing a flatness parameter. They proposed to use the flatness of displacement traces as a boundary condition in the integration. According to (Wu et al., 2006a,b) the corrected displacement trace should be very flat after the ground reached its permanent displacement position. As shown in Figure 2.12, they proposed another time point T3 to help indicating the maximum flatness of displacement trace. The flatness of displacement trace from T3 to the end of record is calculated using Eq. 2.26. They also define the physical meaning of T1 as the time when the ground displacement starts to move away from zero position and T3 when the ground displacement has just reached the permanent position.

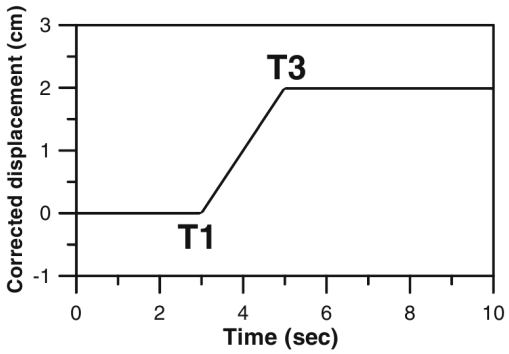

Figure 2.12: The ramp function of displacement trace proposed by Wu & Wu (2007). The flatness of displacement trace is observed to determine corrected displacement. T1 is time point when the ground displacement starts to move from zero position. T3 is time point when the ground displacement has just reached the permanent position.

$$f = \frac{|r|}{|b|\,\sigma} \tag{2.26}$$

where,

f = flatness

r = correlation coefficient

b = slope of LSQ

σ = variance

Chao et al. (2009) and Rupakhety et al. (2009) criticized that the time points in Wu & Wu (2007) correction procedure are determined by artificial choices in a recursive process. There is no objective criterion when the iterative scheme of the method to determine the time points should be stopped. Therefore, Chao et al. (2009) proposed an automatic and objective procedure to determine time points T1 and T3 for the Wu & Wu (2007) method. As suggested by Wu et al. (2006a,b) and Wu & Wu (2007), Chao et al. (2009) applied the ratio of cumulative energy following Eqs. 2.27 and 2.28 as the threshold for the time points, where E_t and E_r are the cumulative energy and its ratio, respectively. The n_p is

P-wave arrival time and n_c is the points of T1 and T3. N is the total number of data samples and a_i is the acceleration value of the i-th time point.

$$E_r = \left(\sum_{i=n_p}^{n_c} \frac{a_i^2}{E_t} \right) \times 100(\%) \tag{2.27}$$

$$E_t = \sum_{i=n_p}^{n_p+N} a_i^2 \tag{2.28}$$

They assume T1 is located within the time window containing the first 50% of energy distribution in acceleration data, whereas T3 is located on the last 50%. By testing all possible positions of T1 and T3 they constrain the results with the nearby GPS or references data. This technique was applied to the data set of the 2003, Mw 6.8 Chengkung earthquake with the reference of displacement results in Wu & Wu (2007). They use 27 stations of strong motion data set of the earthquake. They found that the minimum misfit between strong motion derived displacement and nearby references data can be reached at the position of 25% and 65% of cumulative energy for T1 and T3, respectively.

Chao et al. (2009) validated their method with the data sets of the 2006, Mw 6.1 Taitung eathquake and several records of the 1999, Mw 7.6 Chi-chi earthquake. Results of study in Wang et al. (2011) also show that the method by Chao et al. (2009) works well for the 2007, Mw 7.7 Tocopilla earthquake, in particular for the near-field data.

We apply the methods proposed by Chao et al. (2009) to several data set of strong earthquakes (see e.g. Figure 2.13). We use data set of the the 2007, Mw 7.7 Tocopilla earthquake, northern Chile (Schurr et al., 2009). This data was also used by (Wang et al., 2011) but in this study we show some additional data from University of Chile (Boroschek et al., 2008); the 2010 Mw 7.8 Mentawai earthquake, Sumatra (Wjayanto, 2007; Muzli et al., 2011); the 2003, Mw 8.3 Tokachi-Oki earthquake, Japan and the 2011, Mw 9.0

Tohoku earthquake, Japan (KiK-Net data, Aoi et al. (2004)). We also apply the method by Iwan et al. (1985) to all data sets, except for Mentawai earthquake. Peak Ground Acceleration (PGA) of the Mentawai earthquake at near-source station (PPSI, distance of ∼81 km from epicenter) is 23.8 $cm\ s^{-2}$. Using Iwan et al (1985) method, we calculate the static displacement for the data which have PGA larger than 50 $cm\ s^{-2}$. Whereas using Chao et al. (2009) method, we calculate the displacement of all data.

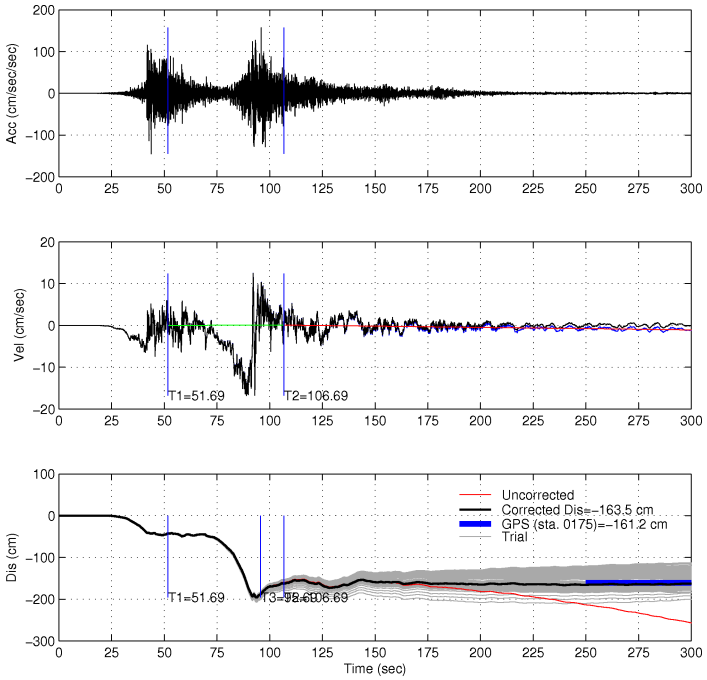

Figure 2.13: An example of data processing using Chao et al. (2009) method for the acceleration data of the 2011, Mw 9.0 Tohoku earthquake recorded at station MYGH12 (north-south component). The empirical time points T1 and T3 are determined based on the 25% and 65% of cumulative energy ratio, respectively. The T2 position was selected which produces the maximum flatness of displacement trace as suggested by Wu & Wu (2007).

Using a grid search method, Chao et al. (2009) found the best position of T1 and T3 for all data without taking into account the stations to hypocenter distance. We apply a similar technique as described by Chao et al. (2009) to find the best position of T1 and T3 for the whole data set of Tohoku earthquake. Considering different behaviour of horizontal and vertical components on their response to the tilt effects, we distinguish our

model for horizontal and vertical components. Moreover, in this study we search for the best position of T1 and T3 gradually for each group of data set at different distances of stations to hypocenter location. We use all data within the distance of 650 km. In total, 975 waveforms from 325 stations have been selected. We apply the grid search technique by generating all possible positions of T1 from 1% to 50% and T3 from 51% to 98% with the interval of iterations being 1% of cumulative energy of each seismogram. Determination of T1 and T3 are optimized so that the final strong motion derived displacement best fits the nearby GPS data.

A problem of nearby GPS data occurs when the study area has sparse GPS stations. However, using a slip distribution model of the earthquake from references, we can calculate surface deformation exactly at the locations of seismic stations by a forward modelling technique. This method can be done e.g. using SDM code written by R. Wang, which has been used in many publications (e.g. Wang et al., 2011, 2012; Altiner et al., 2012). Nevertheless, for case studies in Japan, the method is not necessarry because of the high density of GPS stations in Japan (GPS Earth Observation Network, GEONET, Sagiya et al. (2000)).

We calculated the misfit of strong motion derived displacements and displacements obtained from nearby GPS data. We then calculate the average of misfit contours for each group of data within the intervals of 25 km. To avoid domination of extremely large outliers in the average calculation, we first normalized each misfit contour to value 1 as the maximum. We then selected the position of T1 and T3 which has the minimum misfit and correlate it with the hypocenter distance. As results, we establish the relations of ratio of cumulative energy of T1 and T3 as function of distance for horizontal and vertical components. the relations are then used to improve the results of static displacement calculated from strong motion records.

In order to test our improvements to the method, we have selected data with significant static displacements within coordinates 35.5N to 41N and 139E to 143E. There are 151 strong motion stations in this area. We removed three stations from the data set which have unusual large shift that can be seen even in the acceleration traces. These are stations YMTH08 (38.970N,140.03E), IWTH05 (38.865N,141.35E) and FKSH04 (37.451N,139.81E). As reported by Clinton (2004) the largest tilts in strong motion records occur as consequence of local site failure such as lateral spreading or liquefaction. It is also possible that the sensors were not properly fixed to the ground. We also removed other 5 stations with too short pre-event data (less than 1 sec). The pre-event offset is very difficult to be removed from the waveforms which have very short or no pre-event data.

For the vertical components, we found that the results by using method of Chao et al. (2009) are not satisfactory. To test our improvements, we have selected only the results (using method of Chao et al. (2009)) with the deviations of vector length less than ten times relative to the GPS measurements. Using this additional criteria we collected 113 stations within the area.

We compare the results of displacement obtained by using Chao et al. (2009) method and the proposed relation of T1 and T3 as function of hypocentral distance in this study. To do so, we calculate difference vectors between the strong motion derived displacement and the GPS measurements for both methods. We distinguish two kinds of differences, deviation of vector length and deviation of vector azimuth or displacement directions. We show the displacement vectors, deviation contour and average of absolute deviation for the horizontal and vertical components by using Chao et al. (2009) method and improvement method.

For the next investigation we intend to speed up the method of baseline correction. This can be done by employing the relation of arrival time of empirical T1 and T3 with the

distance of station to hypocenter location. Using empirical T1 and T3 based on cumulative energy distribution, we observe the arrival time of T1 and T3 for each waveform data. We derive a relation between arrival time of T1 and T3 with the distance of station to hypocenter location.

We can obtain the hypocentral distance very quickly because the first location of hypocenter can be calculated soon after at least four P-wave arrival time are recorded at four nearest stations. Starting with the first preliminary hypocenter, we can calculate the position of T1 and T3 using such relation above. For the early warning purposes, it is very important to release the reasonable information as soon as possible. It is not necessary to calculate the cumulative energy distribution, nor to wait until the waveform reach its total 100% of energy. The quality of results can be improved incrementally when the new data arrive at the station.

Chapter 3

Data and Resources

3.1 The 2003, Mw 8.3 Tokachi-Oki earthquake

We use strong motion records of the 2003, Mw 8.3 Tokachi-Oki earthquake, Japan from the KiK-Net strong motion network. The network is operated by NIED (National Research Institute for Earth Science and Disaster Prevention), Japan (Aoi et al., 2004). KiK-Net provides two kinds of data, from the sensors installed in the boreholes and on the ground surface. The data has the sampling rate of 200 Hz. Considering the better quality of data according to the sensors location as also noted by (Wang et al, 2012), we use only the KiK-Net data of the borehole stations. The borehole sensors are installed within hard rock at depths larger than 100 meters from the ground surface. The deepest sensors are about 2000 meters deep. Most of them, however, are installed at depths between 100 to 200 meters of depth (Aoi et al., 2004).

Due to difficulties to adjust the azimuth of borehole sensors, some of the sensors may be rotated away from normal north-south and east-west directions. The orientation of KiK-Net borehole sensors are considered to be the same with Hi-Net sensors because

they are installed in the same containers. The official website of Hi-Net network provides the orientations of the sensors (see $http://www.hinet.bosai.go.jp/\ st\_info/detail/$, last accessed December 2011). We show the data of sensors orientation used in this study for data sets of the Tokachi-Oki and Tohoku earthquakes (see Appendix A).

The first preprocessing step before using the data is rotation of the acceleration data with the provided orientation angle using Eqs. 3.1 and 3.2. We then remove the pre-event mean from all acceleration records in order to get the onset of P-wave arrival at zero baseline. Due to data quality problems of signal to noise ratio and less interest in relatively far-field data, we use only data within a distance of 400 km from hypocenter location. We collected 375 waveforms from 125 three components strong motion stations.

$$N_{corr}(t) = cos(\theta) * N(t) - sin(\theta) * E(t) \tag{3.1}$$

$$E_{corr}(t) = sin(\theta) * N(t) + cos(\theta) * E(t) \tag{3.2}$$

Where, $N_{corr}(t)$ and $E_{corr}(t)$ are the corrected north-south $N(t)$ trace and east-west $E(t)$ trace, respectively. θ is the sensors orientation angle in the borehole.

We also use the GPS data to compare our results. The GPS coseismic displacements data are obtained from (Larson & Miyazaki, 2008).

3.2 The 2007, Mw 7.7 Tocopilla earthquake

Dozens of accelerometers from strong motion network in North Chile recorded the earthquake. In total, 48 waveforms from 16 three component stations have been selected. Eleven stations among them are operated by Integrated Plate Boundary Observatory Chile (IPOC) project (Schurr et al., 2009). Other five stations are operated jointly by the University of

Chile, Swiss and German institutions (Boroschek et al., 2008). The stations are surrounding the epicenter of earthquake within a radius of less than 350 km. The same data was used by previous studies of e.g. rupture process (Peyrat et al., 2010), analysis of high frequency pulses (Ruiz et al., 2010), and coseismic static surface deformation (Wang et al., 2011).

Table 3.1: Strong motion seismometer stations in North Chile

Sta	**Lat(E)**	**Lon(W)**	**Distance (km)**	**Owner**
PB4	-22.33369	-70.14918	50.139	IPOC
TCP	-22.09	-70.20	55.673	Univ. of Chile
PB7	-21.72667	-69.88618	70.531	IPOC
PB6	-22.70580	-69.57188	73.53	IPOC
PB5	-22.85283	-70.20235	85.32	IPOC
PB2	-21.31973	-69.89603	110.74	IPOC
CALA	-22.45	-68.93	115.96	Univ. of Chile
MEJI	-23.10	-70.45	119.86	Univ. of Chile
PB1	-21.04323	-69.48740	146.77	IPOC
PAT	-20.82071	-70.15288	166.2	IPOC
ANTO	-23.68	-70.41	173.57	Univ. of Chile
SPDA	-22.91	-68.20	205.32	Univ. of Chile
HMB	-20.27822	-69.88791	222.49	IPOC
PB8	-20.14112	-69.15340	251.16	IPOC
PSG	-19.59717	-70.12305	298.29	IPOC
MNM	-19.13108	-69.59553	350.03	IPOC

For the reference of our study, we use GPS data from Béjar-Pizarro et al. (2010). The data were obtained from the North Chilean cGPS network. In this network, 11 cGPS stations are distributed between the coastline and ∼300 km east of the trench in the continent. It covers well the deformed zone caused by the 2007 Tocopilla earthquake.

3.3 The 2010, Mw 7.8 Mentawai earthquake

For the 2010, Mw 7.8 Mentawai earthquake in Sumatra, we use the strong motion data from the strong motion network of Meteorological, Climatological and Geophysical Agency of Indonesia (BMKG) (Wjayanto, 2007; Muzli et al., 2011). The network was running in operational state after 2005. In total, 105 accelerometers have been deployed until the end of 2010. All of them were installed covering the prone area of large earthquakes in Indonesia. Several stations are operated in collaboration with GFZ-Potsdam and other international institutions.

The strong motion network of BMKG is equipped with two kinds of accelerometers: Triaxial Seismic Accelerometer (TSA-100S) and BBAS-2 Force-Balanced Accelerometer. TSA-100S sensor has the measure range of $\pm 4g$, wide frequency rensponse and high accuracy (ultra low non-linearity and hysteresis). BBAS-2 sensor has the sensitivity $2.5V/g$ and the measure range of $\pm 4g$. The stations equipped with the TSA-100S sensor have the sampling frequency $80Hz$, whereas the stations with BBAS-2 sensor have the lower sampling frequency $40Hz$.

Table 3.2: Strong motion seismometer stations in Sumatra

Sta	Lat(S)	Lon(E)	Distance (km)	Sensor type
PPSI	-2.766	100.01	83.123	TSA-100S
MKBI	-2.447358	101.239601	171.1	TSA-100S
LHSI	-3.826624	103.52333	380.9	TSA-100S
MDSI	-4.486037	104.17823	465.1	TSA-100S
LWLI	-5.017472	104.058914	470.26	BBAS-2
MNSI	0.795498	99.579627	479.16	TSA-100S
KASI	-5.52361	104.495964	536.9	TSA-100S
SBSI	1.398759	99.430938	547.65	BBAS-2
KLI	-4.836292	104.870452	549.28	TSA-100S

We collected the data of the 2010, Mw 7.8 Mentawai earthquake recorded by the network. Twenty-seven waveforms from 9 stations have been used in this study. Despite only a few stations being close to the epicenter location, we still see significant coseismic displacement at a number of stations.

3.4 The 2011, Mw 9.0 Tohoku earthquake

The same data source as it was used for the 2003, Mw 8.3 Tokachi-Oki earthquake above (see Section 3.1), has been used for the data set of the 2011, Mw 9.0 Tohoku earthquake. The sampling rate of the data set, however, has been changed between the time of earthquake occurrence to 100 Hz. We apply a similar process of data preparation to the Tohoku earthquake data set as we did for the Tokachi-Oki earthquake data set.

The Tohoku earthquake caused a very large static surface deformations. Therefore, we use data within a distance of 650 km from the hypocenter location. We collected 975 waveforms from 325 three components strong motion stations.

In order to compare our results, we use the GPS coseismic displacement data version 2.0 provided by the ARIA (Advanced Rapid Imaging and Analysis) team at JPL (Jet Propulsion Laboratory) and Caltech (California Institute of Technology). The original data were provided to Caltech by the Geospatial Information Authority (GSI) of Japan. The data are available at $ftp://sideshow.jpl.nasa.gov/pub/usrs/ARIA/$ (last accessed December 2011). The displacements measured are difference between solution at 5:00 and 6:30 UTC (the earthquake origin time was at 5:46:24 UTC), based on 30 minutes solutions.

Chapter 4

Results

4.1 Comparison of results using existing methods

In this section, we show the results of static displacements calculated from strong motion data using two existing methods. The methods were proposed by Chao et al. (2009) and Iwan et al. (1985). We apply both methods to several strong earthquakes. We also show the GPS data from the references in order to compare the results.

4.1.1 The 2003, Mw 8.3 Tokachi-Oki earthquake

Tokachi-Oki earthquake occurred near the northern Japanese island of Hokkaido on September 25, 2003, with a moment magnitude 8.3. The origin time was at 19:50:06 UTC. The epicenter was located at 41.775N and 143.904E with the hypocenter at 27 km depth. The results of reverse fault focal mechanism and earthquake depth imply that it occurred as the result of thrust-faulting on the plate interface between the overriding North American plate and the subducting Pacific plate.

The earthquake was recorded by the dense seismic and GPS networks. At the time of the earthquake, three large seismic networks were operated by NIED (National Research Institute for Earth Science and Disaster Prevention), Japan. They are F-NET, K-Net and KiK-Net. F-Net is a full-range broadband seismographic network. K-Net or Kyoshin-Net is the accelerometer network installed at free-field sites, on the ground surface. KiK-Net or Kiban Kyoshin Net is the accelerometer network installed in the boreholes and on the ground surface. Considering the better quality of strong motion data as noted by Wang et al. (2012), we used only KiK-Net boreholes data to calculate the static displacements due to the Tokachi-Oki earthquake. The static displacements recorded by the GEONET GPS network obtained from Larson & Miyazaki (2008), were used to compare the results of strong motion derived displacements.

The Tokachi-Oki earthquake produced coseismic deformations over a relatively wide area. From the results of strong motion derived displacements using the method by Chao et al. (2009), as shown in Figure 4.1, the largest amplitude of static displacements were recorded at station TKCH08 with the displacements of 66.985 cm, -32.975 cm and -28.835 cm, respectively for east-west, north-south and vertical components. The station is located at the coordinates of 42.486N and 143.15E, about 101 km from epicenter location. At a distance of about 314 km, which is relatively far from the epicenter, the station SBSH01, located at 43.234N and 140.62E, recorded considerately the smallest displacements with the amplitude of about 4.64 cm, -2.90 cm and 0.40 cm, respectively for east-west, north-south and vertical components. Some stations e.g. SRCH01, KKWH09 and SOYH08 show unrealistic displacements, which are most likely caused by local sites failure. However, in general, the strong motion derived displacements of all 125 stations, either horizontal or vertical components, are in good agreement with the GPS data from Larson & Miyazaki (2008). Using the method of Iwan et al. (1985), the results also show the displacements are comparable to nearby GPS data. Using this method, however, we calculated displacements

only for the strong motion records which have the Peak Ground Acceleration (PGA) larger than 50 $cm\ s^{-2}$. This is because of the Iwan et al. (1985) method determines the time points in the baseline correction based on the threshold when acceleration exceeds 50 $cm\ s^{-2}$.

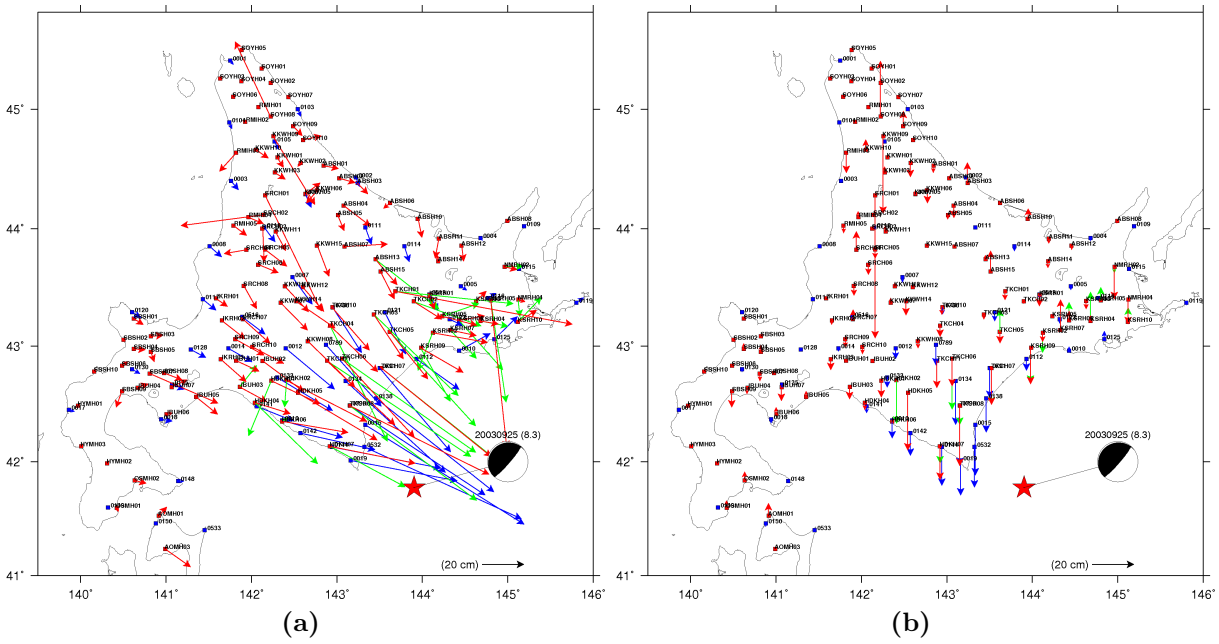

Figure 4.1: (a) Strong motion derived displacements for horizontal components calculated by Chao et al. (2009) and Iwan et al. (1985) methods are shown by red and green arrows, respectively. Blue arrows showing the GPS data from Larson & Miyazaki (2008). Large red star indicates the mainshock location of the earthquake. The beach ball shows the focal mechanism solution from GCMT. (b) Same as Figure 4.1a but for the vertical component.

4.1.2 The 2007, Mw 7.7 Tocopilla earthquake

The Mw 7.7 Tocopilla earthquake occurred on November 14, 2007 at 15:40:50 UTC. The hypocenter was located at 22.20S and 69.87W and at a depth of 40 km. The region has been identified as the location of a seismic gap (Kelleher, 1972). The earthquake took place at the slab interface between subducted Nazca plate and the South American plate. It was the largest thrust earthquake in this region since the last strong earthquake of 1995, the Mw 8.0 Antofagasta earthquake.

The Tocopilla earthquake was very well recorded by a permanent broadband and strong motion network in northern Chile. The network is a join colaboration of the Helmhotz-Zentrum Potsdam, Deutsches GeoForschungsZentrum (GFZ) of Germany, Institut de Physique du Globe de Paris (IPGP) of France and the Geophysics Department of University of Chile in Santiago (DGF) under the project of Integrated Plate Boundary Observatory Chile (IPOC) (Schurr et al., 2009). Additional data of this earthquake are also available from the strong motion network operated by University of Chile in colaboration with German and Swiss institutions (see Boroschek et al., 2008).

We used the strong motion data from both networks, IPOC and University of Chile networks, to calculate the coseismic static displacements due to Mw 7.7 Tocopilla earthquake. The results of strong motion derived displacements are shown in Figure 4.2. Table 4.1 shows the displacements data. In total, 48 waveforms from 16 stations were analyzed. Eleven closest stations have peak ground acceleration greater than 50 $cm\,s^{-2}$. For these stations we show the results using both methods by Chao et al. (2009) and Iwan et al. (1985). Whereas, for other stations we only show the results by using Chao et al. (2009).

In order to compare the results of displacements obtained from strong motion data with the GPS data, we used the GPS data from Béjar-Pizarro et al. (2010) as the reference. As shown in Figure 4.2, the blue arrows represent the displacements data from GPS stations. Red and green arrows show the strong motion derived displacements using methods by Chao et al. (2009) and Iwan et al. (1985), respectively. Comparing the results of displacements from the two methods, the results using method by Chao et al. (2009) showing the strong motion derived displacements are in good agreement with the GPS measurements, particularly for horizontal components. For the vertical component, in general, both methods either Chao et al. (2009) or Iwan et al. (1985) showing good results which are comparable to the GPS data.

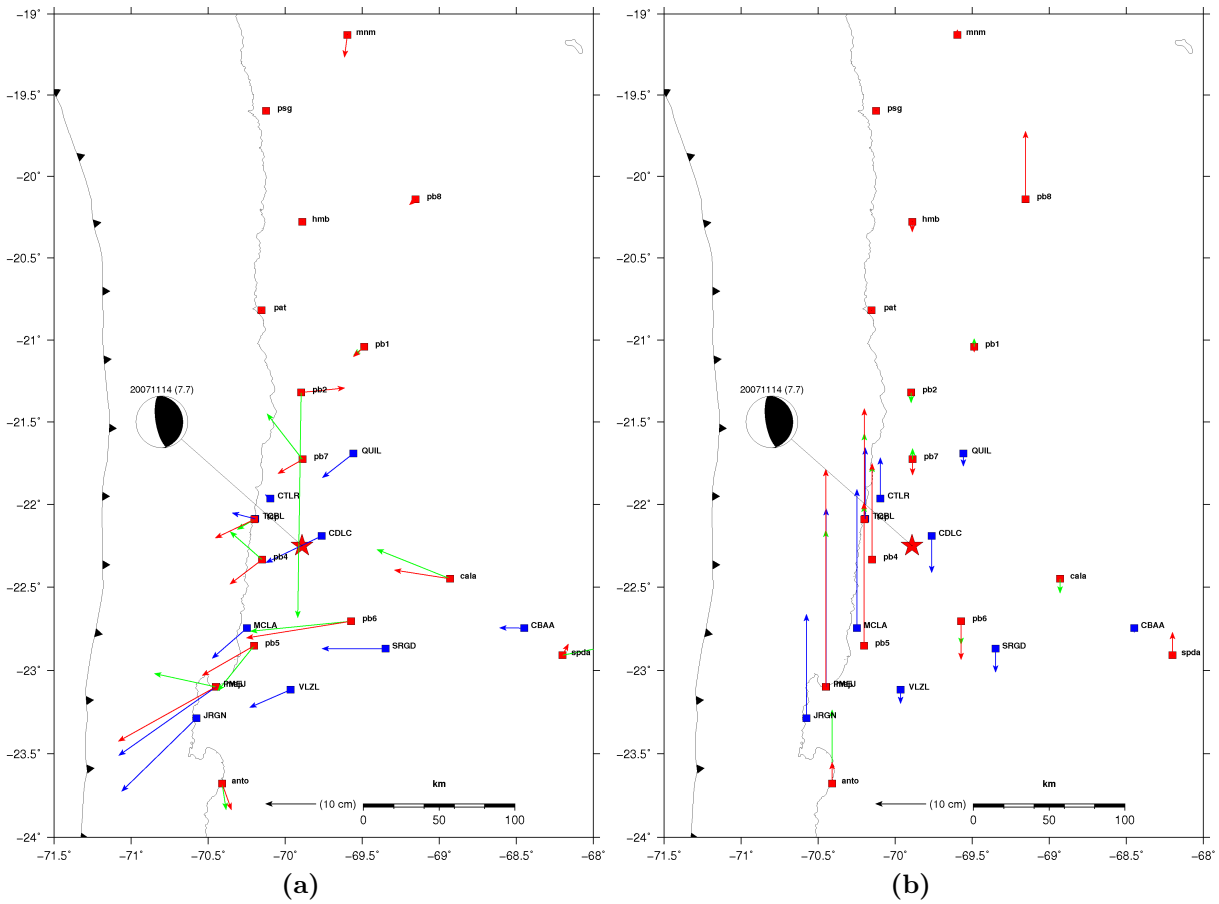

(a) (b)

Figure 4.2: (a) The strong motion derived displacements for horizontal components calculated by Chao et al. (2009) and Iwan et al. (1985) methods, respectively shown by red and green arrows. Blue arrows showing the GPS data from Béjar-Pizarro et al. (2010). Red star and beach-ball show the mainshock location and focal mechanism solution from GCMT. (b) Same as Figure 4.2a but for the vertical component.

Table 4.1: Strong motion derived displacements for Tocopilla earthquake

Sta	Lat(S)	Lon(W)	EW(cm)	NS(cm)	UD(cm)
ANTO	-23.68	-70.41	1.8553	-5.2294	4.2393
CALA	-22.45	-68.93	-11.015	1.7206	0.30204
HMB	-20.278	-69.888	-0.34346	-0.35249	-2.0754
MEJI	-23.1	-70.45	-19.306	-10.772	43.088
MNM	-19.131	-69.596	-0.57734	-4.3966	1.071

Continued on next page

Table 4.1 – continued from previous page

Sta	Lat(S)	Lon(W)	EW(cm)	NS(cm)	UD(cm)
PAT	-20.821	-70.153	-0.045424	-0.17604	-0.1002
PB01	-21.043	-69.487	-2.1838	-1.9945	-1.0855
PB02	-21.32	-69.896	8.6297	0.88738	0.14322
PB04	-22.334	-70.149	-6.3683	-4.8651	19.082
PB05	-22.853	-70.202	-10.291	-5.9124	28.386
PB06	-22.706	-69.572	-20.719	-3.3039	-7.6091
PB07	-21.727	-69.886	-4.8924	-2.8038	-3.0852
PB08	-20.141	-69.153	-1.2004	-1.0833	13.469
PSG	-19.597	-70.123	0.71486	0.21541	-0.68124
SPDA	-22.91	-68.2	1.1903	2.233	4.5847
TCP	-22.09	-70.2	-7.7184	-3.6841	21.97

4.1.3 The 2010, Mw 7.8 Mentawai earthquake

An earthquake with moment magnitude of 7.8 hit west of Mentawai islands, offshore the island of Sumatra on October 25, 2010. The hypocenter was located at 3.48S and 100.11E with the depth was about 20 km. The earthquake has the origin time at 14:42:22 UTC or on the evening at 21:42:22 local time.

At the location of this earthquake, the Australian plate moves north-northeast with respect to the Sunda plate at a relative velocity of approximately 57-69 mm/yr (USGS, *http* : *//earthquake.usgs.gov*). The Mentawai earthquake occurred as a result of thrust faulting. Focal mechanism solution and earthquake depth indicate that this earthquake

occurred at the slab interface between the Australian and Sunda plates (see Singh et al., 2011).

The earthquake generated a surprisingly large tsunami with maximum runup height is larger than 16 meters (Hill et al., 2012). It caused at least 509 people killed and substantial damage (Pusdalops PB Sumatra Barat). Mentawai earthquake is classified as the "tsunami earthquake" based on its definition that the "tsunami earthquake" is reserved for a special earthquake events that generate tsunamis much larger than expected for their magnitude (Kanamori, 1972).

The Mentawai earthquake and the structure of Mentawai segment have been studied by e.g. Lay et al. (2011); Newman et al. (2011); Singh et al. (2011); Collings et al. (2012) and Hill et al. (2012). Lay et al. (2011) and Newman et al. (2011) show the rupture model of the earthquake based on teleseismic inversion. Newman et al. (2011) also identified the earthquake as a "tsunami earthquake". Singh et al. (2011) and Collings et al. (2012) image the structure of Mentawai segment, respectively using seismic reflection data and local earthquake traveltime tomography. Hill et al. (2012) proposed the rupture model based on near-field GPS data inversion. From the Mentawai earthquake, we learnt the potential of significant tsunami generation due to shallow megathrust ruptures in regions of up-dip of great underthrusting earthquakes and therefore we should aware for the tsunami hazard not only due to great earthquake in strongly coupled portions subduction zone but also in weakly shallow regions.

In this study, we used different data to investigate coseismic deformations caused by Mentawai earthquake. We calculated surface static displacements using strong motion records. The earthquake was recorded by the strong motion network of BMKG (Meteorological, Climatological and Geophysical Agency of Indonesia). For this data set, we applied the method of baseline correction proposed by Chao et al. (2009) to calculate the

static displacements from strong motion data. The method proposed by Iwan et al. (1985) was not applied to the data set because it does not meet the requirement of thresholds. We compared the results of strong motion derived displacements with the GPS data from Sumatra GPS Array (SuGAr) network, which were analyzed by Hill et al. (2012).

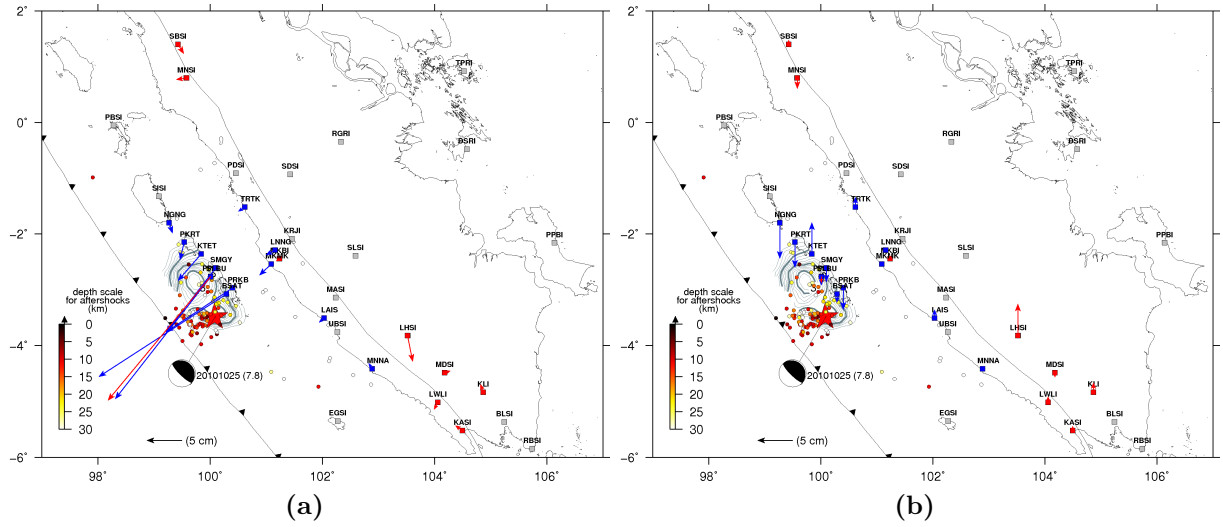

Figure 4.3: (a) Strong motion derived displacements for the horizontal components calculated by Chao et al. (2009) method, shown by red arrows. Blue arrows showing the GPS data from Hill et al. (2012). Color scaled circles indicate the aftershocks until March 25, 2011 from GEOFON network. Contour lines represent the slip distribution from Lay et al. (2011). Red star and beach-ball show the mainshock location and focal mechanism solution from GCMT. (b) Same as Figure 4.3a but for the vertical component.

Figure 4.3 and Table 4.2 show the results of static displacements calculated from strong motion records of the 2010, Mw 7.8 Mentawai earthquake, Sumatra. Only two stations located relatively close to epicenter location of the earthquake. Red arrows showing the displacements calculated from strong motion data. Blue arrows represent the GPS data obtained from Hill et al. (2012). The significant displacement was recorded at station PPSI (2.76S,100.01E), which is almost collocated with the GPS station SLBU (-2.77S,100.01E) of SuGAr network. The strong motion derived displacements at station PPSI were -14.65 cm, -17.66 cm and -0.89 cm, respectively for east-west, north-south and vertical components. The GPS data at station SLBU showing the displacements of -13.6 cm,

-17.4 cm and -1.2 cm, respectively for east-west, north-south and vertical components. For additional references, we also show the slip distribution from Lay et al. (2011) and aftershock distribution from GEOFON network.

Table 4.2: Strong motion derived displacements for Mentawai earthquake

Sta	**Lat(S)**	**Lon(E)**	**EW(cm)**	**NS(cm)**	**UD(cm)**
KASI	-5.5236	104.5	-0.99788	0.72348	0.61687
KLI	-4.8363	104.87	-0.39208	1.1384	1.3595
LHSI	-3.8266	103.52	0.73885	-3.6795	4.5355
LWLI	-5.0175	104.06	-0.52836	-0.9928	0.8012
MDSI	-4.486	104.18	0.82407	0.26508	-0.65255
MKBI	-2.4474	101.24	-0.48129	-0.33613	0.46877
MNSI	0.7955	99.58	-1.4657	-0.22198	-1.5185
PPSI	-2.766	100.01	-14.645	-17.663	-0.89438
SBSI	1.3988	99.431	0.84231	-1.3358	0.61426

4.1.4 The 2011, Mw 9.0 Tohoku earthquake

The Tohoku earthquake, with a moment magnitude of 9.0 was the fourth greatest earthquake in the world since 1900 as compiled by USGS. Previous historical Mw 9-class earthquakes were the 1960, Mw 9.5 Chile, the 1964, Mw 9.2 Alaska and the 2004, Mw 9.1 Sumatra earthquakes. Tohoku earthquake occurred on March 11, 2011 at the origin time 05:46:24 UTC. The epicenter was located at 38.297N and 142.372E with the hypocenter depth was about 30 km.

The earthquake was the result of thrust faulting at subduction zone plate boundary

between the Pasific and North American plates. The North American plate subducts beneath the Pasific plate with the relative velocity of plate motion 83 mm/yr. The focal mechanism solution and depth of the hypocenter location consistent with the event having occurred at the slab interface.

The Tohoku earthquake generated a huge tsunami with a maximum runup height of about 37.88 m (USGS). It caused at least 15,863 people killed, 4,414 missing, 5,901 injured and 114,591 house collapses as of August 25, 2011 (Fire Disaster Management Agency of Japan, 2011).

From all the largest historical Mw 9-class earthquakes mentioned before, the Tohoku earthquake was observed by the densest networks of geophysical and geodetic instruments. The earthquake was recorded by 84 F-Net broadband sensors, 1,000 K-Net strong motion accelerometers, 777 Hi-Net high sensitivity seismographic stations (boreholes installation), 777 KiK-Net strong motion accelerometers (surface and boreholes installation), which are collocated with the Hi-Net stations and 1,200 permanent GPS stations of GEONET, Japan. These data provide a unique opportunity to investigate the consistency of the ground motion and source mechanism observed by different instruments.

In this study, we analyzed strong motion records from KiK-Net boreholes stations. The KiK-Net boreholes strong motion data are the most stable data compared to other strong motion data from K-Net or KiK-Net surface installation. KiK-Net boreholes sensors installed on the hard rock at the depth from the surface between 100 and 2000 meters. We used the data to recover coseismic deformations due to the Tohoku earthquake. We applied two methods of baseline correction proposed by Chao et al. (2009) and Iwan et al. (1985).

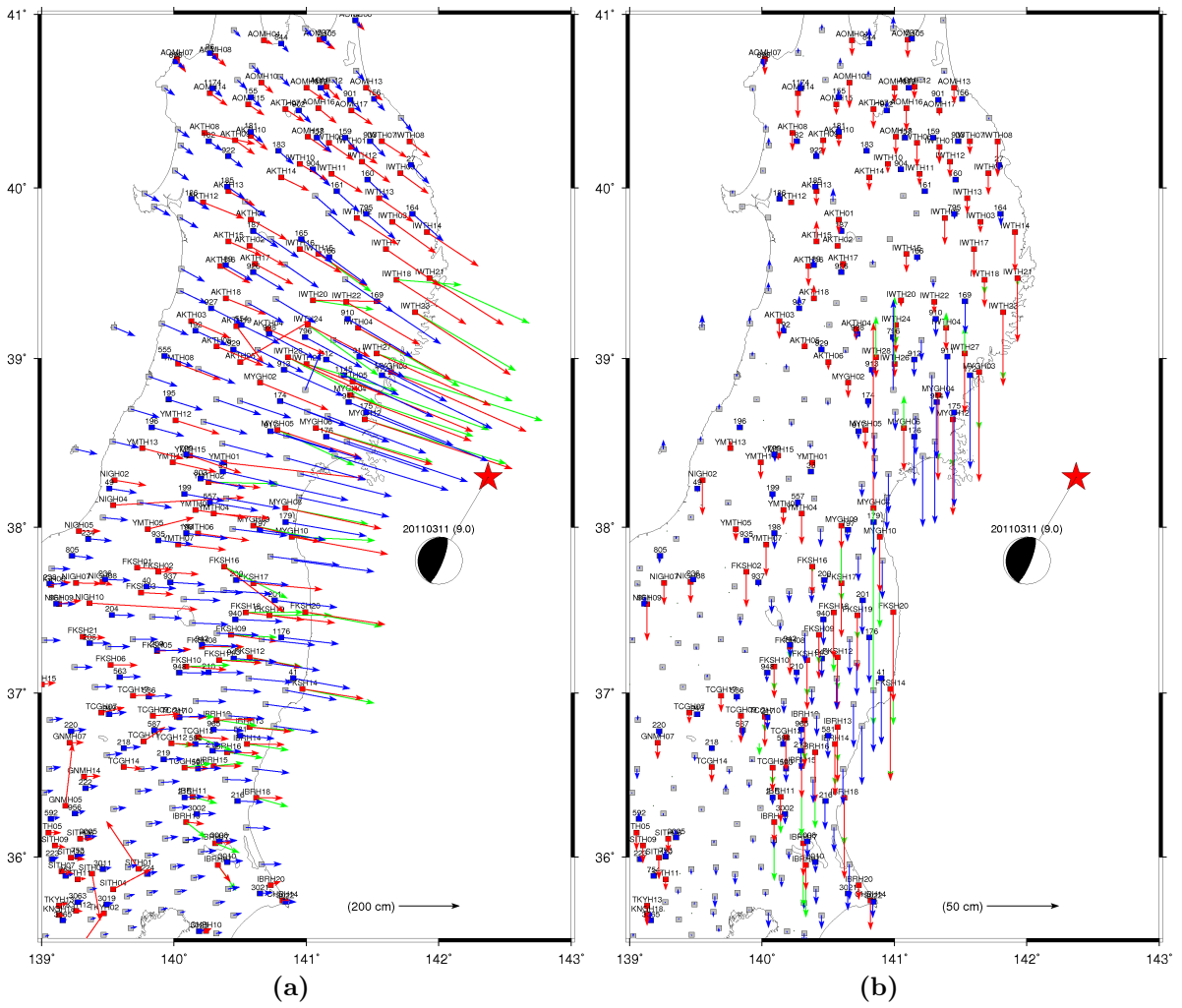

Figure 4.4: (a) Comparison of the static displacements calculated from strong motion data using methods by Chao et al. (2009), Iwan et al. (1985) and displacements from GPS measurements with different vector colors of red, green and blue, respectively. Red star and beach-ball show the epicenter location and focal mechanism solution from GCMT. Small red, blue and gray squares, respectively represent strong motion seismic stations, nearby GPS stations used for the references and unused GPS stations. (b) Same as Figure 4.4a but for the vertical component.

Figures 4.4 shows the results of static displacements calculated using methods by Chao et al. (2009) and Iwan et al. (1985). For reference, we show the displacements obtained from GPS measurements released by the ARIA team at JPL and Caltech. There are 44 stations used to calculate the static displacements using Iwan et al (1985) method since those stations meet the threshold requirement of the method that the PGA is larger than

50 $cm\ s^{-2}$. Using the method by Chao et al. (2009), we calculated the static displacements of 143 stations within the coordinates 35.5N to 41N and 139E to 143E. Compared to the results of strong motion derived displacements using the method by Iwan et al. (1985), the results using method by Chao et al. (2009), in general, show more comparable to the GPS measurements.

Tohoku earthquake has the very large rupture length and width. The earthquake caused the surface static deformations in a very large area. The nearest station to epicenter location of the earthquake was MYGH12, located at 38.642N and 141.44E. The static displacements at this station were calculated with the amplitudes of 400 cm, -150 cm and -69 cm, respectively for east-west, north-south and vertical components. A nearby GPS station "0175", is located at a distance of 4.62 km from MYGH12 seismic station. The displacements were measured at this station with the amplitudes of 404 cm, -161 cm and -66 cm, respectively for east-west, north-south and vertical components. On the other hand, at station TKYH13, for example, which is located at 35.702N and 139.13E at a distance of ∼408 km from epicenter location, the static displacements were calculated from strong motion data with the amplitudes of 25 cm, 16 cm and -6 cm, respectively for east-west, north-south and vertical components. These examples of static deformations data illustrated how large the static deformations were, due to the Tohoku earthquake.

4.2 T1 and T3 variation for the Tohoku earthquake data set

Results of strong motion derived displacements for the four data sets in Section 4.1 confirmed that the method by Chao et al. (2009) gives better solutions, either for horizontal or vertical components. Further study, the very large and very good quality of boreholes strong motion data of Tohoku earthquake give us opportunity to evaluate the method proposed by Chao et al. (2009) deeply. We applied similar method described by Wu & Wu (2007) and Chao et al. (2009) to find the best variation of T1 and T3 positions for the Tohoku earthquake data set. Determination of T1 and T3 positions were optimized, so that the final strong motion derived displacement best fits the nearby GPS data. Compared to Chao et al. (2009) method, the difference we made in our study, is that we distinguished our data processing for horizontal and vertical components. It was considered based on the assumption about the different effect of tilt for horizontal and vertical components that was proposed by Rodgers (1968); Boore (2001); Graizer (2005, 2006, 2010). They noted that the ground tilt and rotation during the strong shaking is the source of baseline shift. Boore (1999); Clinton (2004) and Graizer (2006) indicated that the tilt effect for the vertical component is less sensitive compared to horizontal components.

Figures 4.5a and 4.5b below showing the results of T1 and T3 determinations for the Tohoku earthquake data set for horizontal and vertical components, respectively. We used 650 waveforms for horizontal components, whereas for the vertical component was 325 waveforms. A grid search method was used to find the best position of time points T1 and T3 in each waveform and calculated the average of all data. The minimum misfit of strong motion derived displacements and nearby GPS data for horizontal components is reached with the variation of T1 at 4% and T3 at 87% of cumulative energy. For the

vertical component, the best variation of T1 and T3 is respectively at 24% and 51% of the cumulative energy.

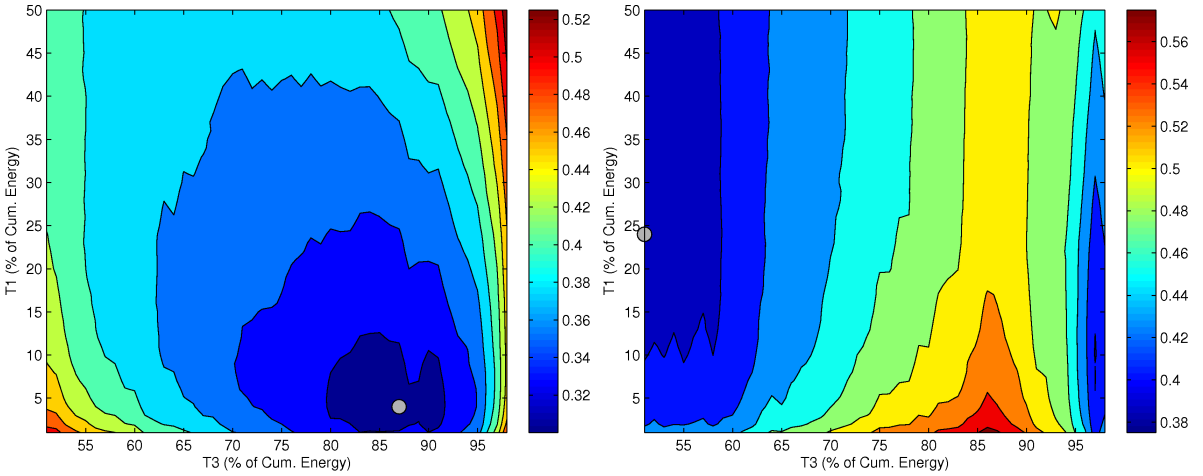

Figure 4.5: (a) Misfit contour of strong motion derived displacements and nearby GPS data for the Tohoku earthquake data set for horizontal components. The minimum misfit is reached at the variation of T1 and T3, respectively at 4% and 87% of cumulative energy. The position of minimum misfit is indicated by gray circle. (b) Same as Figure 4.5a but for the vertical component. The minimum misfit is reached at 24% and 51% of cumulative energy for T1 and T3, respectively.

We used the variation of T1 and T3 positions obtained from Figure 4.5 above in the baseline correction procedure proposed by Wu & Wu (2007). We calculated static displacements from strong motion data set of the Tohoku earthquake. Figures 4.6b and 4.8b show the results of static displacements calculated using T1 and T3 variation proposed in this study for horizontal and vertical components. The figures also show color contour of vector length deviations of strong motion derived displacements and nearby GPS data. Figures 4.7a and 4.7b show the deviations of azimuth or displacements direction using method of Chao et al. (2009) and improvement method in this study. The average values of deviation are shown in Table 4.3.

Table 4.3: Comparison of deviations between strong motion derived displacements and nearby GPS data, using T1 and T3 in this study and Chao et al. (2009) method.

	Deviation	
	Chao et al (2009) **T1:25%,T3:65%**	**This study** **(Hor) T1:4%,T3:87%** **(Ver) T1:24%,T3:51%**
Horizontal (%)	54.1	39.7
Azimuth (*deg*)	11.3	9.4
Vertical (%)	301.7	212.1

These results show clearly that the deviations between strong motion derived displacements and nearby GPS data are significantly reduced using T1 and T3 variation in this study. For horizontal components, the deviation is reduced from 54.1% to 39.7%. The consistency of the improvements are also shown at deviations of azimuth and vertical component. However, as shown in the results by using the method of Chao et al. (2009) where T1 and T3 variation is at 25% and 65% of cumulative energy ratio, the average deviation for the vertical component is very large. Eventhough the average deviation is significantly minimized using T1 and T3 variation in this study, the average deviation of vertical component is still large. The strong motion derived displacements of vertical component are less comparable to GPS data.

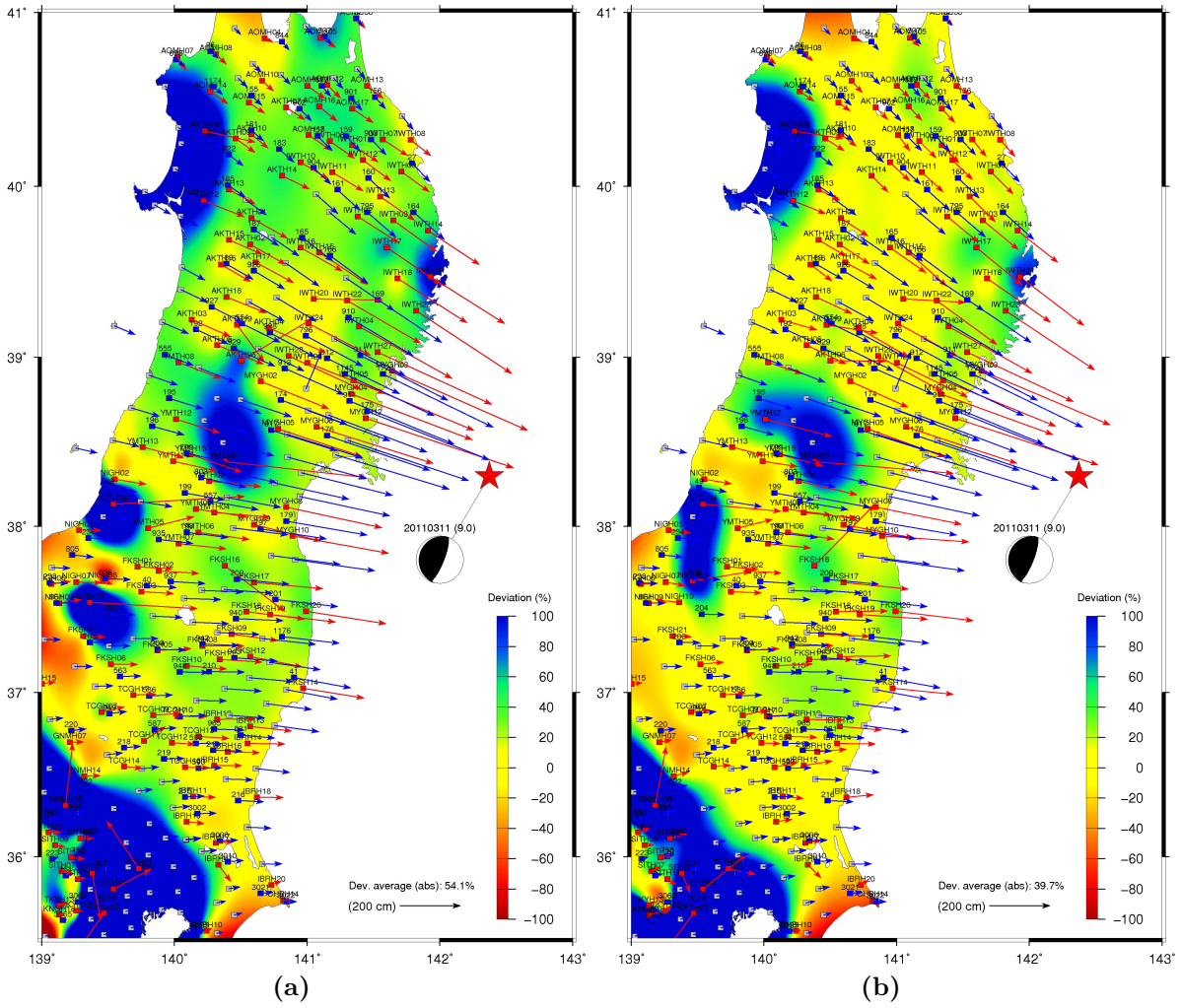

Figure 4.6: (a) Results of strong motion derived displacements calculated using Chao et al. (2009) method with color contour of deviations of vector length relative to GPS measurements. Red and blue arrows show the displacements obtained from strong motion records and GPS measurements, respectively. (b) Same as Figure 4.6a but the displacements were calculated using T1 and T3 variation at 4% and 87% of cumulative energy ratio, respectively.

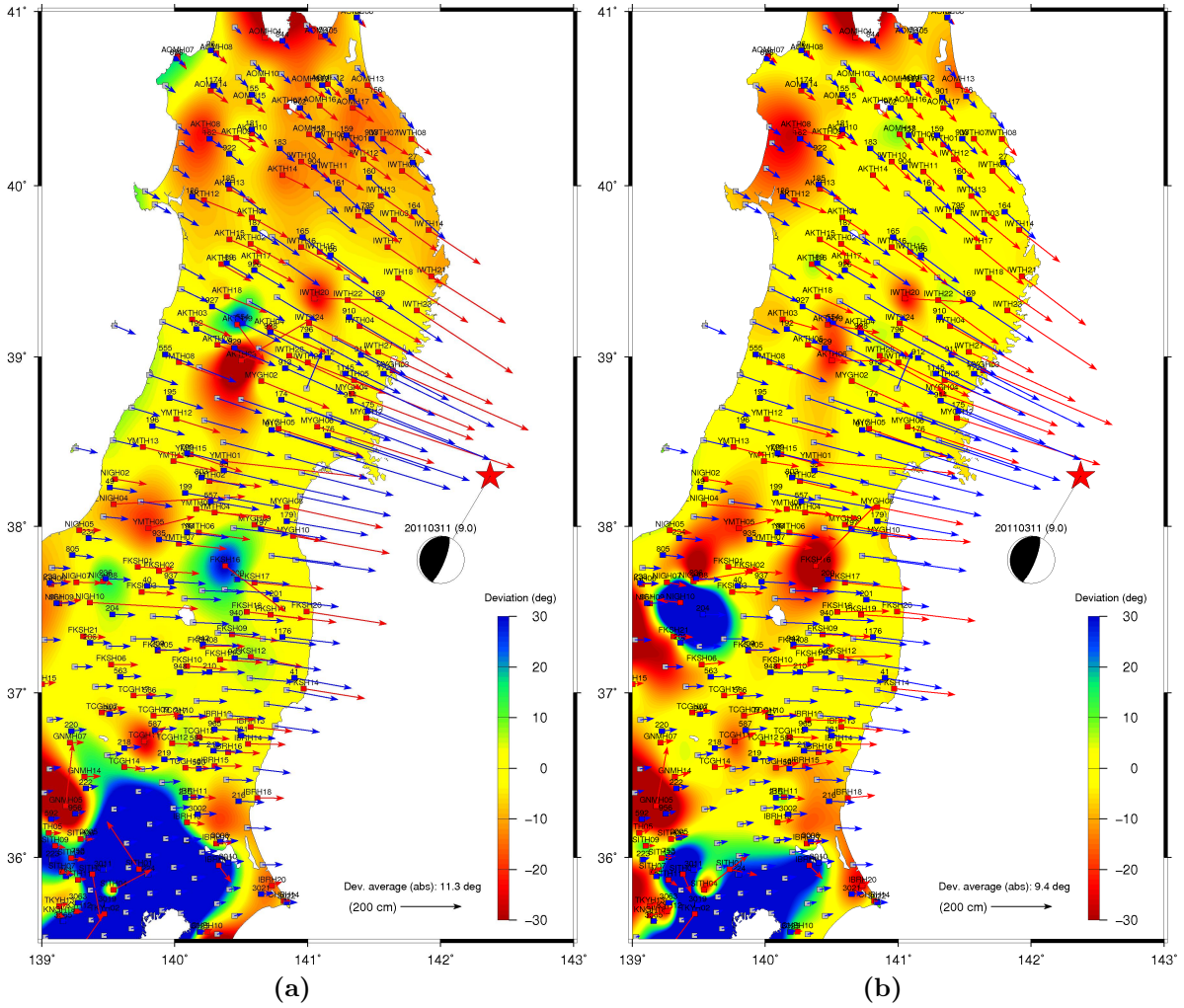

Figure 4.7: (a) The azimuth deviations of strong motion derived displacements relative to nearby GPS measurements. The strong motion derived displacements were calculated using Chao et al. (2009) method. (b) Same as Figure 4.7a but the displacements were calculated using T1 and T3 variation at 4% and 87% of cumulative energy, respectively.

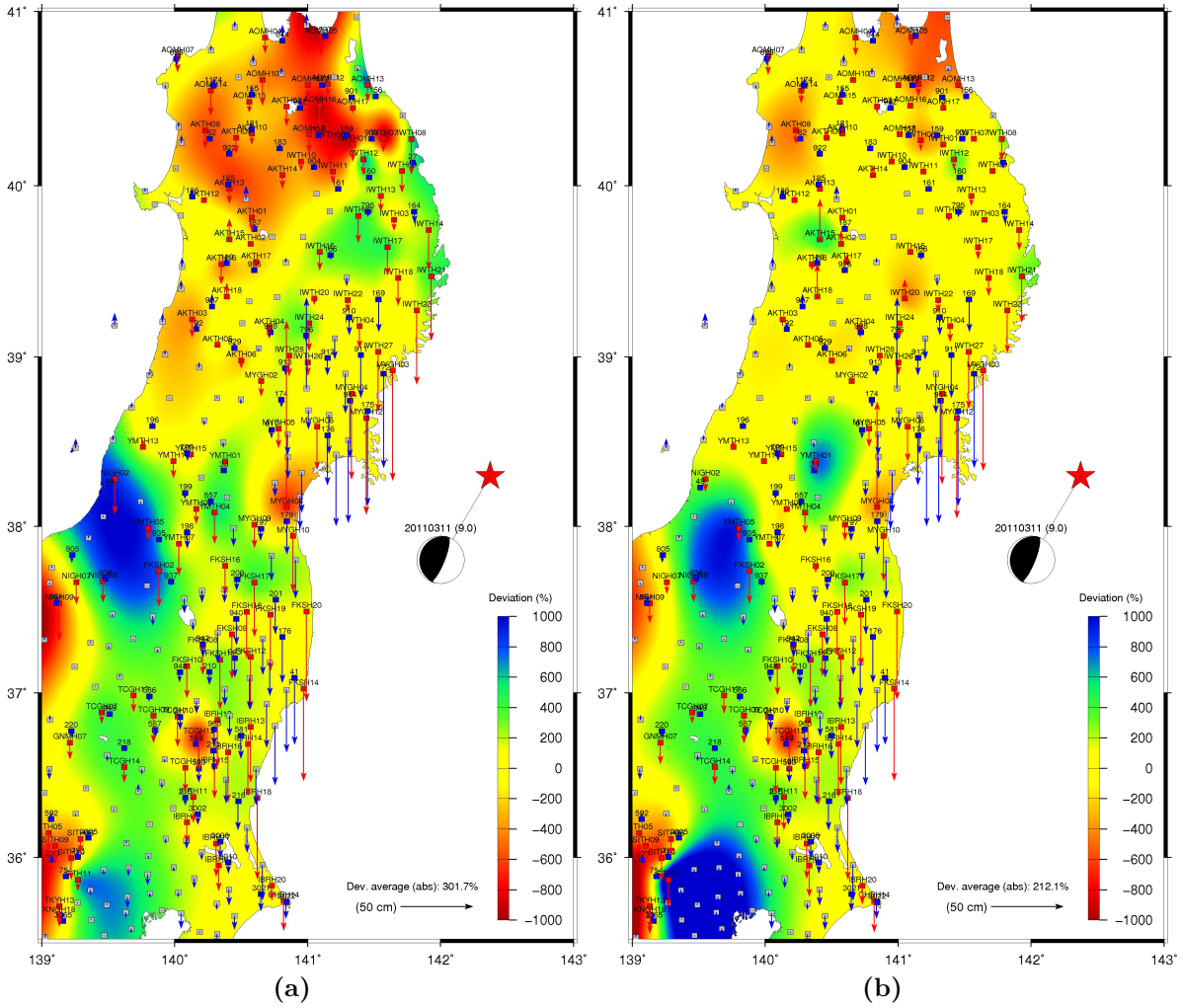

Figure 4.8: (a) The deviations of strong motion derived displacements relative to nearby GPS measurements for the vertical component. The strong motion derived displacements were calculated using Chao et al. (2009) method. (b) Same as Figure 4.8a but the displacements were calculated using T1 and T3 variation at 24% and 51% of cumulative energy, respectively.

4.3 The hypocenter distance dependency of the empirical baseline correction

Further study, we investigated the dependency of method to hypocenter distance. We applied similar method as it has been done in Section 4.2 for different groups of data with different distances. The distance of each group of data increased from 100 to 650 km with the intervals of 25 km. For every group of data we applied a grid search method to determine the best position of T1 and T3. It was indicated by the results of strong motion derived displacements which have the minimum misfit to nearby GPS data. We then calculated the average of minimum misfit for each group of data. We made relation between time points T1 and T3 positions as functions of hypocenter distance.

Figures 4.9a and 4.9b show the relation of T1 and T3 as functions of hypocenter distance for horizontal and vertical displacements. The numbers below gray squares show number of waveforms data used for the correspondence intervals. Total number of data used for the horizontal components were 650 waveforms and for the vertical component was 325 waveforms.

Figure 4.9a (Top) shows a linear relation of T3 as a function of hypocenter distance for the horizontal components obtained from the average of results of east-west and north-south components. The relation follows a linear equation as given by the Eq. 4.1. T3 is in percentage of cumulative energy ratio and the hypocenter distance is in kilometers. In Figure 4.9a (Buttom), we found an exponential relation of T1 as a function of hypocenter distance. The relation follows Eq. 4.2. The thin dashed line in both Figures 4.9a buttom and top show the position of T1 at 25% and T3 at 65% of cumulative energy proposed by Chao et al. (2009).

$$T3 = 102.78 - 0.052332 * distance, (110 < dist. < 650km) \tag{4.1}$$

$$T1 = 143.92 * exp(-0.0087366 * distance), (110 < dist. < 650km) \tag{4.2}$$

Similar to Figure 4.9a, Figure 4.9b shows the relation of T1 and T3 as functions of hypocenter distance for the vertical component. T3 jumps dramatically from near 50% to near 100% at the hypocenter distance of about 300 km. The equations for both linear relations before and after 300 km follow Eqs. 4.3 and 4.4, respectively. The number of data used for the vertical component was 325 waveforms. A combination of linear and exponential relations is shown at relation of T1 as a function of distance for the vertical component in Figure 4.9b buttom. The relations follow Eqs. 4.5 and 4.6 respectively for the hypocenter distance less than 300 km and greater than 300 km.

$$T3 = 53.964 - distance * 0.0057143, (110 < dist. < 300km) \tag{4.3}$$

$$T3 = 99.576 - 0.0058024 * distance, (300 < dist. < 650km) \tag{4.4}$$

$$T1 = 0.21108 * distance - 27.189, (110 < dist. < 300km) \tag{4.5}$$

$$T1 = 12652 * exp(-0.019569 * distance), (300 < dist. < 650km) \tag{4.6}$$

Figures 4.10a and 4.10b, respectively show the results of static displacements for horizontal components calculated using method of Chao et al. (2009) and improvement method in this study. In general, they are comparable with the GPS data. We found that, using Chao et al. (2009) method the strong motion derived displacements are larger than the GPS measurements from the average of absolute deviation for horizontal components (see Figure 4.10a). The average of absolute deviation is about 54.1%. On the other hand,

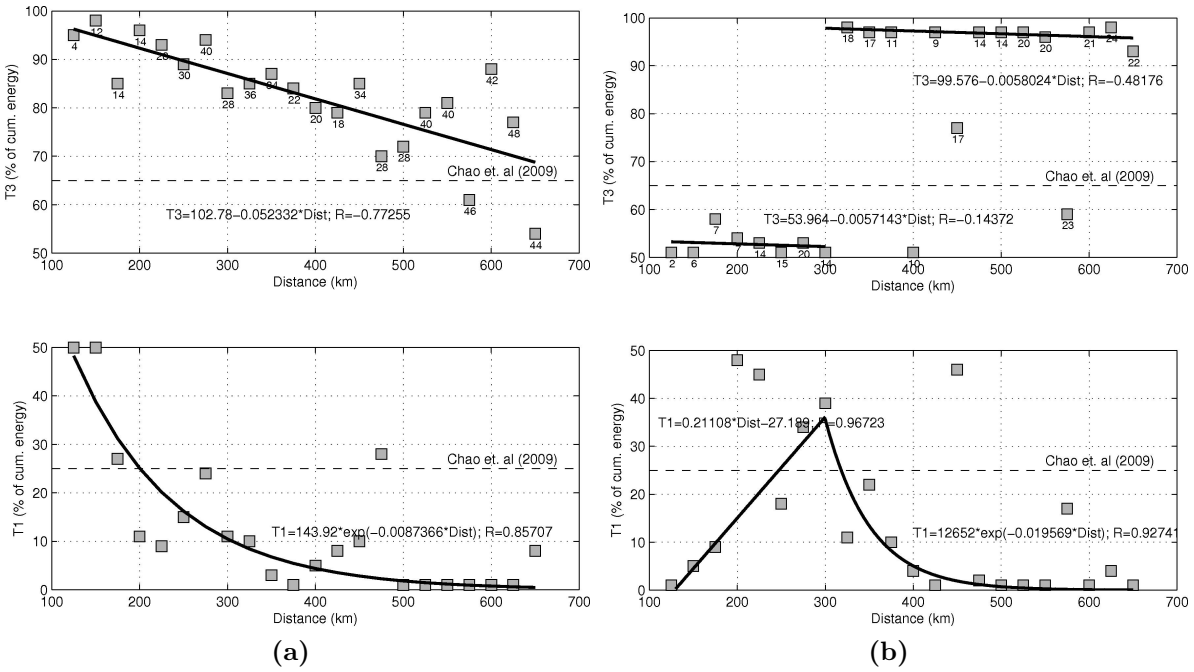

Figure 4.9: (a) Relation between ratio of cumulative energy of T3 and T1 as functions of hypocenter distance. Gray squares show the position of T3 and T1 which have the minimum misfit between strong motion derived displacements and nearby GPS measurements at the correspondence distance. Solid lines show linear and exponential line fitting for T3 and T1. Thin dash lines show the position of T3 and T1 proposed by Chao et al. (2009). (b) Same as Figure 4.9a but for the vertical component.

Figure 4.10b show the results using improvement method in this study. The average of absolute deviation is about 35.2% larger relative to the GPS measurement.

The deviations of azimuth or displacement directions are shown in Figures 4.11a and 4.11b. Figure 4.11a shows the results by using Chao et al. (2009) method with the average of absolute deviation is about 11.3 degrees relative to the direction of displacements from GPS measurements. Degrees in minus mean anti clockwise direction of deviation. Figure 4.11b shows the results using improvement method in this study. The average of absolute deviations is about 8.0 degrees.

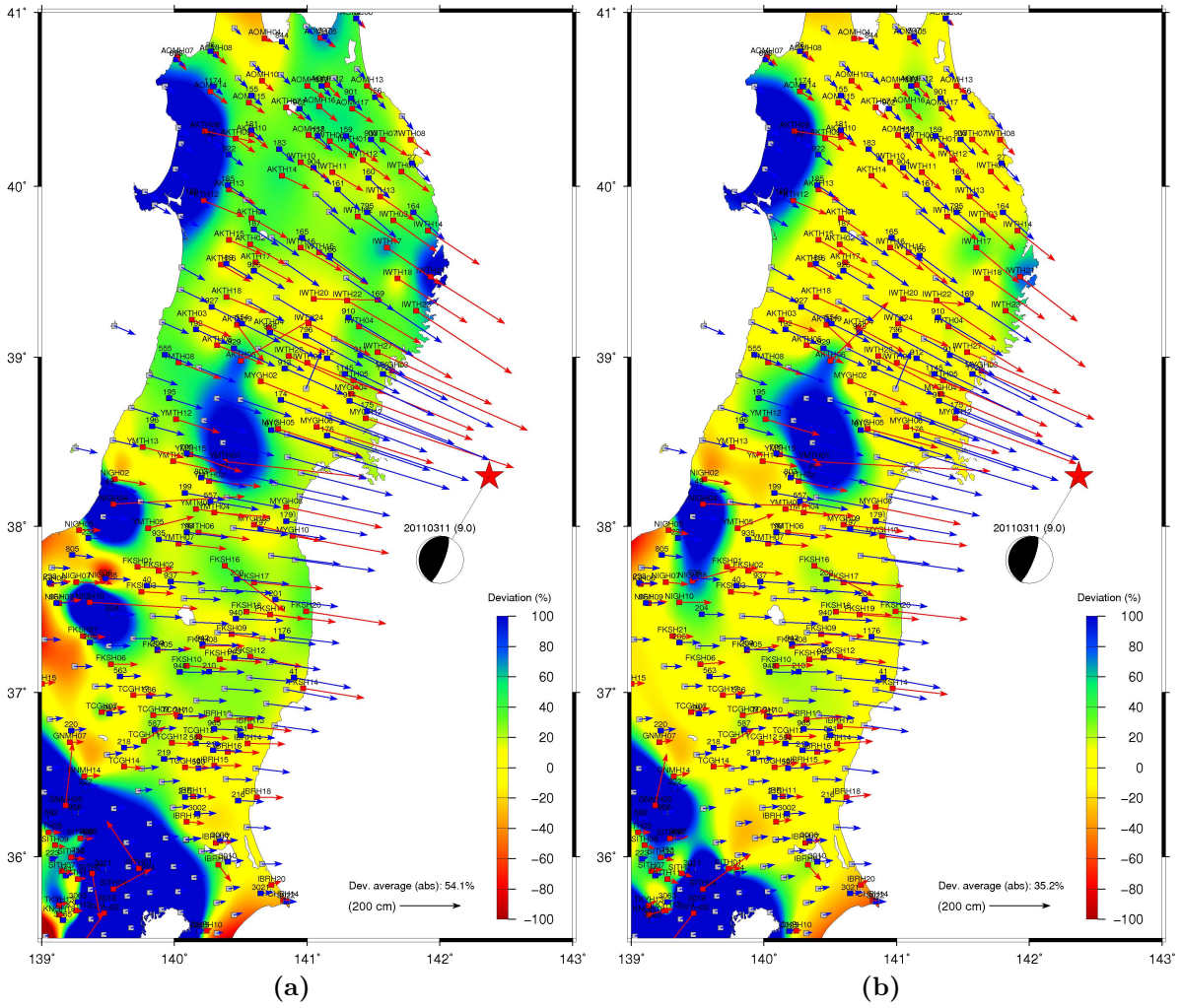

Figure 4.10: (a) Results of strong motion derived displacements calculated using Chao et al. (2009) method with color contour of deviations of vector length relative to GPS measurements. Red and blue arrows show the displacements obtained from strong motion records and GPS measurements, respectively. (b) Same as Figure 4.10a but the displacements were calculated using the improvement method in this study.

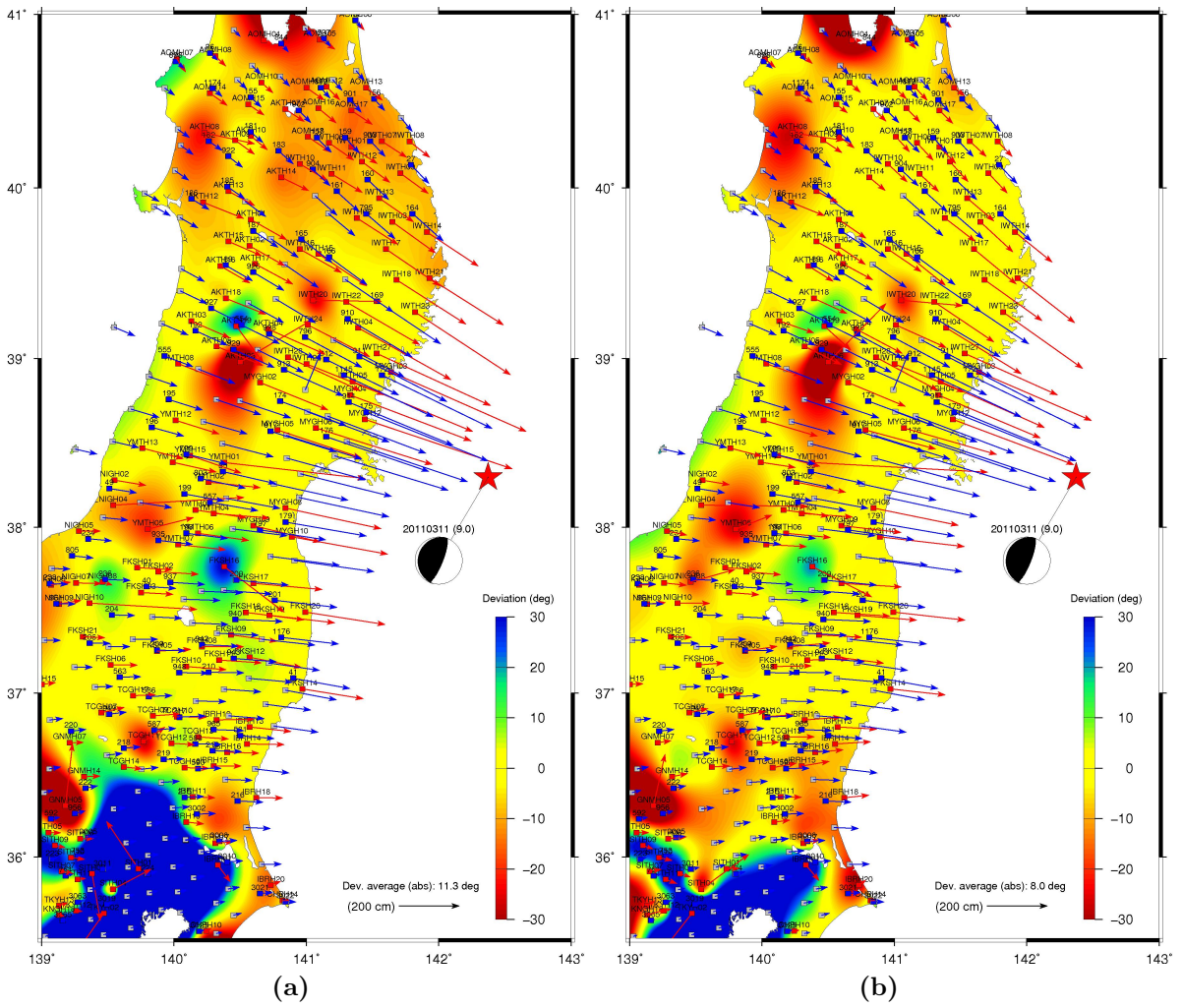

(a) **(b)**

Figure 4.11: (a) Azimuth deviations of strong motion derived displacements relative to nearby GPS measurements. The strong motion derived displacements were calculated using Chao et al. (2009) method. (b) Same as Figure 4.11a but the displacements were calculated using the improvement method in this study.

For the vertical displacements as shown in Figures 4.12a and 4.12b, the deviations are relatively very large. Using Chao et al. (2009) method as shown in Figure 4.12a, we obtain the average of absolute deviations about 301.7% relative to GPS measurements. Most of large deviations, which increased the average values, were contributed by relatively far-field data. A much better results using the improvement method in this study shown in Figure 4.12b. The average of absolute deviation is about 193.0% relative to GPS measurements.

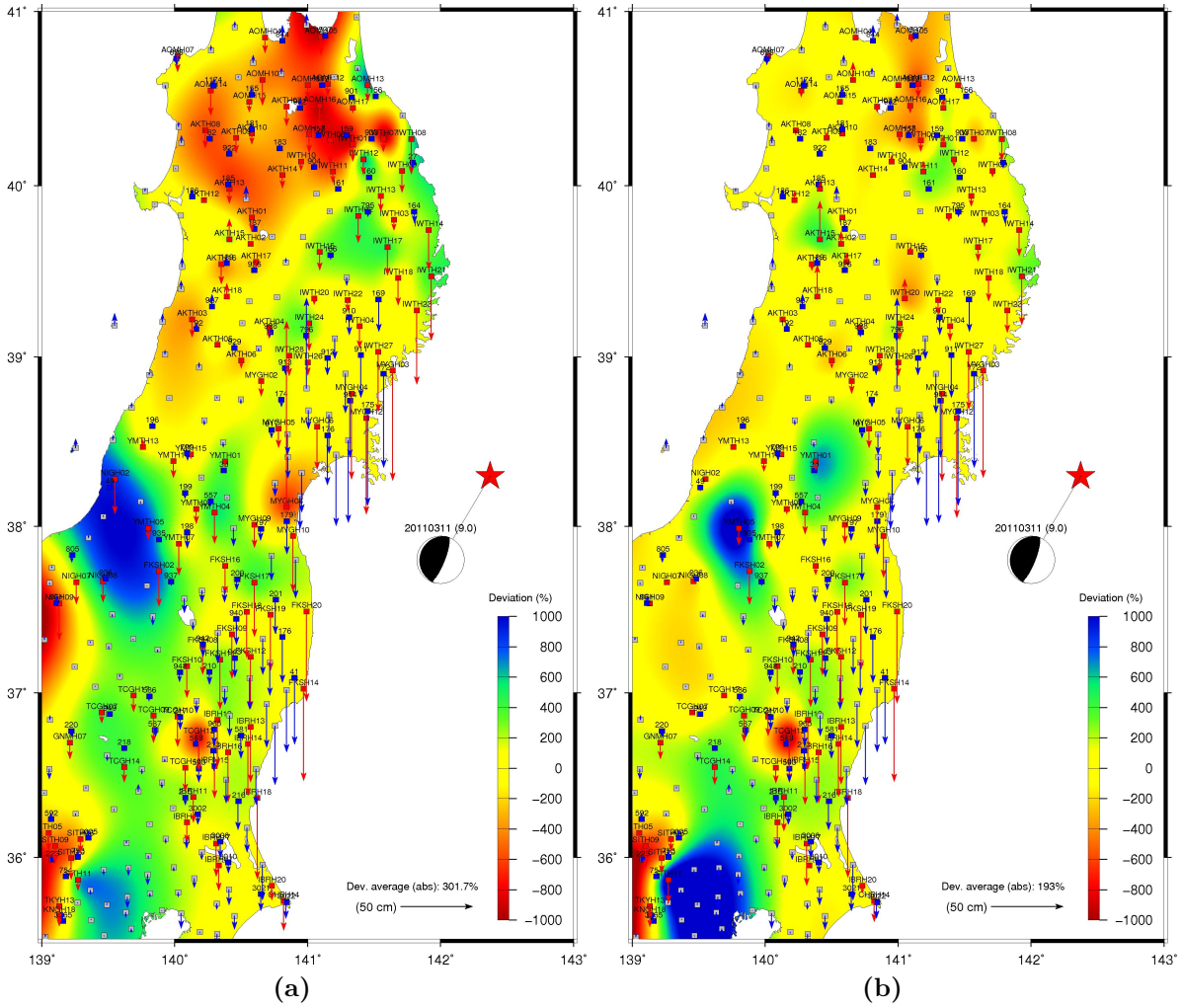

Figure 4.12: (a) The deviations of strong motion derived displacements relative to nearby GPS measurements for the vertical component. The strong motion derived displacements were calculated using Chao et al. (2009) method. (b) Same as Figure 4.12a but the displacements were calculated using the improvement method in this study.

Table 4.4: Comparison of displacement deviations using T1 and T3 as functions of hypocenter distance and Chao et al. (2009) method

	Deviation	
	Chao et al (2009)	**This study**
	T1:25%,T3:65%	**T1(dist),T3(dist)**
Horizontal (%)	54.1	35.2
Azimuth (*deg*)	11.3	8.0
Vertical (%)	301.7	193.0

4.4 Rapid estimation of coseismic static displacement

Static surface deformation data is very valuable to be used in studies of the source mechanisms of great earthquakes. For instance, inversion of surface deformation data can help to estimate moment magnitude of the earthquake, which is a crucial information for making tsunami warning decision. Inversion of such data can also bring out the slip distribution of the earthquake at the fault interface. For earthquakes occur in subduction zones, slip models give an important information whether the earthquake has the potential for generating a tsunami. Sobolev et al. (2007) reported that the earthquake-induced tsunami is sensitive to slip distribution on the fault interface.

Near-source surface deformations can be measured using satellite-based methods (i.e. GPS and InSAR) and seismic method. Using satellite-based methods, however take time hours, days or even longer to get a precise deformation data. This is because the geodetic method (e.g. GPS) requires entire day or multiple days of data at one station to calculate its precise average position before and after the earthquake occurrence (Emore & Haase,

2007). Only continuous high-rate GPS may have the potential to serve the real-time surface deformation data. Accurate GPS real-time processing, however, is not yet well established, and high-rate continuous GPS stations are still rare (Wang et al., 2011). Seismic method, on the other hand, with their several orders of magnitude higher dynamic range can be the solution for recording near-source surface deformation through strong motion accelerometer stations. Once the baseline problem of the acceleration records can be removed properly, we can obtain the static displacements easily and very quickly by simple double integration.

Automatic baseline correction methods have been introduced by e.g. Chao et al. (2009) and Wang et al. (2011). Both techniques can provide the reasonable static displacements due to the earthquake after the records comprise 100% of the earthquake's energy. We analyzed the displacements time series obtained from several strong motion records due to the Tohoku earthquake. We found that the static displacements can already reach a near-stable position soon after the strong shaking transient. This indicates the static displacements can be obtained earlier, instead of waiting for it's complete energy envelope to have ended.

We investigated the method of baseline correction proposed by Chao et al. (2009). We analyzed the arrival time of empirical time points T1 and T3 related to cumulative energy distribution of each accelerogram recorded. Then, we made the relation of arrival time of empirical time points T1 and T3 af functions of hypocenter distance, rather than cumulative energy ratio. In this method, we relied on the assumption that the hypocenter was a point source and available at a very early stage after origin time, usually within few minutes. This method can speed up the calculation of static displacements significantly.

Figure 4.13 shows the relation between arrival time (from P-wave onset) of T1 and T3 as functions of hypocenter distance. The arrival time of T1 and T3 based on the ratio of cumulative energy at 25% and 65% proposed by Chao et al. (2009). The relation follows

the Eqs. 4.7 and 4.8. T1 and T3 are in unit of seconds.

$$T1 = 25.051 + 0.16068 * distance \tag{4.7}$$

$$T3 = 65.916 + 0.16095 * distance \tag{4.8}$$

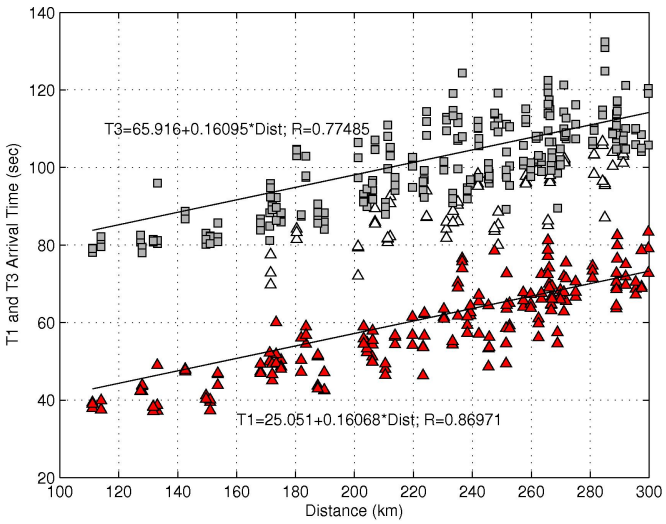

Figure 4.13: Empirical arrival time of T1 and T3 as functions of hypocenter distance. Gray squares represent T3 position and Red triangles represent T1 position. White triangles indicate outliers data.

The equations were derived by using data within a distance of 300 km from the hypocenter location. We collected 255 waveforms from 85 three component stations. Using such empirical equations, which is independent from the ratio of cumulative energy, T1 and T3 can be calculated very quickly. We only need the hypocenter location. Once T1 and T3 are obtained, using Eqs. 4.7 and 4.8, we applied the flatness-based method described by Wu & Wu (2007) to calculate the static displacements.

Figures 4.14a and 4.14b show the comparison between the results of displacements calculated by Chao et al. (2009) and this study, for the horizontal components. For the vertical component, the results are shown in Figures 4.15a and 4.15b. In general, compared to GPS measurements, the results of using Chao et al. (2009) method look better than

this study. Nevetheless, the results in this study, on the other hand, potentially to be calculated much faster than using method by Chao et al. (2009).

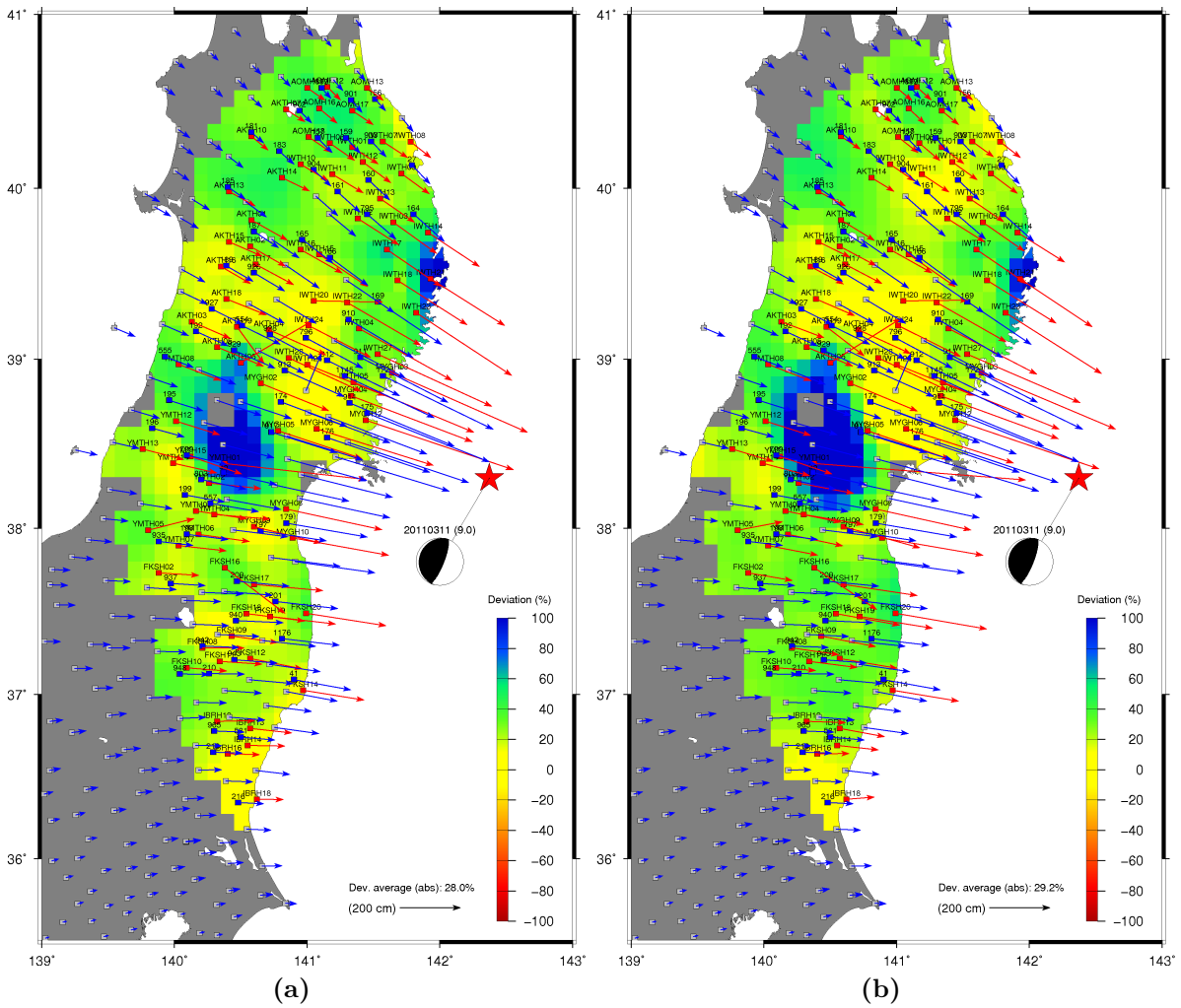

Figure 4.14: Results for horizontal components using different methods. (a) The strong motion derived displacements were calculated using Chao et al. (2009) method. Color contours represent the deviation of vector length between the strong motion derived displacements and GPS measurements. (b) Same as Figure 4.14a but the displacements were calculated using proposed Eqs. 4.7 and 4.8 in this study.

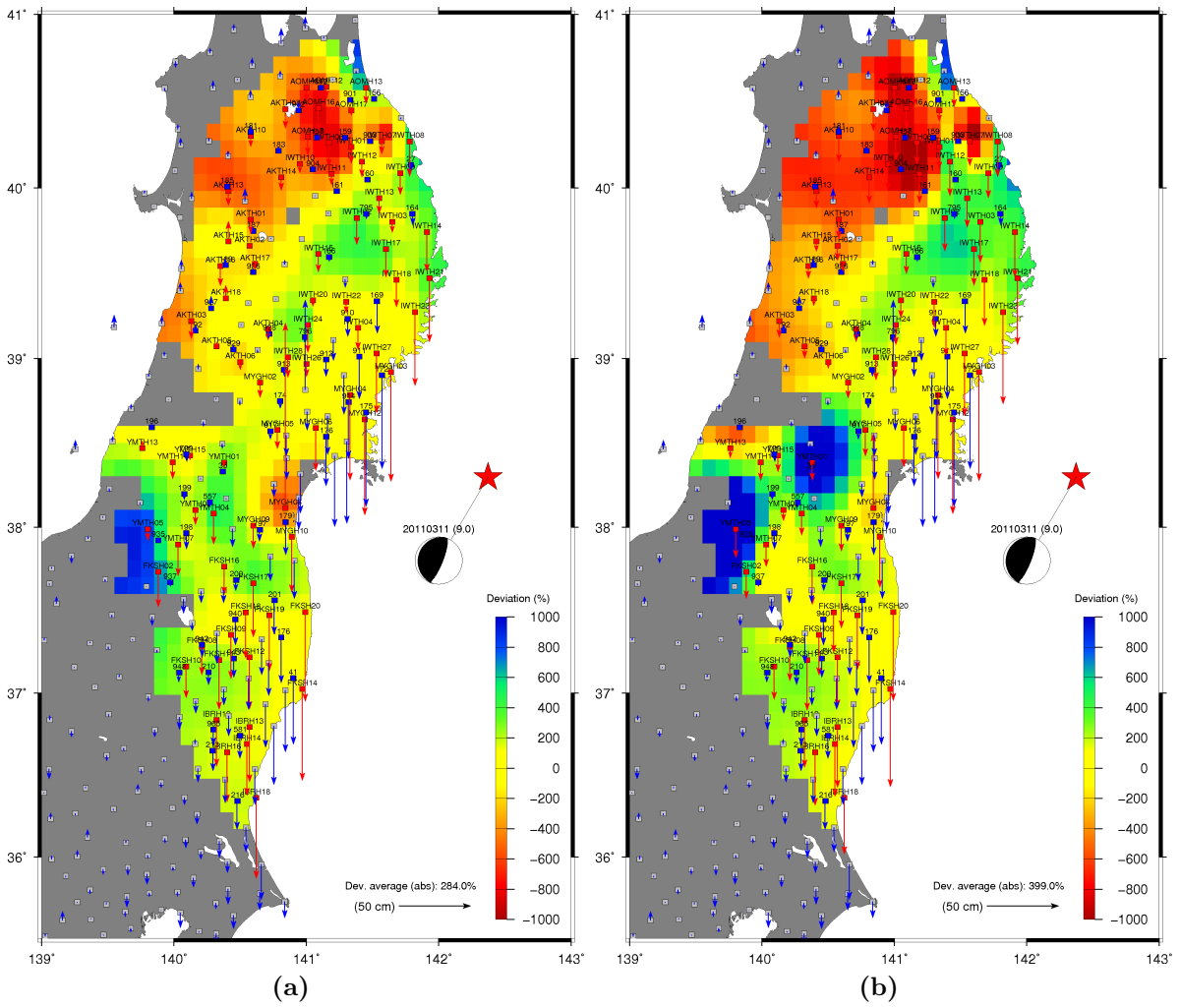

Figure 4.15: Same as Figures 4.14a and 4.14b but for the vertical component.

In order to show how fast we can calculate reasonable static displacements from strong motion records, we demonstrate the application of Eqs. 4.7 and 4.8 to several stations closest to hypocenter location. We calculated the displacements using different length of waveforms. Alternatively, we also calculated the static displacements using Chao et al. (2009) method, but the position of T1 at 25% and T3 at 65% of cumulative energy were determined relative to total energy recorded at stations.

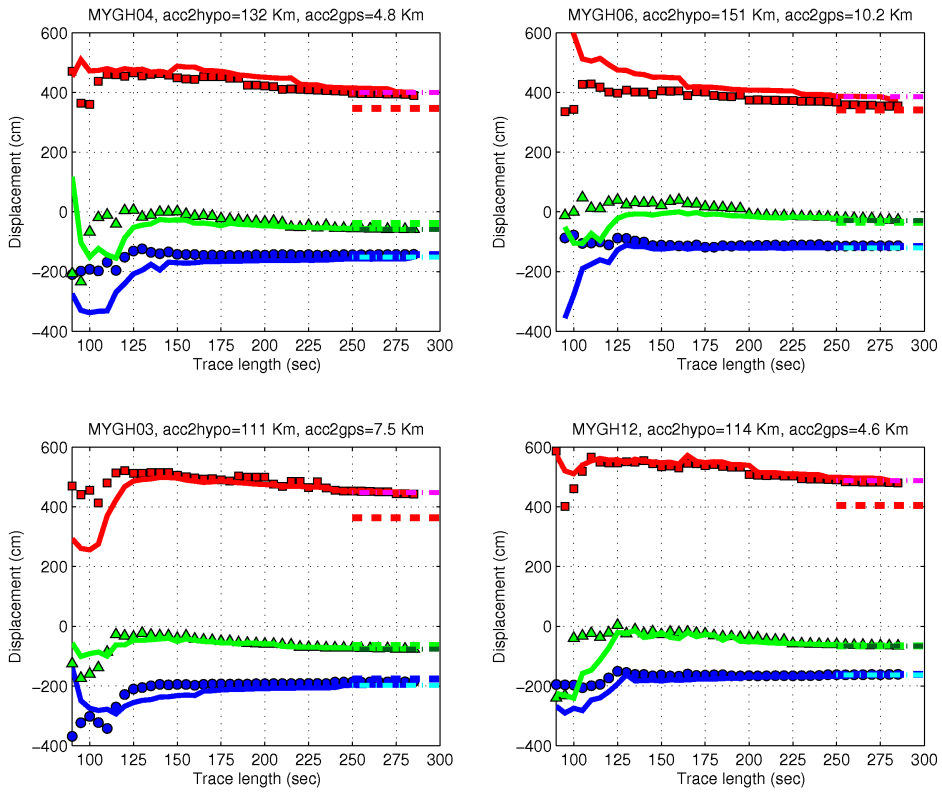

Figure 4.16: Demonstration of static displacements calculated at four stations using different length of waveforms. Red squares, blue circles and green triangles represent displacements calculated following Eqs. 4.7 and 4.8 for east-west, north-south and vertical components, respectively. Solid lines colored in red, blue and green represent displacements calculated using Chao et al. (2009) with T1 and T3 at 25% and 65% of "relatively total energy" recorded at stations. Dashed lines colored in red, blue and green represent nearby GPS data. Dashed-dot lines colored in magenta, cyan and dark green represent displacements obtained from Chao et al. (2009) method using complete 100% of energy.

Figure 4.16 demonstrates the result of displacements calculated using different length of waveforms. We varied the length of waveforms used from 90 to 300 sec with the intervals of 5 sec. Here, we demontrate the application of methods by showing the results of four stations, which are closest to hypocenter location. Both methods produce comparable results, either by using arrival time of T1 and T3 as functions of hypocenter distance, or by using T1 and T3 at 25% and 65% of "relatively total energy" recorded at stations.

Figure 4.16 shows very important aspects of different behaviour of particularly east-west and north-south components, which are respectively perpendicular and parallel to

the trench of subduction zone. On the north-south component, the stable position of static displacements is reached very early, namely about 150 sec after P-wave arrival time. It can be seen at all four stations. The other two components, particularly the east-west component showing the graphics were not yet stable even until 300 sec of waveforms length.

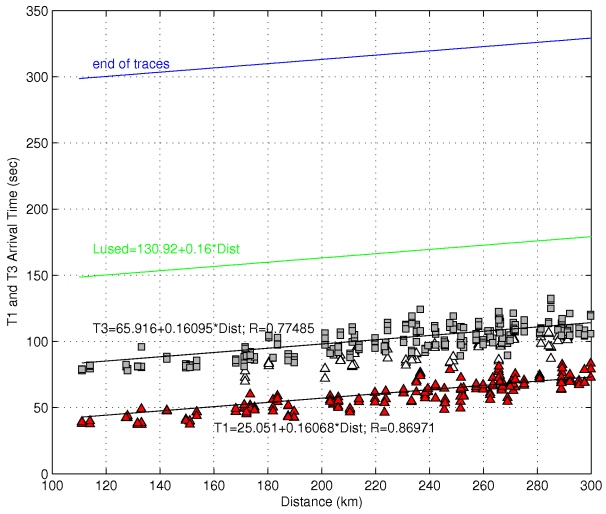

Figure 4.17: Time saved using empirical relation of T1 and T3 as functions of hypocenter distance, or using Chao et al. (2009) with the T1 and T3 at 25% and 65% of "relatively total energy" recorded at stations. Symbol remarks same as 4.13.

$$Lused = 130.92 + 0.16 * distance \tag{4.9}$$

Figure 4.17 illustrates how much time can be saved using relation of T1 and T3 as functions of hypocenter distance or using Chao et al. (2009) with the T1 and T3 at 25% and 65% of "relatively total energy" recorded at stations. The length of waveforms (*Lused*) used to calculate static displacements following Eq. 4.9. Hence, as shown in Figure 4.16, at stations located about 100-150 km from hypocenter location, the first reasonable solutions of static displacements can be obtained at about 150 sec after P-wave arrival time. This method makes it possible to calculate static displacements in real-time. The quality of the results can be improved incrementally when the new data arrive at the stations. The final solutions are obtained after the waveforms completely recorded at the stations.

Chapter 5

Discussion and Conclusions

We have shown that the bilinear line fitting of baseline correction of strong motion records can accurately recover the static displacements if the time points of T1 and T2 are placed at the correct positions. To do it, one possible way is by constraining the displacement trace to a ramp function as proposed by Wu & Wu (2007). The displacement trace must be flattened after the ground reaches its new permanent position. In other words, soon after the earthquake occurrence, the sensor stays at its new position with zero average velocity. Therefore, the baseline correction method essentially attempts to adjust the baseline of the velocity trace to be at zero position before and after the earthquake occurrence.

Using methods suggested by Chao et al. (2009) and Iwan et al. (1985) we obtain coseismic static displacements from strong motion data for several strong earthquakes. The method of Chao et al. (2009) shows much better results in general for all data sets compared to those obtained using the method of Iwan et al. (1985). Application of Chao et al. (2009) method to the data set of the 2011, Mw 9.0 Tohoku earthquake produces satisfactory results, comparable with the GPS measurements. Actually, the method has never been tested before for the earthquakes of very large magnitude (Mw>8.0). This

work has provided additional successful applications using the same method after several previous studies using data sets of the 2003, Mw 6.8 Chengkung earthquake, the 2006, Mw 6.1 Taitung earthquake, the 1999, Mw 7.6 Chi-chi earthquake and the 2007, Mw 7.7 Tocopilla earthquake. In this study, we also show that the method could be successfully applied to the 2003, Mw 8.3 Tokachi-Oki earthquake, and the 2010, Mw 7.8 Mentawai earthquake. It confirms that the threshold of ratio of cumulative energy is appropriate to be used as the standard threshold for the time points determination (i.e. T1 and T3) of bilinear line fitting and flatness-based empirical baseline correction.

Furthermore, we found that the optimized position of cumulative energy ratio for time points T1 and T3 differ between horizontal and vertical components. This may indicate different mechanisms of baseline shifts for horizontal and vertical components. Tilt or rotation of the ground during strong shaking most likely contributes the baseline shift at the horizontal components, as it was also noted by e.g. Boore (2001); Graizer (2005) and Graizer (2006). It happens when the mechanical and electrical zero position of the system in the sensors are not identical at the certain level of strong shaking. Boore (1999); Clinton (2004) and Graizer (2006) noted that the same source also affects the baseline shift in the vertical components but with a much lesser extent compared to the horizontals. Therefore, assuming tilt is one of the main reasons of baseline shift in acceleration data, we propose that the method should be distinguished for horizontal and vertical components.

The variation of time points T1 and T3, which is 25% and 65% of cumulative energy ratio in the baseline correction method proposed by Chao et al. (2009), generally yields reasonable displacements applied to many relatively strong earthquakes. For a very large event like the Tohoku earthquake with moment magnitude of 9.0, however, as shown in Table 5.1, better results can be obtained when T3 is placed at 87%, much larger than T3 position in Chao et al. (2009) method and T1 at 4%, much smaller than T1 in Chao

et al. (2009) method, for horizontal components. For the vertical component, the variation is completely different, T1 is optimized at 24% and T3 at 51%. These results show the behaviour of flatness-based empirical baseline correction method. This implies that T1 and T3 positions depend on the magnitude of earthquake and therefore also on the rupture duration.

We obtain significant improvement of the results when the effect of hypocenter distance is taken into account. In this study we have shown the strong hypocenter distance dependency of time points T1 and T3 in the empirical baseline correction method, particularly for horizontal components. We established a set of relations between time points T1 and T3 as function of hypocenter distance (see Eqs. 4.1 to 4.6). The formulas, however, have not been tested for different cases of large earthquakes. As can be seen in Table 5.1, in the case of the 2011, Mw 9.0 Tohoku earthquake, using such relations we minimized the deviations of vector length between the strong motion derived displacements and GPS measurements of horizontal components from 54.1% become 35.2%. The strong indication of optimal thresholds or position of time points T1 and T3 is also shown by the improvement of the deviation of azimuth or displacement direction from 11.3 to 8.0 degrees at the same results.

Table 5.1: Comparison of displacement deviations using T1 and T3 in this study and in Chao et al. (2009) method

	Deviation		
	Chao et al (2009)	**This study**	
	T1:25%,T3:65%	**(Hor) T1:4%,T3:87%**	
		(Ver) T1:24%,T3:51%	**T1(dist),T3(dist)**
Horizontal (%)	54.1	39.7	35.2
Azimuth (*deg*)	11.3	9.4	8.0

Continued on next page

Table 5.1 – continued from previous page

	Deviation		
	Chao et al (2009)	**This study**	
	T1:25%,T3:65%	**(Hor) T1:4%,T3:87%**	
		(Ver) T1:24%,T3:51%	**T1(dist),T3(dist)**
Vertical (%)	301.7	212.1	193.0

For the vertical displacements, the average deviation is very large, about 301.7%. Using the proposed relation of T1 and T3 as function of distance, the deviation could be minimized to 193.0%. The uncertainties of vertical displacements are relatively larger in far-field data. These contributions increased the average deviations. It has been discussed in Chao et al. (2009), that such problems arise due to the relatively poor signal to noise ratio at large distances. In addition, Wang et al. (2011) noted that for distant stations the strong ground shaking is dominated by far-field body waves which have no contribution to the static displacement but last long and cause relatively large uncertainties in the empirical baseline correction. Fortunately, for the early warning purposes, far-field data at distances of larger than ∼200 km are of less interest.

An interesting feature is observed on relation of T3 as a function of hypocenter distance for vertical component (see Figure 4.9b). Time point T3 position jumps dramatically from the position of near 50% of cumulative energy ratio at distance less than 300 km, to the position of near 100% at distance larger than 300 km. Either before or after this boundary distance, both graphics showing T3 positions are constant, which means a lower distance dependency. We analyzed in more detail the displacement waveforms of vertical component (see Figure 5.1). We have selected waveforms with the azimuth of 180 to 270 degrees from epicenter location. These data represent all station distances. We found, at

a distance of about 300 km, a new phase starts to appear with a little time shift. On the other hand, a phase that exists earlier, which is recorded by near-source stations is getting disappear at about 300 km of distance. We assume that T3 needs a longer time to collect its cumulative energy since the existing phase begins to disappear and a new phase comes a bit later. We interpret that a new phase which comes later likely due to complexity of rupture process (Koketsu et al., 2011; Yoshida et al., 2011).

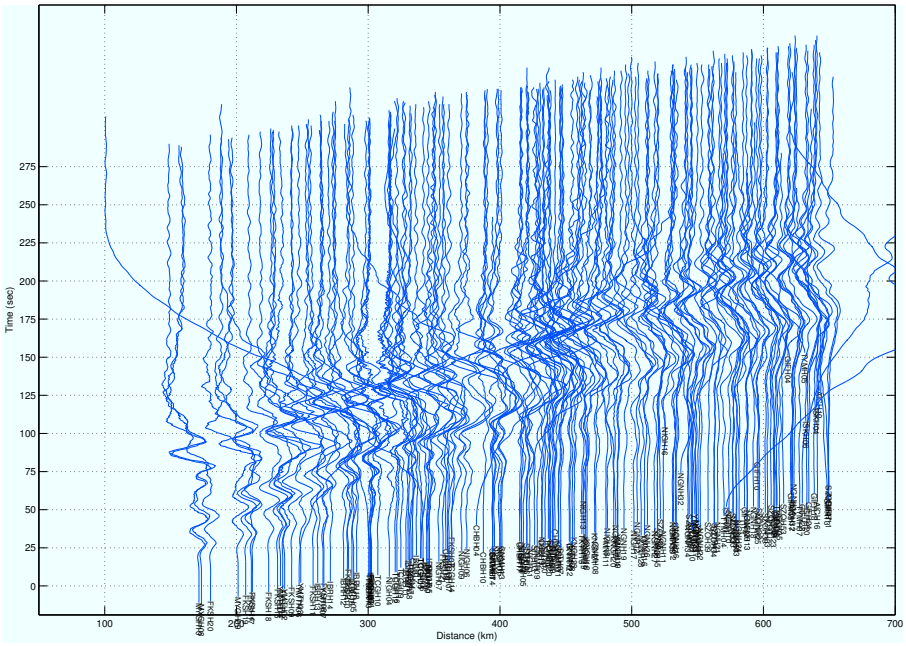

Figure 5.1: Displacement waveforms of vertical component of the 2011, Mw 9.0 Tohoku earthquake

In our study, the hypocenter of 9.0 Tohoku earthquake was simplified as a point source. In fact, the Tohoku earthquake had a very large rupture area. Its rupture model, width and length were complicated. Yoshida et al. (2011) and Maercklin et al. (2012) reported that the rupture process mainly consists of three stages. The first stage occurred with moderate slip at deeper northern part of the fault. The second stage was the largest and longest duration slip, which occurred in the shallow northern part of the rupture area near the hypocenter and centroid location. At the third stage, the rupture propagated to

southern part with small and short duration slip. Such process can be also seen on the phase arrivals in Figure 5.1. The directivity effect of the rupture process may also strongly be one of the reasons of the two main phases occurred at different time or shifted by time delay.

Compared to vertical component, different behaviour is shown at horizontal components. Strong hypocenter distance dependency of T3 position is observed at horizontal components (see Figure 4.9a). We examine in more detail the displacement waveforms of all components (see Figures 5.1 and 5.2). We calculate the velocity of static or plastic deformation which is indicated by the time when the ground has just reached its permanent position. In fact, it is the same physical meaning of T3 that was proposed by Wu & Wu (2007), where T3 is defined as time point when the ground has just reached permanent position. We found that the velocity of static deformation due to Tohoku earthquake is ∼3.5 km/sec. The velocity is similar to the typical velocity of surface waves (e.g. Ducic, 2003). Therefore, we assume that surface waves likely transport most of the static deformation due to strong earthquakes. The strong hypocenter distance dependency of time point T3 position could possibly imply the propagation velocity of static deformation.

In this thesis, we also show that the rapid displacements can be calculated either using arrival time of T1 and T3 as functions of hypocenter distance, or using T1 and T3 at 25% and 65% of relatively total energy received at stations. As shown in Figure 4.16, both methods give comparable results. Using such methods, in case of Tohoku earthquake, at near-source stations with the distance of about 100-150 km from hypocenter location, the first reasonable solutions of static displacements were obtained in ∼150 sec after P-wave arrival time. The resulting displacements are fair, particularly on the vertical component and the horizontal component that perpendicular to the trench (east-west component). For the component that is parallel to the trench (north-south component), the results were

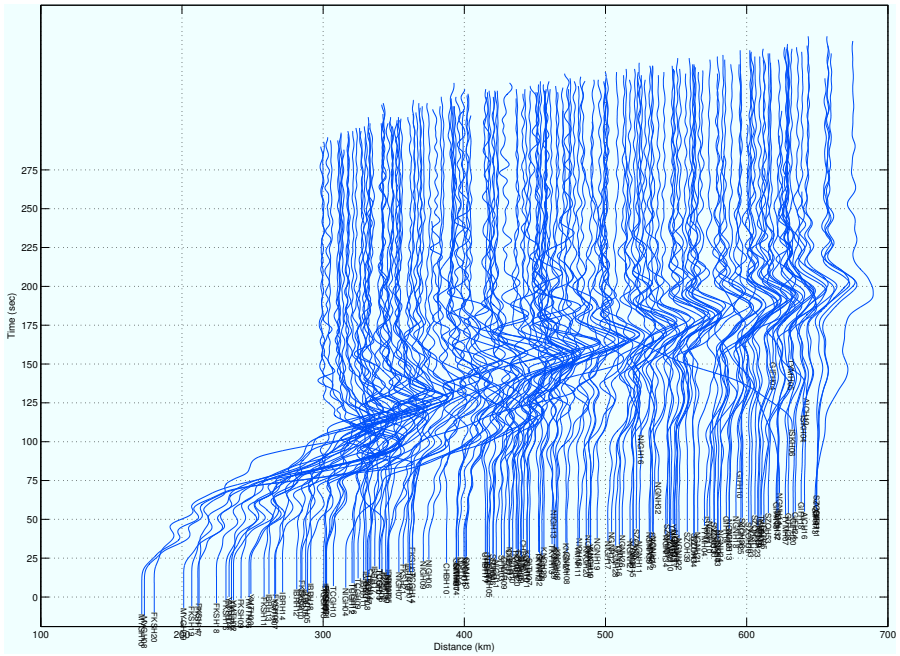

(a)

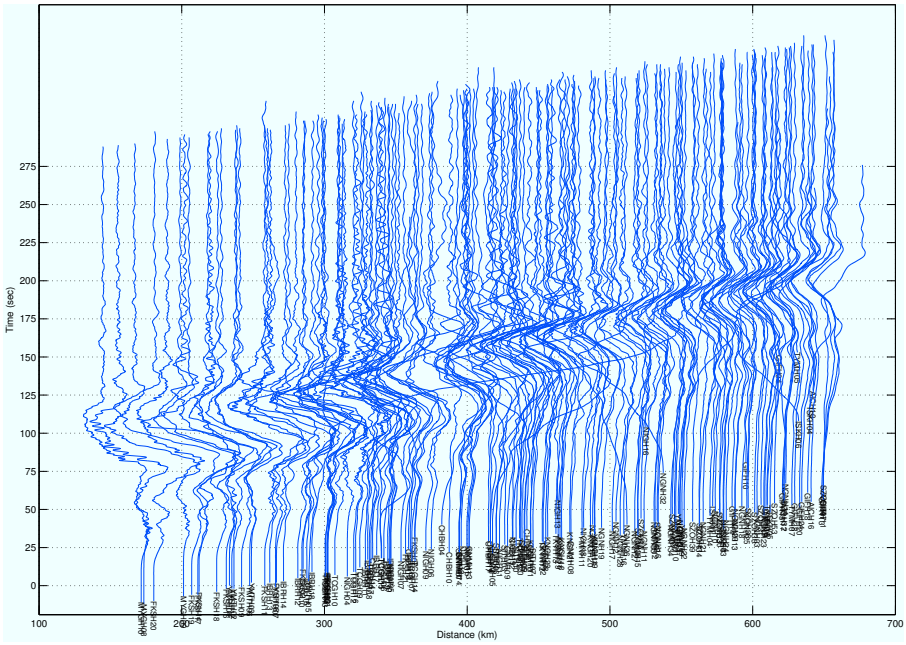

(b)

Figure 5.2: Displacement waveforms of (a) East-west component and (b) North-south component of the 2011, Mw 9.0 Tohoku earthquake.

significantly better (see Figure 4.16). For the two problematic components (east-west and vertical), the quality of results can be improved incrementally with new data arriving at

the stations. This procedure allows the static displacement to be calculated in real-time.

Another important observation related to Figure 4.16, the static displacements at north-south component for all four stations reached the stable position earlier at about 150 sec after P-wave arrival time. This component is parallel to the trench. Whereas, for other two components (east-west and vertical), particularly east-west component, the static displacements at all stations were not stable, even until the waveforms reached their complete 100% of energy at about 300 sec after P-wave arrival time. The slopes of strong motion derived displacement and their misfits to nearby GPS measurements decrease systematically with increasing hypocenter distance.

In general, the results of strong motion derived displacements are larger than the GPS measurements, particularly for east-west component. The possible reason is that the baseline correction method can remove some tilt effects in the strong motion data, but not all. Graizer (2005) reported the same phenomenon at another example using different baseline correction method. We also initially speculate that it could be due to the overshooting effect of displacement. During the earthquake, the overriding plate forced up suddenly and moves toward the subducting plate. Soon after the plate reachs maximum deformation, the overriding plate moves slowly to the opposite direction, namely to the east, in case of Tohoku earthquake. However, we observed in detail the displacement time series (see e.g. Figure 1.1b) and found that the overshooting effect has the time scale about 25 to 50 sec. We also see similar time scale of the overshooting effect from the high-rate GPS data. Therefore, perhaps the overshooting effect does not coincide with what we see in Figure 4.16 that the displacements on east-west component decrease slowly with larger time scale. This figure probably shows numerical problems due to the short time windows used in our calculation. This may be the uncertainty of rapid strong motion derived displacements. The uncertainty, however, decreases with increasing length of the

time windows. In spite of the uncertainty we observed when we use short time windows particularly for the east-west component, the uncertainty is relatively small and it is within the acceptable range for the real-time observation.

Chapter 6

Use of static displacements for rapid moment magnitude estimation

6.1 Introduction

One of the motivations of our study is to optimize the use of valuable rapid coseismic static displacement information from strong motion or GPS data. The earthquake parameter of moment magnitude (Mw) can be calculated from coseismic surface deformation data. Moment magnitude is one of the most crucial parameters for making tsunami warning decisions. It is our hypothesis that with relatively few good measurement of static displacements, moment magnitude with sufficient accuracy can be estimated rapidly enough to be used for tsunami warning.

Methods of rapid moment magnitude estimation have been introduced by many studies before (e.g. Blewitt et al., 2006; Delouis et al., 2009; Singh et al., 2012). Nevertheless, most of methods rely on either static deformation from GPS data or on dynamic displacements from strong motion data. Normally, they need data from at least several

near-epicenter stations. These may take longer time or may not be available at all. Blewitt et al. (2006), for example, needs about 15 minutes of GPS data following earthquake initiation to determine moment magnitude. Our aim here is to investigate whether strong motion data can help in making moment magnitude estimation available more quickly, especially within 5 minutes as required for tsunami warning e.g. in Indonesia.

We learnt from the 2010, Mw 7.8 Mentawai earthquake in Sumatra. The earthquake was recorded by the strong motion network of BMKG (Meteorological, Climatological and Geophysical Agency of Indonesia). Due to the lack of strong motion stations and problems of station maintenance, the earthquake was properly recorded at only two near-epicenter stations within a distance of less than about 200 km. Significant static displacement was recorded at only one near-epicenter station (PPSI, distance of 81 km). This data, however, would be very valuable if we could use it well in near real-time. A case like this may happen again in the future for other large earthquakes in this or other regions.

The Mentawai earthquake is a realistic case that is to be expected in a country like Indonesia, where a good measurement of displacement is recorded at only one near-epicenter station. Based on experience, the question then arises, what we can do or learn from a single vector of displacement?. The displacement vector must be related to the centroid location and magnitude scale of the earthquake. This idea leads us to develop the method of grid search for centroid location with the trial of possible magnitudes by using displacements data from a single station. In principle, additional stations can be included incrementally to improve the quality of magnitudes.

We have shown in this thesis that strong motion data can provide a faster coseismic deformation relative to satellite-based methods (i.e. GPS or InSAR). Here, we demonstrate how we use the static deformation mostly obtained from strong motion data to calculate reasonable moment magnitude very quickly. Due to lack of strong motion data, for certain

events (e.g. for 2004 Sumatra earthquake) we use GPS data from the references, but using the same inversion method.

6.2 Method

Strong shallow earthquakes normally produce permanent or static surface deformations in the vicinity of the epicenter location. Deformation is a function of the earthquake size, location, source mechanism and fault geometry. Using deformation data, we can attempt an inversion for at least some of the earthquake source parameters, for instance, slip at the slab interface and seismic moment of the earthquake. Otherwise, modelling the source mechanism and moment magnitude of strong earthquakes can predict surface deformation near epicenter location.

Okada (1985) proposed a forward modelling method to calculate static surface deformations caused by strong earthquakes. His model uses finite rectangular faults and calculates deformations due to shear and tensile faults in half space. Using the Okada (1985) model, we use as input parameters: the centroid location (latitude, longitude and depth), fault geometry (strike, dip, rake and rupture's area) and average slip of the earthquake to the given formulas (see Eqs. 2.2 to 2.8). We predict static deformation at an observation coordinate on the earth's surface and compare the result with the observation data at the same coordinate.

Slip is computed based on the magnitude and an assumption of Poisson's ratio or elastic shear modulus of the crust structure. Using a grid search method, we search all possibilities of moment and centroid position near hypocenter location. We search iteratively over the moment magnitude range between 6.0 to 9.5 at intervals of 0.1. For each magnitude iteration, we calculate moment using the Hanks & Kanamori (1979) equation

following Eq. 6.1.

$$\log(M_o) = 1.5M_w + 9.1 \tag{6.1}$$

assuming the commonly used elastic shear modulus $\mu = 30\,GPa$, slip value is calculated using Eq. 6.2.

$$M_o = \mu\, D\, A \tag{6.2}$$

where D is the slip average of the whole rupture area (A) on the fault surface. Here, we make the simplification that the slip is homogeneous, that is, it occurs with the same amplitude on the entire fault surface.

The rupture area is calculated using empirical relation of magnitude-area scaling laws. We make another simplification of fault dimensions by assuming a rectangular area. Length (L) and Width (W) of the rupture are calculated following Eqs. 6.3 and 6.4 from Wells & Coppersmith (1994).

$$\log(L) = 0.63M_w - 2.86 \tag{6.3}$$

$$\log(W) = 0.41M_w - 1.61 \tag{6.4}$$

We observe static displacement at a strong motion station near the epicenter. On the other hand we compare this with predicted static displacement at the same location using the method of Okada (1985) by forward modelling. We calculate the misfit between observed and predicted displacements. During grid search, the centroid position is moved

over a sufficiently large area on the slab interface.

For misfit calculation between observation and prediction displacements data, we weight the vertical displacements 25%, i.e. relatively smaller than horizontal components. Normally, vertical deformation is much smaller than horizontal deformation. Misfit is calculated using Eq. 6.5 below,

$$Misfit = (\Delta EW + \Delta NS + 0.25 * \Delta UD)/3 \tag{6.5}$$

where ΔEW, ΔNS and ΔUD are differences in the east-west, north-south and vertical components between observed and predicted displacements, respectively.

The parameters (i.e. latitude, longitude, depth, strike and dip) for grid point at epicenter location are obtained from the slab model slab1.0 of USGS (Hayes et al., 2012). The grid point is then used as reference to set other grid points within a length and width of 400 km and 140 km, respectively. The spacing between grid points is fixed at 20 km. Such large values of grid search area and spacing are considered sufficient. The grid of 147 points is centered at the hypocenter location.

The rake of typical megathrust earthquakes can be approximated to be close to 90 degrees. However, in this study, we have tested the method using three possibilities of rake for each grid point. First, we use rake from the reference, GCMT (Global Centroid Moment Tensor). Second, we use rake of 90 degrees. Third, rake is searched or optimized between 70 to 110 degrees at intervals of 1 degree. In this case the best rake will be selected where the misfit reaches its minimum value.

Using the grid search method, the final result of moment magnitude will be selected if the observed and predicted displacements have minimum misfit. Additional stations can be incorporated easily to improve the quality of final results. However, we want to focus

here on the case of one available station with good measurement, as this is what can be typically expected to be realistic in Indonesia.

6.3 Results

We apply the method to calculate moment magnitudes of several strong earthquakes as listed in Table 6.2. The reference stations used for the earthquakes are listed in Table 6.1. In order to test the consistency of our results of moment magnitude, for the case of the Tohoku earthquake, we also used other nearby strong motion stations for the references. The results of moment magnitude using different reference stations are shown in Table 6.3.

Figures 6.1 and 6.2 show the results for the earthquakes listed in Table 6.2 using rake of 90 degrees.

Table 6.1: Reference stations used to calculate moment magnitude by grid search method

Earthquake	**Station**	**Lat**	**Lon**	**Distance (km)**
Sumatra (2004)	R171	2.96	95.52	64.97
Tohoku (2011)	MYGH12	38.64	141.44	89.66
	MYGH03	38.92	141.64	94.04
	MYGH04	38.79	141.33	105.9
	IWTH27	39.03	141.53	109.5
	MYGH06	38.59	141.07	118.0
Maule (2010)	CONZ	-36.84	-73.02	107.2
Tokachi-Oki (2003)	TKCH06	42.89	143.06	142.3
Mentawai (2010)	PPSI	-2.77	100.01	80.67
Tocopilla (2007)	PB05	-22.85	-70.20	79.86
Tokachi-Oki aft. (2003)	0144	42.13	142.94	70.35

The GPS data at stations R171, CONZ and 0144 are obtained from Hoechner et al. (2008), Delouis et al. (2010) and Larson & Miyazaki (2008), respectively.

Table 6.2: Results of rapid moment magnitude estimation using single station

Earthquake	**Moment magnitude (Mw)**			
	Ref. (GCMT)	**Rake(λ) from ref.**	**Rake=90**	**Rake opt.**
Tohoku (2011)	9.1	9.2 (λ=88)	9.2	9.2 (λ=73)
Sumatra (2004)	9.0	9.2 (λ=111)	8.6	8.6 (λ=91)
Maule (2010)	8.8	9.0 (λ=116)	8.9	8.6 (λ=109)
Tokachi-Oki (2003)	8.3	8.5 (λ=132)	8.2	8.1 (λ=102)
Mentawai (2010)	7.8	7.8 (λ=96)	8.1	8.3 (λ=74)
Tocopilla (2007)	7.7	7.7 (λ=98)	7.3	7.7 (λ=102)
Tokachi-Oki aft. (2003)	7.3	7.3 (λ=86)	7.3	7.3 (λ=81)

Table 6.3: Results of rapid moment magnitude estimation using single different station for the 2011, Mw 9.1 (GCMT) Tohoku earthquake

Station	**Moment magnitude (Mw)**		
	Rake(λ)=88 (ref.)	**Rake=90**	**Rake opt.**
MYGH12	9.2	9.2	9.2 (λ=73)
MYGH03	9.0	9.0	9.0 (λ=82)
MYGH04	9.0	9.0	9.1 (λ=71)
IWTH27	8.9	8.9	9.0 (λ=82)
MYGH06	8.9	9.2	9.2 (λ=72)

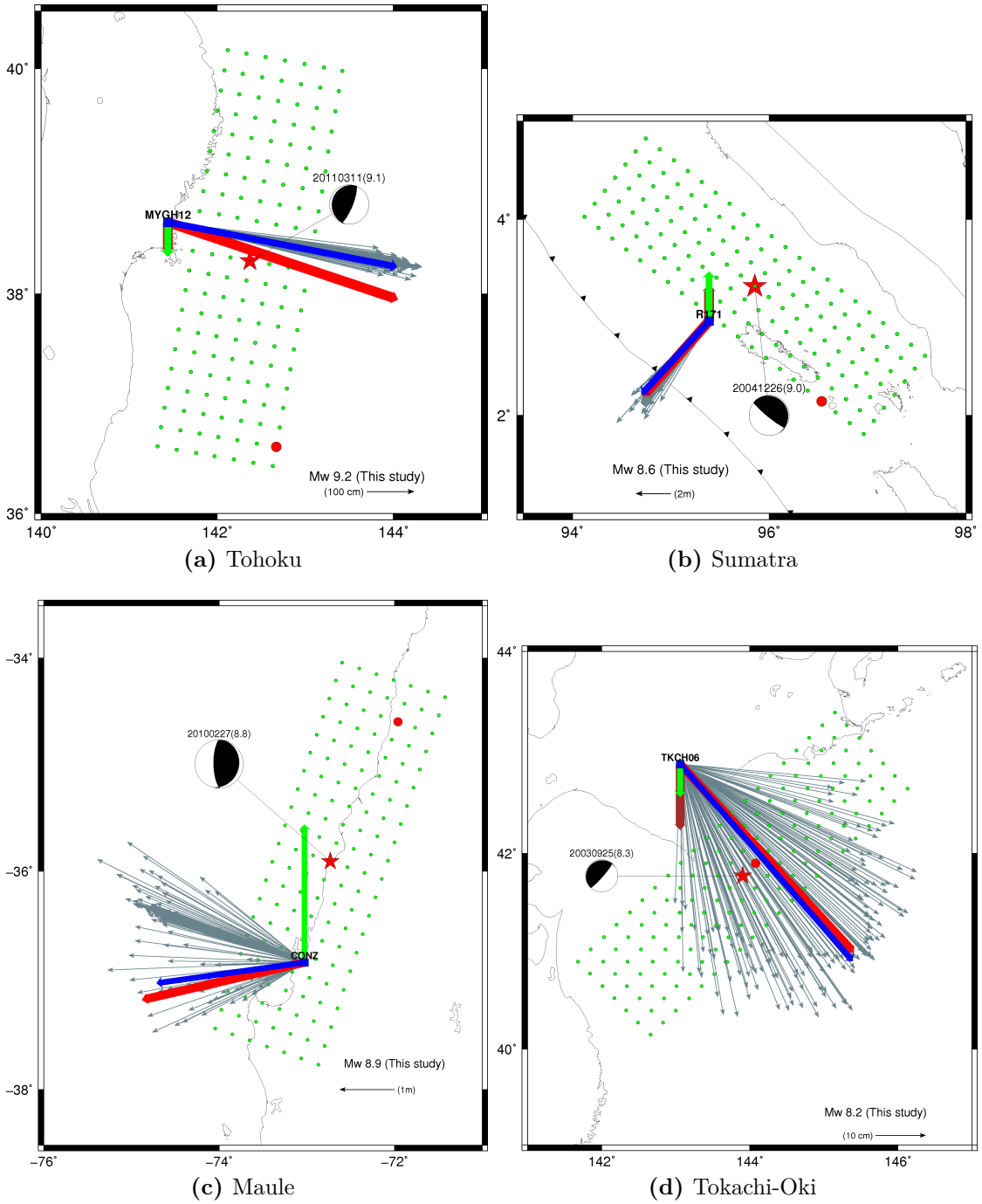

(a) Tohoku **(b)** Sumatra

(c) Maule **(d)** Tokachi-Oki

Figure 6.1: Results of rapid moment magnitudes calculated using single near-epicenter station for (6.1a) Tohoku earthquake, (6.1b) Sumatra earthquake, (6.1c) Maule earthquake and (6.1d) Tokachi-Oki earthquake. Rake is fixed at 90 degrees. Red and brown arrows represent displacements data from the references, respectively for horizontal and vertical components. Blue and green arrows represent selected predicted displacements with minimum misfit to reference data. Gray arrows represent trial displacements. Small green circles indicate grid points used for grid search and red circles indicate selected centroid positions which produce final predicted displacements. Beach balls show focal mechanism solutions from GCMT.

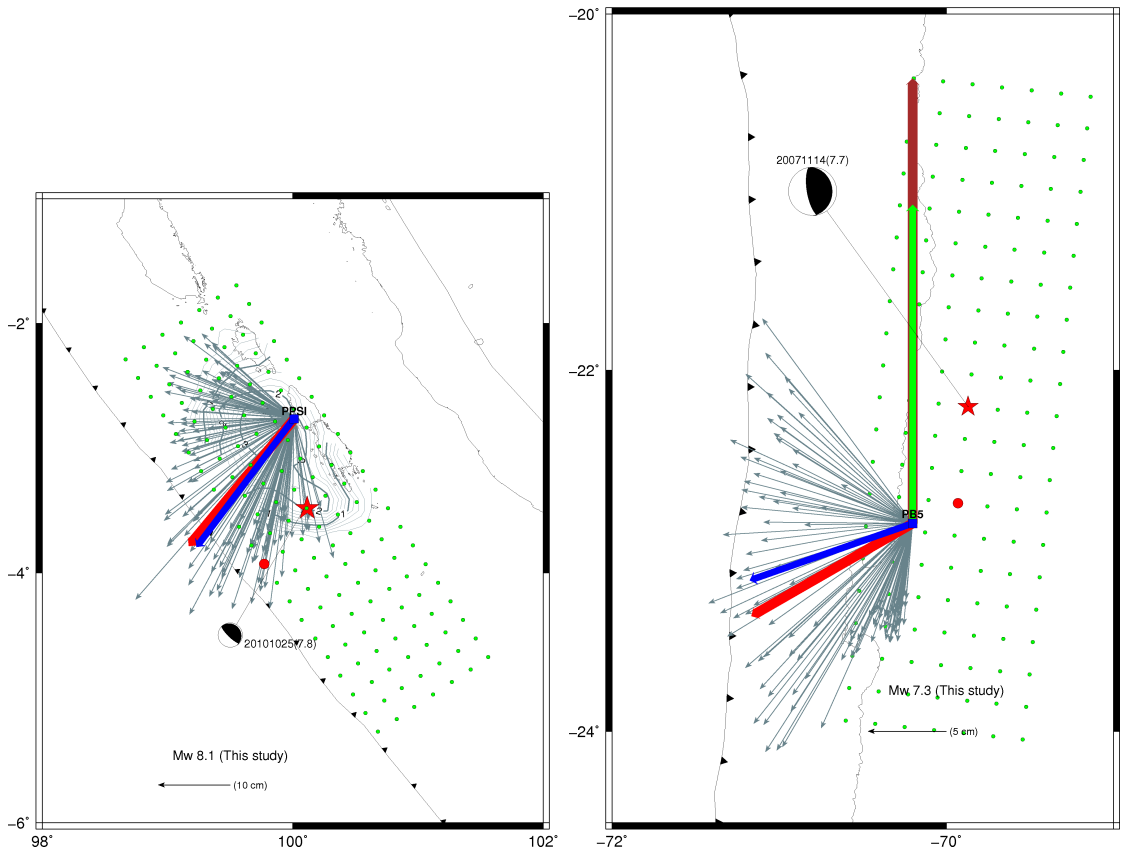

(a) Mentawai **(b)** Tocopilla

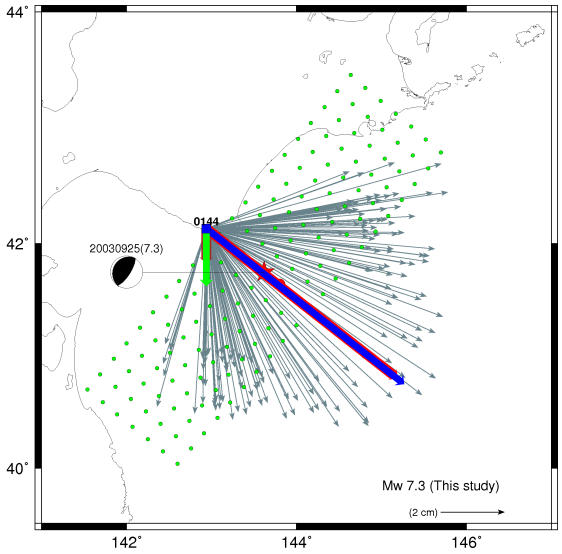

(c) Tokachi-Oki aftershock

Figure 6.2: Continued from Figure 6.1: (6.2a) Mentawai earthquake, (6.2b) Tocopilla earthquake and (6.2c) Tokachi-Oki aftershock earthquake.

6.4 Discussion and Conclusions

We have demonstrated that we can calculate reasonable moment magnitude of relatively strong earthquakes using single strong motion or GPS station. Assuming the references have the correct magnitudes, we compared the results of magnitude using our method and reference magnitudes.

We have used different rakes for the moment magnitudes calculation. By using the rake from reference solutions we obtain magnitudes very close to the reference magnitudes with an average deviation of 0.1. Assuming the rake is equal to 90 degrees, the average deviation is 0.2. Optimizing rake between 70 and 110 degrees by selecting the best fitting rake to produce minimum misfit between observed and predicted data, the average deviation is also 0.2.

We have tested how consistent the results are if using different stations where the data are available for the references. For example, for the Tohoku earthquake, the result of moment magnitude was close to the reference magnitude. Consistency of the results can be tested by using different stations for the same event. We compared the results using five different stations. We show that, even with rake fixed at 90 degrees, the average deviation is very small, namely 0.12.

It is not surprising that the best results can be obtained when we use rakes from the reference (GCMT). In reality, however, of course we have no rake from reference at the time of earthquake occurrence. As other two possibilities, we can use either a rake approximated to 90 degrees or search for the best rake. Both methods result in the same average deviations. The method of optimizing rake takes more time for the calculation process. Therefore, for early warning purposes, we suggest calculating moment magnitude using the method in this study with rake fixed at 90 degrees.

It is understandable that the results of magnitude using the method presented here are slightly different from the GCMT magnitudes. In this study, magnitudes have been estimated under several simplifying assumptions. First, we made the simplification of fault dimension, where we assumed a rectangular rupture area. Second, we used scaling laws of empirical relation between moment magnitude and rupture area. Third, we assumed that slip occurs with homogeneous amplitudes across the fault plane. Fourth, rake was assumed to be 90 degrees.

Despite the many assumptions introduced to the method, the results in terms of moment magnitudes using data from only one strong motion or GPS station are quite encouraging. In fact, a full slip inversion with much more data and fewer assumptions can produce moment magnitude with better accuracy. However, the goal of this method is rapid moment magnitude estimation for e.g. tsunami early warning purposes. The speed of data processing with reasonable results is critical. The accuracy of moment magnitude can be improved incrementally when the new data are obtained.

List of Figures

List of Tables

Bibliography

Aki, K. & Richards, P., 2002, Quantitative Seismology, second edition, *University Science Books, Sausalito*.

Altiner, Y., Söhne, W., Güney, C., Perlt, J., Wang, R., & Muzli, M., 2012, A Geodetic Study of the 23 October 2011 Van , Turkey earthquake, *Tectonophysics*, (October), 1–15.

Aoi, S., Kunugi, T., & Fujiwara, H., 2004, Strong-Motion Seismograph network operated by NIED : K-NET and KiK-net, *Journal of Japan Association for Earthquake Engineering*, **4**(3), 65–74.

Béjar-Pizarro, M., Carrizo, D., Socquet, a., Armijo, R., Barrientos, S., Bondoux, F., Bonvalot, S., Campos, J., Comte, D., de Chabalier, J. B., Charade, O., Delorme, a., Gabalda, G., Galetzka, J., Genrich, J., Nercessian, a., Olcay, M., Ortega, F., Ortega, I., Remy, D., Ruegg, J. C., Simons, M., Valderas, C., & Vigny, C., 2010, Asperities and barriers on the seismogenic zone in North Chile: state-of-the-art after the 2007 Mw 7.7 Tocopilla earthquake inferred by GPS and InSAR data, *Geophysical Journal International*, **183**(1), 390–406.

Blewitt, G., Kreemer, C., Hammond, W. C., Plag, H.-P., Stein, S., & Okal, E., 2006, Rapid determination of earthquake magnitude using GPS for tsunami warning systems, *Geophysical Research Letters*, **33**(11), 6–9.

Boore, D., 1999, Effect of baseline corrections on response spectra for two recordings of the 1999 Chi-Chi, Taiwan, earthquake, *U.S. Geol. Surv. Open-File Rept.*, pp. 99–545, 37 pp.

Boore, D., 2001, Effect of baseline corrections on displacements and response spectra for several recordings of the 1999 Chi-Chi, Taiwan, earthquake, *Bulletin of the Seismological Society of America*, (October), 1199–1211.

Boore, D., 2003, Analog-to-digital conversion as a source of drifts in displacements derived from digital recordings of ground acceleration, *Bulletin of the Seismological Society of America*, **93**(5), 2017–2024.

Boroschek, R., Soto, P., & Leon, R., 2008, Terremotos de Chile - Earthquakes of Chile, *http://terremotos.ing.uchile.cl/registros/123*.

Chao, W.-A., Wu, Y.-M., & Zhao, L., 2009, An automatic scheme for baseline correction of strong-motion records in coseismic deformation determination, *Journal of Seismology*, **14**(3), 495–504.

Chinnery, M., 1963, The stress changes that accompany strike-slip faulting, *Bulletin of the Seismological Society of America*, **53**(5), 921–932.

Chiu, H., 1997, Stable baseline correction of digital strong-motion data, *Bulletin of the Seismological Society of America*, **87**(4), 932–944.

Clinton, J. F., 2004, Modern Digital Seismology - Instrumentation, and Small Amplitude Studies for the Engineering world, *PhD Thesis, California Institute of Technology*.

Collings, R., Lange, D., Rietbrock, a., Tilmann, F., Natawidjaja, D., Suwargadi, B., Miller, M., & Saul, J., 2012, Structure and seismogenic properties of the Mentawai segment of the Sumatra subduction zone revealed by local earthquake traveltime tomography, *Journal of Geophysical Research*, **117**(B1), B01312.

Delouis, B., Charlety, J., & Vallee, M., 2009, A Method for Rapid Determination of Moment Magnitude Mw for Moderate to Large Earthquakes from the Near-Field Spectra of Strong-Motion Records (MWSYNTH), *Bulletin of the Seismological Society of America*, **99**(3), 1827–1840.

Delouis, B., Nocquet, J. M., & Vallée, M., 2010, Slip distribution of the February 27, 2010 Mw = 8.8 Maule Earthquake, central Chile, from static and high-rate GPS, InSAR, and broadband teleseismic data, *Geophysical Research Letters*, **37**(17), L17305.

Ducic, V., 2003, Ionospheric remote sensing of the Denali Earthquake Rayleigh surface waves, *Geophysical Research Letters*, **30**(18), 1951.

Emore, G. & Haase, J., 2007, Recovering seismic displacements through combined use of 1-Hz GPS and strong-motion accelerometers, *Bulletin of the Seismological Society of America*, **97**(2), 357–378.

Geosig, 2009, GSK-166 Uniaxial Linear Shaking Table, *GeoSIG Ltd.*

Graizer, V., 1979, Determination of the true ground displacement by using strong motion records, *Izvestiya Phys. Solid Earth.*

Graizer, V., 1989, Bearing on the problem of inertial seismometry, *Izv. USSR Acad. Sci., Physics Solid Earth*, **25**(3), 197–204.

Graizer, V., 2006, Tilts in Strong Ground Motion, *Bulletin of the Seismological Society of America*, **96**(6), 2090–2102.

Graizer, V., 2010, Strong Motion Recordings and Residual Displacements: What Are We Actually Recording in Strong Motion Seismology?, *Seismological Research Letters*, **81**(4), 635–639.

Graizer, V. M., 2005, Effect of tilt on strong motion data processing, *Soil Dynamics and Earthquake Engineering*, **25**(3), 197–204.

Hanks, T. & Kanamori, H., 1979, A moment magnitude scale, *J. geophys. Res*, **84**.

Havskov, J. & Ottemöller., L., 2010, *Routine data processing in earthquake seismology*, Springer.

Hayes, G. P., Wald, D. J., & Johnson, R. L., 2012, Slab1.0: A three-dimensional model of global subduction zone geometries, *Journal of Geophysical Research*, **117**(B1), 1–15.

Hill, E. M., Borrero, J. C., Huang, Z., Qiu, Q., Banerjee, P., Natawidjaja, D. H., Elosegui, P., Fritz, H. M., Suwargadi, B. W., Pranantyo, I. R., Li, L., Macpherson, K. a., Skanavis, V., Synolakis, C. E., & Sieh, K., 2012, The 2010 M w 7.8 Mentawai earthquake: Very shallow source of a rare tsunami earthquake determined from tsunami field survey and near-field GPS data, *Journal of Geophysical Research*, **117**(B6), 1–21.

Hoechner, A., Babeyko, A. Y., & Sobolev, S. V., 2008, Enhanced GPS inversion technique applied to the 2004 Sumatra earthquake and tsunami, *Geophysical Research Letters*, **35**(8), L08310.

Iwan, W., Moser, M., & Peng, C., 1985, Some observations on strong-motion earthquake measurement using a digital accelerograph, *Bulletin of the Seismological Society of America*, **75**(October), 1225–1246.

Kanamori, H., 1972, Mechanism of tsunami earthquakes, *Physics of the earth and planetary interiors*, **6**, 346–359.

Kanamori, H., 1977, The energy release in great earthquakes, *J. geophys. Res*, **82**.

Kelleher, J. a., 1972, Rupture zones of large South American earthquakes and some predictions, *Journal of Geophysical Research*, **77**(11), 2087.

Kinemetrics, 2005, User Guide, Episensor - Force Balance Accelerometer Model FBA ES-T, *Kinemetrics*, (Document 301900).

Koketsu, K., Yokota, Y., Nishimura, N., Yagi, Y., Miyazaki, S., Satake, K., Fujii, Y., Miyake, H., Sakai, S., Yamanaka, Y., & Okada, T., 2011, A unified source model for the 2011 Tohoku earthquake, *Earth and Planetary Science Letters*, **310**(3-4), 480–487.

Larson, K. & Miyazaki, S., 2008, Resolving static offsets from high-rate GPS data: the 2003 Tokachi-oki earthquake, *Earth Planets and Space (EPS)*, pp. 801–808.

Larson, K. M., 2009, GPS seismology, *Journal of Geodesy*, **83**(3-4), 227–233.

Lay, T., Ammon, C. J., Kanamori, H., Yamazaki, Y., Cheung, K. F., & Hutko, a. R., 2011, The 25 October 2010 Mentawai tsunami earthquake (M w 7.8) and the tsunami hazard presented by shallow megathrust ruptures, *Geophysical Research Letters*, **38**(6), 2–6.

Lee, S.-J., Huang, B.-S., Ando, M., Chiu, H.-C., & Wang, J.-H., 2011, Evidence of large scale repeating slip during the 2011 Tohoku-Oki earthquake, *Geophysical Research Letters*, **38**(19), L19306.

Maercklin, N., Festa, G., Colombelli, S., & Zollo, A., 2012, Twin ruptures grew to build up the giant 2011 Tohoku, Japan, earthquake., *Scientific reports*, **2**, 709.

Motagh, M., Schurr, B., Anderssohn, J., Cailleau, B., Walter, T. R., Wang, R., & Villotte, J.-P., 2010, Subduction earthquake deformation associated with 14 November 2007, Mw 7.8 Tocopilla earthquake in Chile: Results from InSAR and aftershocks, *Tectonophysics*, **490**(1-2), 60–68.

Muzli, M., Saul, J., Asch, G., Wang, R., & Tilmann, F., 2011, Coseismic displacement of the 2010 , Mw 7 . 8 Mentawai earthquake obtained from Strong Motion Data, *Geophysical Research Abstracts*, **13**(2007), 10653.

Newman, A. V., Hayes, G., Wei, Y., & Convers, J., 2011, The 25 October 2010 Mentawai tsunami earthquake, from real-time discriminants, finite-fault rupture, and tsunami excitation, *Geophysical Research Letters*, **38**(5).

Okada, Y., 1985, Surface deformation due to shear and tensile faults in a half-space, *Bulletin of the Seismological Society of America*, **75**(4), 1135–1154.

Peyrat, S., Madariaga, R., Buforn, E., Campos, J., Asch, G., & Vilotte, J. P., 2010, Kinematic rupture process of the 2007 Tocopilla earthquake and its main aftershocks from teleseismic and strong-motion data, *Geophysical Journal International*, **182**(3), 1411–1430.

Razinkov, O. G., 2012, GeoDAS Software Manual, *GeoSIG Ltd.*

Rodgers, P., 1968, The response of the horizontal pendulum seismometer to Rayleigh and Love waves, tilt, and free oscillations of the earth, *Bulletin of the Seismological Society of America*, **58**(5).

Ruff, L. & Kanamori, H., 1983, Seismic coupling and uncoupling at subduction zones, *Tectonophysics*, **99**, 99–117.

Ruiz, S., Kausel, E., Campos, J., Saragoni, G. R., & Madariaga, R., 2010, Identification of High Frequency Pulses from Earthquake Asperities Along Chilean Subduction Zone Using Strong Motion, *Pure and Applied Geophysics*, **168**(1-2), 125–139.

Rupakhety, R., Halldorsson, B., & Sigbjörnsson, R., 2009, Estimating coseismic deformations from near source strong motion records: methods and case studies, *Bulletin of Earthquake Engineering*, **8**(4), 787–811.

Sagiya, T., Miyazaki, S., & Tada, T., 2000, Continuous GPS array and present-day crustal deformation of Japan, *Pure and applied Geophysics*, **157**, 2303–2322.

Schreiber, K. U., Hautmann, J. N., Velikoseltsev, a., Wassermann, J., Igel, H., Otero, J., Vernon, F., & Wells, J.-P. R., 2009, Ring Laser Measurements of Ground Rotations for Seismology, *Bulletin of the Seismological Society of America*, **99**(2B), 1190–1198.

Schurr, B., Asch, A., Sodoudi, F., Manzanares, A., Ritter, O., & Klotz, J., 2009, The Integrated Plate Boundary Observatory Chile (IPOC) in the northern Chile seismic gap, *Geophysical Research Abstract*, **11**, 11040.

Singh, S. C., Hananto, N., Mukti, M., Permana, H., Djajadihardja, Y., & Harjono, H., 2011, Seismic images of the megathrust rupture during the 25th October 2010 Pagai earthquake, SW Sumatra: Frontal rupture and large tsunami, *Geophysical Research Letters*, **38**(16), 1–6.

Singh, S. K., Perez-Campos, X., Iglesias, a., & Melgar, D., 2012, A Method for Rapid Estimation of Moment Magnitude for Early Tsunami Warning Based on Coastal GPS Networks, *Seismological Research Letters*, **83**(3), 516–530.

Sobolev, S. V., Babeyko, A. Y., Wang, R., Hoechner, A., Galas, R., Rothacher, M., Sein, D. V., Schröter, J., Lauterjung, J., & Subarya, C., 2007, Tsunami early warning using GPS-Shield arrays, *Journal of Geophysical Research*, **112**(B8), B08415.

Stein, S. & Wysession, M., 2003, An introduction to seismology, earthquakes, and earth structure, *Blackwell Publishing*.

Suzuki, W., Aoi, S., Sekiguchi, H., & Kunugi, T., 2011, Rupture process of the 2011 Tohoku-Oki mega-thrust earthquake (M9.0) inverted from strong-motion data, *Geophysical Research Letters*, **38**(July), 2–7.

Trifunac, M., 1971, Zero baseline correction of strong-motion accelerograms, *Bulletin of the Seismological Society of America*, **61**(5), 1201–1211.

Trifunac, M. & Todorovska, M., 2001, A note on the useable dynamic range of accelero-

graphs recording translation, *Soil Dynamics and Earthquake Engineering*, **21**(4), 275–286.

Wang, R., Schurr, B., Milkereit, C., Shao, Z., & Jin, M., 2011, An Improved Automatic Scheme for Empirical Baseline Correction of Digital Strong-Motion Records, *Bulletin of the Seismological Society of America*, **101**(5), 2029–2044.

Wang, R., Parolai, S., Ge, M., & Jin, M., 2012, The 2011 Mw 9 . 0 Tohoku Earthquake : Comparison of GPS and Strong- Motion Data, *accepted by Bulletin of the Seismological Society of America*.

Wells, D. & Coppersmith, K., 1994, New empirical relationships among magnitude, rupture length, rupture width, rupture area, and surface displacement, *Bulletin of the Seismological Society of America*, **84**(4), 974–1002.

Wjayanto, 2007, Magnitude determination using acceleration records from the Indonesian strong motion network, *Bulletin of IISEE*, (45), 115–120.

Wu, Y.-M. & Wu, C.-F., 2007, Approximate recovery of coseismic deformation from Taiwan strong-motion records, *Journal of Seismology*, **11**(2), 159–170.

Wu, Y.-M., Chen, Y.-G., Chang, C.-H., Chung, L.-H., Teng, T.-L., Wu, F. T., & Wu, C.-F., 2006, Seismogenic structure in a tectonic suture zone: With new constraints from 2006 Mw6.1 Taitung earthquake, *Geophysical Research Letters*, **33**(22), 1–5.

Wu, Y. M., Chen, Y. G., Shin, T. C., Kuochen, H., Hou, C. S., Hu, J. C., Chang, C. H., Wu, C. F., & Teng, T. L., 2006, Coseismic versus interseismic ground deformations, fault rupture inversion and segmentation revealed by 2003 Mw 6.8 Chengkung earthquake in eastern Taiwan, *Geophysical Research Letters*, **33**(2), 2–5.

Yoshida, K., Miyakoshi, K., & Irikura, K., 2011, Source process of the 2011 off the Pacific

coast of Tohoku Earthquake inferred from waveform inversion with long-period strong-motion records, *Earth, Planets and Space*, **63**(7), 577–582.

ACKNOWLEDGEMENT

1. PD. Dr. Günter Asch as the advisor of my study. He brought me to Germany and gave me the chance to pursue my dream to become a Doctor. He never feels tired of repeating explanations, endless supports until I finished my study. For me, he almost knows everything in seismology.

2. Dr. Joachim Saul as another advisor of my PhD work who spent a lot of time for discussion and corrected my thesis carefully. He gave me high motivations and always reminds me not only to write the thesis but also to "sell" the ideas. He made me feel more confident.

3. Prof. Dr. Serge A. Shapiro at Freie Universität Berlin as one of the reviewers of this thesis for the encouraging comments. I know him for a long time as one of the best professors in Geophysics.

4. Committee members of my disputation: PD. Dr. Günter Asch, Prof. Dr. Serge A. Shapiro, Prof. Dr. Rainer Kind, PD. Dr. Ekkehard Scheuber and Dr. Carsten Dinske for reading my thesis and giving encouraging comments.

5. Dr. Rongjiang Wang for discussion and providing many softwares which are the important tools for my study.

6. Prof. Dr. Rainer Kind and Prof. Dr. Frederik Tilmann (Head of the Section 2.4 Seismology at GFZ-Potsdam) for the discussion and giving inspirations, as well as other members in the section. Especially, Dr. Tuna Eken for the encouraging discussion, Amerika Manzanares, Dr. Christoph Sens-Schönfelder, Dr. Angelo Strollo, Dr. Peter Evans and Dr. Forough Sodoudi for reading the thesis, my roommate Peter Gäbler for translating Abstract into German and other roommates who ever

bothered by my short questions. They made me feel comfortable working in the section.

7. Karl-Heinz Jäckel for the discussion and making experiments being carried out, as well as Dr. Heiko Woith and Erwin Günther for preparing shaking table and all supports during experiments at the shaking table laboratory.

8. Dr. Jörn Lauterjung for providing financial support from GFZ-Potsdam in the frame of GITEWS (German Indonesian Tsunami Early Warning System) project.

9. Dr. P.J. Prih Harjadi for supporting my study and giving recommendation of additional financial support from BMKG.

10. Dr. Fauzi and Dr. Horst Letz at BMKG for supporting, giving recommendation and motivations to pursue a PhD degree.

11. Dr. Makky Sandra Jaya as well as other close friends from Indonesia, who also in pursuing PhD degrees at GFZ-Potsdam, Andri Hendriyana, Mochamad Nukman, Muksin, Muhamad Andhika and Sintia Windhi, for inspirations and discussion on many issues related to PhD work, everyday life and also updated news from Indonesia.

12. My lovely mother, wife and children who always make me happy. They give me energy and endless supports.

Appendix A

Orientation angle (θ) of KiK-Net boreholes stations

Source: *http* : *//www.hinet.bosai.go.jp/st_info/detail/* (last accessed December 2011)

Sta	Lat(N)	Lon(E)	θ (deg)	Sta	Lat(N)	Lon(E)	θ (deg)	Sta	Lat(N)	Lon(E)	θ (deg)
ABSH01	44.528	142.84	1	IBRH18	36.363	140.62	0	NIGH11	37.173	138.74	1
ABSH02	44.423	143.03	-2	IBRH19	36.214	140.09	2	NIGH12	37.224	138.98	-49
ABSH03	44.384	143.24	5	IBRH20	35.828	140.73	-14	NIGH13	37.054	138.40	1
ABSH04	44.192	143.08	1	IBUH01	42.874	141.82	1	NIGH14	37.030	138.85	-2
ABSH05	44.115	143.01	3	IBUH02	42.871	142.13	-2	NIGH15	37.053	139.00	1
ABSH06	44.215	143.62	2	IBUH03	42.649	141.86	-2	NIGH16	36.938	137.85	-1
ABSH07	43.849	143.09	4	IBUH05	42.563	141.35	2	NIGH17	36.857	138.10	-1
ABSH08	44.064	144.99	-3	IBUH06	42.412	141.00	-1	NIGH18	36.943	138.26	-8
ABSH10	44.081	143.94	-6	IBUH07	42.648	141.06	3	NIGH19	36.811	138.78	0
ABSH11	43.914	144.19	-2	IKRH01	43.409	141.58	3	NMRH02	43.677	144.96	-7
ABSH12	43.857	144.46	177	IKRH02	43.220	141.65	0	NMRH04	43.398	145.12	-2
ABSH13	43.742	143.45	1	IKRH03	42.888	141.64	0	NMRH05	43.390	144.80	-4
ABSH14	43.723	144.18	3	ISKH01	37.527	137.28	-3	OSMH01	41.598	140.42	6
ABSH15	43.635	143.51	2	ISKH03	37.346	137.24	-1	OSMH02	41.837	140.63	2
AICH07	35.219	137.40	-4	ISKH04	37.190	136.72	-151	RMIH01	45.017	142.08	2
AICH10	35.000	137.62	-4	ISKH05	37.222	136.97	35	RMIH02	44.895	141.92	3
AICH16	35.154	137.53	0	ISKH06	37.053	136.82	142	RMIH03	44.636	141.82	3
AICH17	35.184	137.73	-3	IWTH01	40.238	141.34	-2	RMIH04	44.097	141.96	1
AKTH01	39.815	140.58	3	IWTH02	39.825	141.38	0	RMIH05	44.025	141.79	1
AKTH02	39.663	140.57	-2	IWTH03	39.802	141.65	-1	SBSH01	43.234	140.62	6
AKTH03	39.222	140.13	-4	IWTH04	39.181	141.39	-1	SBSH02	43.053	140.50	-1
AKTH04	39.174	140.71	-2	IWTH05	38.865	141.35	-1	SBSH03	43.084	140.82	2

Continued on next page

Continued from previous page

Sta	Lat(N)	Lon(E)	θ (deg)	Sta	Lat(N)	Lon(E)	θ (deg)	Sta	Lat(N)	Lon(E)	θ (deg)
AKTH05	39.072	140.32	0	IWTH06	40.261	141.17	0	SBSH05	42.950	140.82	1
AKTH06	38.980	140.50	13	IWTH07	40.270	141.57	1	SBSH06	42.831	140.48	-4
AKTH07	40.456	140.84	2	IWTH08	40.269	141.78	-4	SBSH07	42.763	140.81	2
AKTH08	40.319	140.23	-2	IWTH09	40.086	141.71	-1	SBSH08	42.768	140.98	3
AKTH09	40.276	140.46	0	IWTH10	40.139	140.95	5	SBSH09	42.610	140.48	3
AKTH10	40.300	140.58	0	IWTH11	40.081	141.19	-5	SBSH10	42.780	140.16	2
AKTH12	39.916	140.22	1	IWTH12	40.153	141.42	2	SITH01	35.929	139.73	-88
AKTH13	39.982	140.41	-1	IWTH13	39.940	141.55	-1	SITH03	35.899	139.38	7
AKTH14	40.062	140.81	-87	IWTH14	39.743	141.91	2	SITH04	35.803	139.54	4
AKTH15	39.688	140.41	-2	IWTH15	39.615	141.09	-3	SITH05	36.151	139.05	-1
AKTH16	39.545	140.35	0	IWTH16	39.644	140.95	0	SITH06	36.113	139.29	1
AKTH17	39.557	140.61	2	IWTH17	39.644	141.60	0	SITH07	35.912	139.15	-8
AKTH18	39.355	140.39	-1	IWTH18	39.463	141.68	-3	SITH08	36.027	138.97	-4
AKTH19	39.191	140.47	-4	IWTH20	39.343	141.05	-25	SITH09	36.072	139.10	-4
AOMH01	41.527	140.91	6	IWTH21	39.473	141.93	-5	SITH10	35.996	139.22	-3
AOMH02	41.405	140.86	1	IWTH22	39.334	141.30	2	SITH11	35.864	139.27	-4
AOMH03	41.234	140.99	2	IWTH23	39.274	141.82	0	SOYH01	45.335	142.12	-2
AOMH04	40.852	140.68	2	IWTH24	39.198	141.01	4	SOYH02	45.216	142.22	-3
AOMH05	40.856	141.10	1	IWTH26	38.969	141.00	-2	SOYH03	45.253	141.63	0
AOMH06	40.966	141.37	5	IWTH27	39.031	141.53	0	SOYH04	45.230	141.88	1
AOMH07	40.745	140.02	-1	IWTH28	39.009	140.86	0	SOYH05	45.488	141.88	6
AOMH08	40.762	140.31	5	KKWH01	44.597	142.30	3	SOYH06	45.102	141.78	4
AOMH09	40.620	140.35	-1	KKWH02	44.551	142.57	3	SOYH07	45.100	142.43	-3
AOMH10	40.609	140.66	3	KKWH03	44.473	142.27	-3	SOYH08	44.939	142.22	1
AOMH11	40.580	141.00	7	KKWH05	44.292	142.63	2	SOYH09	44.857	142.49	1
AOMH12	40.585	141.15	4	KKWH06	44.321	142.76	3	SOYH10	44.743	142.60	0
AOMH13	40.579	141.45	-5	KKWH07	43.370	142.34	3	SRCH02	44.116	142.14	-2
AOMH14	40.549	140.27	0	KKWH08	43.041	142.66	3	SRCH04	43.820	141.94	0
AOMH15	40.484	140.56	-1	KKWH09	44.774	142.25	-6	SRCH05	43.824	142.16	7
AOMH16	40.462	141.09	4	KKWH10	44.662	142.05	-6	SRCH06	43.695	142.08	-105
AOMH17	40.449	141.34	7	KKWH11	43.975	142.28	-5	SRCH07	43.230	141.90	1
AOMH18	40.296	141.01	4	KKWH12	43.504	142.60	-2	SRCH08	43.514	141.91	0
CHBH04	35.797	140.02	89	KKWH13	43.511	142.39	-5	SRCH09	43.059	141.81	0
CHBH10	35.546	140.24	2	KKWH14	43.384	142.52	-8	SRCH10	42.993	142.01	-1
CHBH11	35.287	140.15	-7	KKWH15	43.855	142.77	-4	SZOH24	34.834	137.66	1
CHBH12	35.344	139.86	-5	KNGH10	35.499	139.52	5	SZOH30	35.223	137.92	-3
CHBH13	35.831	140.30	-3	KNGH11	35.404	139.35	-7	SZOH31	34.940	138.08	-6
CHBH14	35.734	140.82	-2	KNGH18	35.644	139.13	-3	SZOH32	35.009	137.84	-5
CHBH16	35.138	139.96	-10	KNGH19	35.417	139.04	-6	SZOH33	35.015	138.35	-1
CHBH17	35.171	140.34	4	KNGH20	35.366	139.13	9	SZOH34	35.130	138.42	-3
CHBH20	35.088	140.10	-3	KNGH21	35.463	139.21	-1	SZOH35	34.947	139.09	178
FKSH01	37.757	139.72	0	KNGH23	35.262	139.61	-6	SZOH36	34.914	138.20	3
FKSH02	37.732	139.88	-3	KSRH01	43.436	144.08	-2	SZOH37	35.203	138.57	-5
FKSH03	37.608	139.75	-1	KSRH02	43.114	144.12	1	SZOH38	35.085	138.98	-4
FKSH04	37.451	139.81	39	KSRH03	43.385	144.63	-43	SZOH39	34.799	138.77	-8
FKSH05	37.254	139.87	-5	KSRH04	43.214	144.68	-4	SZOH40	34.783	138.97	-8
FKSH06	37.172	139.52	-7	KSRH05	43.256	144.23	0	SZOH41	34.675	138.83	-4
FKSH07	37.010	139.38	-1	KSRH06	43.220	144.43	-6	SZOH42	34.976	138.91	1
FKSH08	37.282	140.21	-3	KSRH07	43.136	144.33	2	SZOH53	34.877	138.02	
FKSH09	37.353	140.43	-86	KSRH08	43.160	143.89	-3	TCGH07	36.882	139.45	-6
FKSH10	37.162	140.09	-2	KSRH09	42.986	143.98	2	TCGH09	36.862	139.84	5

Continued on next page

Continued from previous page

Sta	Lat(N)	Lon(E)	θ (deg)	Sta	Lat(N)	Lon(E)	θ (deg)	Sta	Lat(N)	Lon(E)	θ (deg)
FKSH11	37.201	140.34	-3	KSRH10	43.208	145.12	-3	TCGH10	36.858	140.02	2
FKSH12	37.217	140.57	-5	MYGH02	38.859	140.65	0	TCGH11	36.708	139.77	-2
FKSH14	37.026	140.97	-8	MYGH03	38.921	141.64	-1	TCGH12	36.696	139.98	-3
FKSH16	37.764	140.38	1	MYGH04	38.786	141.33	-1	TCGH13	36.734	140.18	-3
FKSH17	37.664	140.60	163	MYGH05	38.579	140.78	2	TCGH14	36.551	139.62	1
FKSH18	37.489	140.54	-1	MYGH06	38.591	141.07	-2	TCGH15	36.559	139.86	-1
FKSH19	37.470	140.72	-4	MYGH08	38.113	140.84	2	TCGH16	36.548	140.08	-4
FKSH20	37.491	140.99	-5	MYGH09	38.009	140.60	-5	TCGH17	36.985	139.69	-2
FKSH21	37.342	139.31	-2	MYGH10	37.941	140.89	1	TKCH01	43.468	143.68	1
GIFH04	36.245	137.20	3	MYGH12	38.642	141.44	0	TKCH02	43.382	143.90	3
GIFH10	36.378	137.37	-1	NGNH03	35.479	137.73	-4	TKCH03	43.271	143.43	1
GIFH11	35.486	137.25	1	NGNH10	35.963	137.77	-3	TKCH04	43.174	142.92	3
GIFH13	36.274	136.90	0	NGNH11	35.916	138.31	1	TKCH05	43.121	143.62	2
GIFH14	36.249	137.52	-2	NGNH12	35.970	138.48	-4	TKCH06	42.892	143.06	0
GIFH15	36.134	137.22	0	NGNH13	35.514	137.88	-3	TKCH07	42.811	143.52	4
GIFH16	36.094	137.34	-2	NGNH14	35.309	137.63	-3	TKCH08	42.486	143.15	-1
GIFH18	35.899	137.15	-1	NGNH16	35.947	138.18	-5	TKCH10	43.334	142.94	-3
GIFH19	36.022	137.39	2	NGNH17	36.142	138.55	1	TKCH11	42.874	142.88	-2
GIFH20	35.799	137.25	1	NGNH18	35.932	137.59	-2	TKYH02	35.654	139.47	175
GIFH24	35.640	137.32	0	NGNH19	35.974	138.58	2	TKYH12	35.670	139.26	0
GIFH28	35.457	137.47	3	NGNH20	35.787	137.72	6	TKYH13	35.702	139.13	4
GNMH05	36.314	139.18	3	NGNH21	35.831	137.92	-1	TYMH04	36.791	137.47	-98
GNMH07	36.700	139.21	1	NGNH22	35.795	138.08	1	TYMH05	36.574	136.96	-114
GNMH08	36.492	138.52	0	NGNH23	35.606	137.61	4	TYMH06	36.571	137.16	-3
GNMH09	36.621	138.91	-4	NGNH24	35.615	137.88	2	TYMH07	36.441	137.04	-2
GNMH11	36.286	138.92	-8	NGNH25	35.299	137.93	-2	YMNH09	35.433	138.33	-8
GNMH12	36.144	138.91	-2	NGNH26	36.466	138.15	1	YMNH10	35.535	138.31	-1
GNMH13	36.862	139.06	1	NGNH27	36.577	138.05	2	YMNH11	35.625	138.98	-2
GNMH14	36.493	139.32	-2	NGNH28	36.708	138.10	0	YMNH12	35.562	138.45	-2
HDKH01	42.703	142.23	1	NGNH29	36.910	138.44	1	YMNH13	35.351	138.42	-3
HDKH02	42.706	142.41	1	NGNH30	36.064	137.68	0	YMNH14	35.511	138.97	-6
HDKH03	42.593	142.35	0	NGNH31	36.118	137.94	-2	YMNH15	35.532	138.60	-1
HDKH05	42.598	142.54	-3	NGNH32	36.258	137.99	0	YMNH16	35.742	138.57	-3
HDKH06	42.350	142.36	-5	NGNH33	36.460	137.96	-2	YMTH01	38.384	140.38	1
HDKH07	42.133	142.92	-2	NGNH34	36.533	137.82	-3	YMTH02	38.269	140.26	2
HYMH01	42.485	139.97	-8	NGNH35	36.382	137.82	-11	YMTH03	38.103	140.16	3
HYMH02	41.986	140.31	0	NGNH54	35.449	138.01	3	YMTH04	38.081	140.30	5
IBRH07	35.952	140.33	0	NIGH01	37.427	138.89	-3	YMTH05	37.988	139.80	6
IBRH10	36.111	139.99	-48	NIGH02	38.280	139.55	1	YMTH06	37.963	140.18	-3
IBRH11	36.370	140.14	0	NIGH04	38.131	139.54	0	YMTH07	37.896	140.03	-1
IBRH12	36.837	140.32	-4	NIGH05	37.976	139.28	1	YMTH08	38.970	140.03	2
IBRH13	36.795	140.57	-3	NIGH06	37.653	139.07	1	YMTH12	38.636	140.01	2
IBRH14	36.692	140.55	-2	NIGH07	37.666	139.26	1	YMTH13	38.470	139.76	2
IBRH15	36.557	140.30	-3	NIGH08	37.671	139.46	1	YMTH14	38.386	139.99	-1
IBRH16	36.641	140.40	19	NIGH09	37.539	139.13	-1	YMTH15	38.426	140.12	2
IBRH17	36.086	140.31	1	NIGH10	37.544	139.36	3				

Appendix B

Strong motion derived displacements of Mw 8.3 Tokachi-Oki earthquake

Method by Chao et al. (2009).

Sta	Lat	Lon	EW(cm)	NS(cm)	UD(cm)	Sta	Lat	Lon	EW(cm)	NS(cm)	UD(cm)
HDKH02	42.706	142.41	38.565	-19.733	0.52295	AKTH14	40.062	140.81	0.22358	0.47529	-5.0892
HDKH05	42.598	142.54	38.17	-22.696	-27.496	AOMH01	41.527	140.91	4.1094	4.3105	6.1157
HDKH06	42.35	142.36	31.698	-5.3622	0.16658	AOMH03	41.234	140.99	12.202	-8.5977	-0.49288
HDKH07	42.133	142.92	40.904	-8.1476	-15.899	AOMH04	40.852	140.68	-3.8241	-2.5551	-1.7927
KKWH08	43.041	142.66	22.6	-22.115	-3.2745	AOMH05	40.856	141.1	1.6914	-6.5823	-6.9166
KSRH01	43.436	144.08	2.479	-6.8398	-5.1784	AOMH10	40.609	140.66	-18.081	-4.2759	-2.4329
KSRH02	43.114	144.12	26.407	-4.6427	-4.1923	AOMH11	40.58	141	8.0133	-1.6394	9.7134
KSRH03	43.385	144.63	4.9261	4.7908	-3.8496	AOMH12	40.585	141.15	2.6695	5.941	-4.0328
KSRH04	43.214	144.68	8.5904	-1.4326	2.7471	AOMH13	40.579	141.45	-6.4282	1.4437	-2.7589
KSRH05	43.256	144.23	16.757	-4.3291	1.0679	AOMH15	40.484	140.56	-6.8213	1.5323	-0.30732
KSRH06	43.22	144.43	12.366	2.2213	4.5946	AOMH16	40.462	141.09	0.9176	3.0416	-2.5514
KSRH07	43.136	144.33	12.483	-2.6335	14.652	AOMH17	40.449	141.34	-2.6986	6.557	-4.7908
KSRH09	42.986	143.98	20.544	-11.868	-17.396	AOMH18	40.296	141.01	14.587	0.62189	6.0413
TKCH01	43.468	143.68	85.225	-15.801	-4.1078	IBUH04	42.642	140.66	5.4647	1.9443	-2.9801
TKCH02	43.382	143.9	13.427	-8.4817	-1.0156	IBUH06	42.412	141	3.0263	0.54302	3.4359
TKCH03	43.271	143.43	14.275	-21.407	-2.3031	IBUH07	42.648	141.06	7.5519	3.401	-6.6401
TKCH04	43.174	142.92	22.912	-22.082	-5.1927	IKRH01	43.409	141.58	5.7182	-3.9662	0.25438
TKCH05	43.121	143.62	18.276	-22.693	-5.3317	IWTH01	40.238	141.34	-0.11166	1.2404	24.904
TKCH06	42.892	143.06	34.715	-37.639	-13.122	IWTH02	39.825	141.38	3.0597	3.9432	2.9689
TKCH07	42.811	143.52	52.738	-42.506	-17.465	IWTH03	39.802	141.65	2.0181	1.4881	-3.3306
TKCH08	42.486	143.15	66.985	-32.975	-28.835	IWTH06	40.261	141.17	-0.099783	9.4552	-8.914
TKCH11	42.874	142.88	32.767	-30.865	-13.039	IWTH07	40.27	141.57	-17.655	-10.6	3.6851

Continued on next page

Continued from previous page

Sta	Lat	Lon	EW(cm)	NS(cm)	UD(cm)	Sta	Lat	Lon	EW(cm)	NS(cm)	UD(cm)
ABSH04	44.192	143.08	12.783	-9.814	-5.7818	IWTH09	40.086	141.71	-3.4248	1.6095	-2.5498
ABSH05	44.115	143.01	3.134	-7.5638	-1.999	IWTH10	40.139	140.95	1.9868	1.1855	-1.3455
ABSH06	44.215	143.62	-3.1854	-2.6253	0.7492	IWTH11	40.081	141.19	7.6612	1.2264	-0.49646
ABSH07	43.849	143.09	20.511	1.202	0.20291	IWTH12	40.153	141.42	8.9663	7.2412	3.0432
ABSH08	44.064	144.99	1.5625	0.0010757	-1.1303	IWTH13	39.94	141.55	0.25469	1.8743	-6.3439
ABSH10	44.081	143.95	1.8012	-8.9575	4.9942	IWTH14	39.743	141.91	15.539	25.831	-28.739
ABSH11	43.914	144.19	-1.7546	-9.3561	-2.1344	IWTH15	39.615	141.09	-3.2547	1.3602	0.18082
ABSH12	43.857	144.46	0.94469	-7.7392	-2.0847	IWTH17	39.644	141.6	-6.1742	4.1736	-1.3273
ABSH13	43.742	143.45	10.573	-12.353	1.9554	IWTH18	39.463	141.68	-12.237	-1.0726	6.1052
ABSH14	43.723	144.18	-0.21989	2.931	-3.0806	IWTH21	39.473	141.93	1.2881	-9.093	-6.1458
ABSH15	43.635	143.51	6.6598	-13.024	10.166	IWTH22	39.334	141.3	-1.5234	-1.3809	-4.2534
AOMH06	40.966	141.37	8.3173	-4.1175	-1.491	IWTH23	39.274	141.82	-1.4756	7.0182	12.021
HDKH01	42.703	142.23	23.525	-11.131	-7.8526	KKWH01	44.597	142.3	3.0769	-4.8783	0.49758
HDKH04	42.513	142.04	17.14	-5.3789	-3.514	KKWH02	44.551	142.57	-1.3099	-1.7481	-6.6509
IBUH01	42.874	141.82	10.952	-5.0784	-0.4103	KKWH03	44.473	142.27	5.248	-3.3151	2.8436
IBUH02	42.871	142.13	19.826	-14.746	-0.68522	KKWH05	44.292	142.63	7.1111	5.335	1.7187
IBUH03	42.649	141.86	13.124	-7.0985	-5.8369	KKWH06	44.321	142.77	-5.3536	-6.15	-6.1114
IBUH05	42.563	141.35	10.471	-8.4375	2.7799	KKWH09	44.775	142.25	20.131	-32.772	-37.089
IKRH02	43.22	141.65	11.326	-8.8693	-1.9694	KKWH10	44.662	142.05	6.1032	-3.9944	4.8824
IKRH03	42.888	141.64	12.241	-10.789	-5.1169	KKWH11	43.975	142.28	5.0947	-9.3024	2.9544
IWTH08	40.269	141.78	20.233	18.826	-21.582	OSMH01	41.598	140.42	1.1575	-2.0072	3.3792
KKWH07	43.37	142.34	12.91	-13.154	2.4628	OSMH02	41.837	140.63	5.657	-1.3664	4.2664
KKWH12	43.504	142.6	10.212	-11.715	-0.21734	RMIH03	44.636	141.82	-8.1355	-8.9833	-9.6526
KKWH13	43.511	142.39	11.458	-12.274	1.8364	RMIH04	44.097	141.96	7.3962	-3.1263	2.8593
KKWH14	43.384	142.52	18.856	-12.87	-6.5764	RMIH05	44.025	141.79	6.2832	-4.7139	-3.5157
KKWH15	43.855	142.77	5.6294	-14.771	-0.96358	SBSH01	43.234	140.62	4.6448	-2.9017	0.40022
KSRH10	43.208	145.12	8.938	5.6942	-0.27664	SBSH03	43.084	140.82	5.8622	0.4719	-0.82392
NMRH02	43.677	144.96	6.2758	-1.3145	-15.318	SBSH04	42.976	140.62	5.6815	-0.32827	2.6997
NMRH04	43.398	145.12	3.4149	-1.0731	-11.692	SBSH05	42.95	140.82	1.6985	-4.7883	3.1686
NMRH05	43.39	144.8	7.6907	-70.689	-0.67839	SBSH06	42.831	140.48	3.1426	2.1494	-0.70876
SRCH05	43.824	142.16	10.564	-8.0966	-4.2467	SBSH07	42.763	140.81	32.797	-14.217	-3.4825
SRCH06	43.695	142.08	9.6041	-3.9711	-4.7867	SBSH08	42.768	140.98	8.5094	-3.2562	-0.52432
SRCH07	43.23	141.9	13.043	-11.701	4.623	SBSH09	42.61	140.48	-2.701	-7.7184	-7.6488
SRCH08	43.514	141.91	6.1117	-10.904	-4.5496	SOYH08	44.939	142.22	-17.014	36.01	26.684
SRCH09	43.059	141.81	13.797	-7.6721	-3.619	SOYH09	44.857	142.49	4.3139	-4.593	7.2939
SRCH10	42.993	142.01	15.035	-8.0061	-3.4366	SOYH10	44.743	142.6	8.9833	2.0527	0.94939
TKCH10	43.334	142.94	18.172	-20.75	-3.5912	SRCH01	44.28	142.16	26.938	-55.393	-68.434
ABSH01	44.528	142.84	7.3499	-1.3945	-3.4359	SRCH02	44.116	142.14	-39.687	-5.1804	-0.18465
ABSH02	44.423	143.03	7.6516	-2.1429	1.2146	SRCH03	43.999	142.13	0.63717	-16.14	0.74836
ABSH03	44.384	143.24	5.0504	-5.2598	9.8782	SRCH04	43.82	141.94	-10.753	-1.85	8.8742
AKTH07	40.456	140.84	0.60905	0.89855	-4.3446						

Appendix C

Strong motion derived displacements of Mw 9.0 Tohoku earthquake

Method by using T1 and T3 as function of distance following Eqs. 4.1 to 4.6.

Sta	Lat	Lon	EW(cm)	NS(cm)	UD(cm)	Sta	Lat	Lon	EW(cm)	NS(cm)	UD(cm)
AKTH01	39.815	140.58	89.886	-61.738	1.0989	IWTH08	40.269	141.78	48.812	-50.5	-14.693
AKTH02	39.663	140.57	92.05	-61.884	8.3802	IWTH09	40.086	141.71	63.113	-66.311	-4.1476
AKTH03	39.222	140.13	115.52	-39.677	0.73645	IWTH10	40.139	140.95	64.501	-60.213	4.1992
AKTH04	39.174	140.71	152.2	-80.425	-0.49286	IWTH11	40.081	141.19	63.605	-58.942	7.1635
AKTH05	39.072	140.32	121.66	-60.411	1.8796	IWTH12	40.153	141.42	60.023	-66.423	-4.8092
AKTH06	38.98	140.5	190.99	193.4	-5.2622	IWTH13	39.94	141.55	88.412	-75.99	-7.1803
AKTH07	40.456	140.84	41.968	-39.93	-3.8002	IWTH14	39.743	141.91	123.45	-99.749	-18.118
AKTH08	40.319	140.23	169.99	-24.863	0.63942	IWTH15	39.615	141.09	128.93	-104.28	3.017
AKTH09	40.276	140.46	62.708	-41.953	3.9897	IWTH16	39.644	140.95	111.07	-75.544	-4.5565
AKTH10	40.3	140.58	50.718	-39.393	0.89318	IWTH17	39.644	141.6	140.5	-116.41	-9.7797
AKTH12	39.916	140.22	110.46	-44.537	5.9771	IWTH18	39.463	141.68	190.37	-135.62	-16.139
AKTH13	39.982	140.41	70.977	-38.359	5.3922	IWTH20	39.343	141.05	204.11	-17.82	13.261
AKTH14	40.062	140.81	52.773	-43.544	-1.0572	IWTH21	39.473	141.93	189.44	-147.71	-33.541
AKTH15	39.688	140.41	88.929	-50.051	26.449	IWTH22	39.334	141.3	197.44	-132.83	-10.028
AKTH16	39.545	140.35	81.373	-50.586	-4.473	IWTH23	39.274	141.82	263.01	-186.5	-15.352
AKTH17	39.557	140.61	98.814	-53.531	6.1917	IWTH24	39.198	141.01	167.14	-75.328	-11.613
AKTH18	39.355	140.39	109.88	-50.503	21.923	IWTH26	38.969	141	230.2	-93.377	-9.3968
AKTH19	39.191	140.47	86.684	-78.678	10.141	IWTH27	39.031	141.53	307.4	-137.78	-39.789
AOMH04	40.852	140.68	32.869	-0.82533	1.6789	IWTH28	39.009	140.86	204.94	-109.73	-11.143
AOMH05	40.856	141.1	27.281	-29.628	-3.8292	KNGH18	35.644	139.13	65.653	17.968	-7.8665
AOMH06	40.966	141.37	25.432	-22.144	0.12184	MYGH02	38.859	140.65	189.91	-79.281	-8.611
AOMH07	40.745	140.02	34.466	-28.633	-0.51182	MYGH03	38.921	141.64	372.3	-161.1	-74.118

Continued on next page

Continued from previous page

Sta	Lat	Lon	EW(cm)	NS(cm)	UD(cm)	Sta	Lat	Lon	EW(cm)	NS(cm)	UD(cm)
AOMH08	40.762	140.31	30.183	-25.114	-67.756	MYGH04	38.786	141.33	338.43	-142.3	-60.657
AOMH10	40.609	140.66	36.392	-32.822	12.25	MYGH05	38.579	140.78	232.82	-63.403	-13.262
AOMH11	40.58	141	39.373	-37.161	-1.6156	MYGH06	38.591	141.07	307.14	-87.693	-26.873
AOMH12	40.585	141.15	42.634	-45.211	-9.2997	MYGH08	38.113	140.84	281.47	-57.38	-31.021
AOMH13	40.579	141.45	35.727	-27.238	-2.1209	MYGH09	38.009	140.6	197.18	-22.662	-12.989
AOMH14	40.549	140.27	48.581	-31.997	-4.3796	MYGH10	37.941	140.89	279.9	-32.245	-28.739
AOMH15	40.484	140.56	37.155	-28.554	1.2374	MYGH12	38.642	141.44	400.09	-150.28	-68.961
AOMH16	40.462	141.09	44.801	-46.166	-5.2192	NIGH02	38.28	139.55	90.249	-15.218	-1.7509
AOMH17	40.449	141.34	44.677	-43.266	5.9567	NIGH04	38.131	139.54	352.26	-4.2362	-122.81
AOMH18	40.296	141.01	45.073	-50.077	-5.2699	NIGH05	37.976	139.28	66.709	-13.393	5.6412
CHBH10	35.546	140.24	17.781	2.2877	-24.252	NIGH06	37.653	139.07	55.141	0.85313	-0.78492
CHBH14	35.734	140.82	17.897	-1.6071	-14.224	NIGH07	37.666	139.26	74.555	-7.793	1.3158
FKSH01	37.757	139.72	102.21	-6.3255	-8.6688	NIGH08	37.671	139.46	146.15	41.344	2.1016
FKSH02	37.732	139.88	114.35	-9.8017	-23.082	NIGH09	37.539	139.13	61.538	5.2222	-0.7621
FKSH03	37.608	139.75	99.453	-7.2491	-1.8769	NIGH10	37.544	139.36	107.24	-0.63204	-6.8577
FKSH05	37.254	139.87	106.39	15.961	-402.76	NIGH15	37.053	139	44.483	2.3103	0.87128
FKSH06	37.172	139.52	83.061	6.542	-305.83	SITH01	35.929	139.73	43.251	1.5174	82.967
FKSH08	37.282	140.21	132.76	12.326	-19.673	SITH03	35.899	139.38	33.891	-11.292	-280.64
FKSH09	37.353	140.43	141.73	-8.1972	-28.228	SITH04	35.803	139.54	158.01	115.89	1.3005
FKSH10	37.162	140.09	123.61	2.3183	-19.512	SITH05	36.151	139.05	41.748	0.087054	-13.121
FKSH11	37.201	140.34	137.25	3.8781	-32.423	SITH06	36.113	139.29	61.055	6.5485	-8.3727
FKSH12	37.217	140.57	153.7	-20.126	-33.76	SITH07	35.912	139.15	38.81	6.8321	-15.895
FKSH14	37.026	140.97	181.78	-20.104	-64.418	SITH09	36.072	139.1	34.052	-11.876	-15.117
FKSH16	37.764	140.38	196.72	-100.26	-6.2992	SITH10	35.996	139.22	44.542	-9.7665	-10.58
FKSH17	37.664	140.6	198.48	-12.381	-29.597	SITH11	35.864	139.27	37.104	-14.195	-15.989
FKSH18	37.489	140.54	186.04	-12.282	-30.337	TCGH07	36.882	139.45	61.942	13.503	-0.28707
FKSH19	37.47	140.72	196.6	-16.337	-37.829	TCGH09	36.862	139.84	83.724	15.438	-18.063
FKSH20	37.491	140.99	237.53	-26.79	-63.449	TCGH10	36.858	140.02	94.058	6.712	-13.322
FKSH21	37.342	139.31	69.363	-2.1147	-0.12253	TCGH11	36.708	139.77	69.701	42.541	-40.191
GNMH05	36.314	139.18	38.257	170.48	111.93	TCGH12	36.696	139.98	64.153	4.0432	-7.5036
GNMH07	36.7	139.21	44.691	6.5773	-11.347	TCGH13	36.734	140.18	94.485	0.50313	-30.611
GNMH14	36.493	139.32	51.743	10.379	-11.854	TCGH14	36.551	139.62	59.089	3.7341	-11.954
IBRH07	35.952	140.33	43.657	-51.426	-1.2439	TCGH16	36.548	140.08	78.773	14.886	-10.671
IBRH11	36.37	140.14	69.753	-1.5233	-23.627	TCGH17	36.985	139.69	73.051	8.0212	-1.8061
IBRH12	36.837	140.32	119.87	9.1052	-33.708	TKYH02	35.654	139.47	-90.862	-116.22	75.394
IBRH13	36.795	140.57	130.42	-7.1999	-39.662	TKYH12	35.67	139.26	24.197	7.385	-10.463
IBRH14	36.692	140.55	118.06	7.3361	-36.497	TKYH13	35.702	139.13	25.388	16.117	-6.5374
IBRH15	36.557	140.3	91.868	15.502	-26.476	YMTH01	38.384	140.38	580.44	-31.744	-6.2287
IBRH16	36.641	140.4	93.282	8.2276	-35.059	YMTH02	38.269	140.26	162.98	-33.592	-6.8865
IBRH17	36.086	140.31	54.481	11.461	-29.252	YMTH03	38.103	140.16	149.14	-20.642	-3.5509
IBRH18	36.363	140.62	82.219	8.616	-55.028	YMTH04	38.081	140.3	167.55	-11.488	-14.893
IBRH19	36.214	140.09	52.668	6.5175	-16.624	YMTH05	37.988	139.8	120.63	47.239	-11.657
IBRH20	35.828	140.73	23.529	16.383	-4.8911	YMTH06	37.963	140.18	147.07	-13.938	144.38
IWTH01	40.238	141.34	54.046	-54.52	6.3165	YMTH07	37.896	140.03	134.34	-7.0132	-3.6902
IWTH02	39.825	141.38	100.7	-77.745	-3.8704	YMTH08	38.97	140.03	115.79	-40.755	-859.49
IWTH03	39.802	141.65	108.23	-100.13	-4.6736	YMTH12	38.636	140.01	178.79	-52.974	1.9688
IWTH04	39.181	141.39	249.18	-152.63	-9.9623	YMTH13	38.47	139.76	104.86	-27.023	0.45629
IWTH05	38.865	141.35	343.57	-152.53	565.28	YMTH14	38.386	139.99	115.14	-17.482	-7.0189
IWTH06	40.261	141.17	53.574	-57.932	-7.5676	YMTH15	38.426	140.12	139.23	-35.944	0.32888
IWTH07	40.27	141.57	54.611	-51.054	-2.1927						